

QATAR UNIVERSITY

COLLEGE OF PHARMACY

SUCCINYLATED CURCUMIN LOADED IN MANNOSYLATED CHITOSAN
NANOPARTICLES FOR COLON CANCER THERAPY

BY

SOUROUR IDOUDI

A Thesis Submitted to

the College of Pharmacy

in Partial Fulfillment of the Requirements for the Degree of

Masters of Science in Pharmacy

June 2022

© 2022. Sourour Idoudi. All Rights Reserved.

COMMITTEE PAGE

The members of the Committee approve the Thesis of
Sourour Idoudi defended on 26/04/2022.

Dr. Nashiru Billa, PhD
Thesis/Dissertation Supervisor

Dr. Yousef Hijji, PhD
Co-Supervisor

Dr. Hesham Korashy, PhD
Committee Member

Dr. Shahab Uddin Khan, PhD
Committee Member

Approved:

Feras Alali, Dean, College of Pharmacy

ABSTRACT

IDOUDI, SOUROUR M., Masters : June [2022], Pharmaceutical Sciences

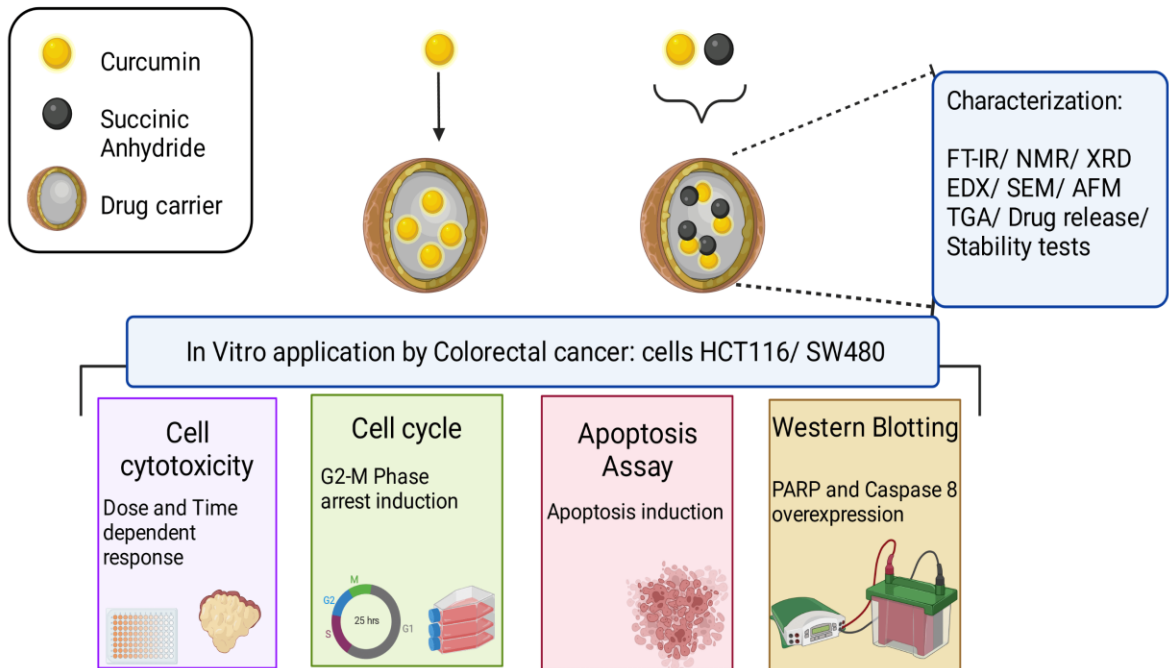
Title: Succinylated Curcumin Loaded in Mannosylated Chitosan Nanoparticles for Colon Cancer Therapy.

Supervisor of Thesis: Prof. Nashiru Billa

Colon cancer (CRC) is the second leading cause of death and the third most diagnosed type worldwide. Although curcumin (CUR) has potent anticancer activity, it suffers from low solubility, bioavailability, and instability. This study aims to conjugate CUR to succinic anhydride (SA) and then formulate in mannosylated-chitosan nanoparticles (CUR.SA-NPs). The formulation was optimized in comparison to curcumin only in the same delivery system. Dynamic light scattering (DLS) studies disclosed a higher size of CUR-NPs (268 ± 6 nm) and CUR.SA-NPs (342 ± 4.6 nm) compared to empty delivery system, CM-NPs, (101 ± 4.3 nm). Conversely, the zeta-potential was reduced from 41.2 ± 0.15 mV to 11 ± 0.75 mV and 13.6 ± 0.8 mV for CUR-NPs and CUR.SA-NPs respectively. The entrapment efficiency was 93.34 ± 0.40 for CUR-NPs, and 98.46 ± 0.06 for CUR.SA-NPs. Physical and structural characteristics of the formulated nanoparticles were investigated using FTIR, NMR, XRD, SEM, and TGA and each attest to the formation of the functionalized CUR.SA-CMNPs. *In vitro* drug release illustrated a sustained release profile of CUR and CUR.SA over a period of 3 days and an excellent cytotoxicity and intracellular uptake by CRC cell lines (SW480 and HCT116). Thus, CUR-NPs and CUR.SA-NPs can be considered as a promising delivery strategy for CRC treatment.

Keywords: Curcumin, Succinic Anhydride, Mannose, Chitosan, Nanoparticles, Ionic gelation, Colorectal cancer.

Graphical abstract



DEDICATION

I dedicate this thesis to my beloved family for their inspiration and their dedicated partnership for success in my life

ACKNOWLEDGMENTS

I would like to thank Almighty Allah for giving me resoluteness and power to achieve this work.

I would like to acknowledge my advisor Prof. Nashiru Billa for his continuous supervision and support. I would like also to appreciate my co-supervisors; Prof. Yousef Hijji, for his insightful assistance and comments that shaped this research towards success, Dr. Shahab Uddin Khan, for sharing his rich experience, his encouragement and great support, and Dr. Hesham Korashy for his continuous assistance and inspiration. Many thanks go to Dr. Maysaloun Merhi, for her valuable follow up and guidance during my work in HMC. My deepest thanks to Dr. Takwa Bedhiafi for her continuous support and guidance and sharing her valuable experience with me. I was lucky to be supervised by such a talented team.

My appreciation goes to the faculty members of the College of Pharmacy and my colleagues at the MSc program for enriching my experience. Special thanks go to my lab partners Aida and Areej for their support and cooperation.

I am forever thankful to the most valuable treasure in life, my family. Mom and Dad, thank you for believing in me, and I would never reach this stage today without you. Your unconditional assistance and sacrifice to pursue my dreams gave me the strength to continue my work here.

Last but not least, to those who have provided support indirectly to this work, thank you very much.

TABLE OF CONTENTS

DEDICATION	v
ACKNOWLEDGMENTS	vi
LIST OF TABLES	xii
LIST OF FIGURES	xiii
LIST OF ABBREVIATIONS	xvi
Chapter 1: Introduction	1
1.1 General overview	1
1.2 Colon and colorectal cancer	2
1.2.1 Anatomy of the colon	2
1.2.2 Colorectal cancer	5
1.2.3 Drug delivery to the colon	8
1.2.4 Management of colorectal cancer	12
1.2.5 Constraints from available treatments	13
1.3 Curcumin	13
1.3.1 Chemical and physical properties of curcumin	14
1.3.2 Anti-colon cancer activity of curcumin	15
1.3.3 Combination therapy with curcumin	18
1.3.4 Clinical trials conducted on curcumin	18
1.3.5 Physicochemical and therapeutic constraints on effectiveness of curcumin	21
1.3.6 Strategies used to overcome physicochemical and therapeutic limitations of	

curcumin	22
1.4 Chitosan.....	27
1.4.1 Methods of preparation for polymeric NPs	28
1.4.2 Physical techniques for NPs characterization.....	34
1.5 D-Mannose	40
1.6 Succinic anhydride	41
1.7 Study rationale and objectives.....	42
CHAPTER 2: MATERIALS AND METHODS	44
2.1 Materials.....	44
2.2 Synthesis of chitosan-mannose conjugate.....	44
2.3 Curcumin-Succinic anhydride Conjugate synthesis.....	45
2.4 CUR.SA -loaded CM-TPP nanoparticles synthesis	46
2.5 Stability test of CUR and CUR.SA	47
2.6 Solubility of CUR and CUR.SA conjugate test	48
2.7 Characterization of the nanoparticles	48
2.7.1 FT-IR Analysis of samples	48
2.7.2 NMR spectroscopic analysis	48
2.7.3 Zeta size and potential	48
2.7.4 Atomic force microscopy	49
2.7.5 X-Ray Diffraction (XRD) Analysis.....	49
2.7.6 HPLC assay for CUR quantification	49

2.7.7 Evaluation of encapsulation parameters	50
2.8 Drug release from prepared NPs	50
2.9 Morphological and elemental analyses of NP by SEM and EDX.....	51
2.10 Thermogravimetric analysis	51
2.11 Stability test of nanoparticles	52
2.11.1 Structural assessment.....	52
2.11.2 Storage condition effect.....	52
2.12 <i>In vitro</i> cell evaluation of formulations.....	52
2.12.1 Maintenance of cell culture media.....	52
2.12.2 Subculturing of cells.....	53
2.12.3 Cell counting.....	53
2.12.4 Cell cytotoxicity	53
2.12.5 Cell Cycle analysis	54
2.12.6 Cellular apoptosis analysis	55
2.12.7 Western Blotting.....	55
2.13. Statistical analysis	56
CHAPTER 3: RESULTS	57
Physicochemical characterization	57
3.1.1 FT-IR analysis	57
3.1.2 NMR spectroscopic analysis	60
3.1.3 Particle size and charge analysis	62

3.1.4 The encapsulation and loading efficiency of nanoparticles.....	64
3.1.3 Stability test of CUR and CUR.SA conjugate.....	64
3.1.6 Solubility of CUR and CUR.SA conjugate test.....	66
3.1.7 AFM analyses	66
3.1.8 EDX Analysis	68
3.1.9 Morphology analysis of NPs	70
3.1.10 XRD analyses	71
3.1.11 TGA Analyses	73
3.2 Drug release from prepared NPs	74
Stability test of nanoparticles	76
3.3.1 Structural assessment.....	76
3.3.2 Storage condition effect.....	77
3.4 In vitro cell evaluation of formulations.....	78
3.4.1 Cell cytotoxicity	78
3.4.2 IC ₅₀ Calculation	83
3.4.3 Effects of nanoformulations on morphology of CRC cell lines	84
3.4.4 Cell cycle	87
3.4.5 Cell apoptosis	91
3.4.6 Western Blotting.....	94
CHAPTER 4: DISCUSSION.....	96
CHAPTER 5: CONCLUSIONS AND FUTURE DIRECTIONS	106

References..... 108

LIST OF TABLES

Table 1. Examples of enteric polymers and pH threshold.	10
Table 2. Summary of CUR on-going trial as anti-CRC and colon related diseases drug.	20
Table 3. Optimization process of the prepared nanoparticles.....	47
Table 4. Optimization of prepared formulations.....	63
Table 5. Elemental composition of samples (% Wt).	68
Table 6. NPs incubation in DMEM culture media.	76
Table 7. NPs incubation in RPMI culture media.	77
Table 8. IC ₅₀ values in μM of CUR-NPs and CUR.SA-NPs on colonic cell lines.....	84

LIST OF FIGURES

Figure 1. Colonic region representation.....	3
Figure 2. Graphical illustration of stages 0, I, and II of CRC.....	6
Figure 3. Graphical illustration of stage III of CRC	7
Figure 4. Graphical illustration of stage IV of CRC.....	8
Figure 5. Representation of the hydrolysis pathway of sulfasalazine into sulphapyridine and 5-aminosalicylic acid.	9
Figure 6. Illustration on the composition of budesonide granules of Entocort.....	11
Figure 7. Summary of available treatments for CRC.	12
Figure 8. Chemical structure of Curcumin, Demethoxycurcumin, and Bis-demethoxycurcumin.....	14
Figure 9. Summary of CUR modulation pathways of cancer progression and regulation of signal transduction pathways.....	17
Figure 10. Biotransformation and CUR metabolites	22
Figure 11. Graphical illustration of polymeric NPs.....	24
Figure 12. Graphical representation of polymeric micelles for delivering drugs.	25
Figure 13. Graphical representation of liposomal carriers for drug delivery.	26
Figure 14. Graphical representation of nanogel carriers as drug delivery systems	26
Figure 15. Graphical representation of gold nanoparticles as drug delivery systems.	27
Figure 16. Alkaline deacetylation of Chitin into Chitosan.	28
Figure 17. Representation of the Polymeric NPs preparation through single emulsion-solvent evaporation technique.....	30
Figure 18. Representation of the two-step processes to produce DE.	30
Figure 19. Illustration of salting out procedure for preparing polymeric NPs.....	31
Figure 20. Different stages enrolled in the Emulsification-diffusion technique.....	32

Figure 21. Illustration of the spray-drying process for polymeric NPs production	33
Figure 22. Polymeric NPs synthesis using the ionotropic gelation method	34
Figure 23. Basic components in the FT-IR spectrometer.	35
Figure 24. Basic principle of NMR.	36
Figure 25. Illustration of AFM set-up.....	37
Figure 26. Illustration of DLS instrumentation.....	38
Figure 27. Illustration of X-ray diffraction instrumentation.....	39
Figure 28. Schematic illustration of TGA instrument.	40
Figure 29. Chemical structure of D-mannose.	41
Figure 30. Method for CUR.SA-NPs production using ionic gelation under constant magnetic stirring.	47
Figure 31. Calibration curve of CUR through serial dilution of the respective standard CUR solution in methanol	50
Figure 32. Graphical representation of the formulated NPs	57
Figure 33. FT-IR spectra of CS, Mannose, and CM Conjugate(A), CUR, SA, and CUR.SA conjugate (B), STPP, CM-NPS, CUR-NPs, and CUR.SA-NPs (C).....	58
Figure 34. ¹ H NMR Spectra of CS (A), and CM conjugate (B)	61
Figure 35. ¹ H NMR spectra of CUR(A), CUR.SA (B) and ¹³ C NMR spectra of CUR(C), CUR.SA (D)	62
Figure 36. Stability test of free CUR (A), and CUR.SA conjugate (B).....	65
Figure 37. Solubility test of CUR.SA conjugate in different media.....	66
Figure 38. AFM images of CM-NPs (A),CUR-NPs (B), and CUR.SA-NPs (C).....	67
Figure 39. EDX spectra of CS (A), STPP (B), CM-NPs (C), CUR-NPs (D), and CUR.SA- NPs (E).	69
Figure 40. SEM images proving the formation of CM-NPs (A), CUR-NPs (B), and	

CUR.SA-NPs (C).....	70
Figure 41. XRD patterns of CS, Mannose, CM Conjugate, STPP and CM-NPs (A), CUR, SA, CUR-SA Conjugate, CUR-NPs, and CUR.SA-NPs (B).	72
Figure 42. TGA curves of Chitosan, Mannose, CM Conjugate, CM NPs, CUR, SA, CUR-SA Conjugate, CUR-CM NPs, and CUR.SA-CM NPs.....	73
Figure 43. In vitro drug release profiles of the prepared CUR-NPs (A), and CUR.SA- NPs (B) in PBS.	75
Figure 44. Stability test of the mean size (nm), Zeta potential (mV), and PDI of the CUR-NPs (A) and CUR.SA-NPs (B)	78
Figure 45. SW480 cell viability treated after 24 hours (A) and after 48 hours (B) using CCK-8 assay.	80
Figure 46. SW480 cell viability treated Free SA (10 and 100 μ M), after 24 and 48 hours using CCK-8 assay.....	82
Figure 47. HCT116 viability treated after 24 hours (A) and after 48 hours (B) using CCK-8 assay	82
Figure 48. HCT116 cell viability treated Free SA (10 and 100 μ M), after 24 and 48 hours using CCK-8 assay.	83
Figure 49. Representative microscope images of live and dead cells showing morphological changes in SW480 cells after different treatments for 24 hours.....	85
Figure 50. Representative microscope images of live and dead cells showing morphological changes in HCT116 cells after different treatments for 24 hours.....	86
Figure 51. Cell Cycle analysis of SW480 cells after treatment with CUR-NPs (10 and 25 μ M), CUR.SA-NPs (10 and 25 μ M), and untreated cells for 24 hours.	88
Figure 52. Cell Cycle analysis of HCT116 cells after treatment with CUR-NPs (10 and 25 μ M), CUR.SA-NPs (10 and 25 μ M), and untreated cells for 24 hours.	90

Figure 53. Apoptotic cell death of SW480 cells after treatment with CUR-NPs (10 and 25 μ M), CUR.SA-NPs (10 and 25 μ M), and untreated cells for 24 hours.92

Figure 54. Apoptotic cell death of HCT116 cells after treatment with CUR-NPs (10 and 25 μ M), CUR.SA-NPs (10 and 25 μ M), and untreated cells for 24 hours.93

Figure 55. Western blot bands of Total PARP and Cleaved Caspase 8 in SW480 and HCT116 cell lines.94

Figure 56. Quantification results as average density to β -actin of cleaved caspase 8 (A) and total PARP (B).95

LIST OF ABBREVIATIONS

5-ASA:	5-aminosalicylic acid
5-FU:	5-Fluorouracil
Akt:	Protein kinase
AFM:	Atomic force microscopy
API:	Active pharmaceutical ingredient
Bcl-2:	B-cell lymphoma-2
Bcl-xL:	B-cell lymphoma-extra-large
Bax:	B-cell lymphoma-2
CD:	Crohn's disease
CRC:	Colorectal cancer
CUR:	Curcumin
CS:	Chitosan
CURDD:	CUR Diethyl Disuccinate
CM:	Chitosan-Mannose conjugate
CUR.SA:	Curcumin-Succinic anhydride conjugate
CCK8:	Cell Counting Kit-8
CDCl ₃ :	Deuterated chloroform
DE:	Double emulsion
DLS:	Dynamic light scattering
DMAP:	Dimethyl amino pyridine
DMEM:	Dulbecco's Modified Eagle Medium
D ₂ O:	Deuterium Oxide
EMT:	Epithelial-mesenchymal transition
EE:	Encapsulation efficiency
EC:	Ethyl cellulose
EDX:	Energy Dispersive X-Ray Analysis
FAP:	Familial adenomatous polyposis
FDA:	Food and Drug Administration
FOBT:	Faecal occult blood test
FT-IR:	Fourier transform infrared spectroscopy
GIT:	Gastrointestinal tract

GPC3: Glypican-3
GST: Glutathione S-transferases
HPMA: N-(2-hydroxypropyl)-methacrylamide
HPLC: High Performance Liquid Chromatography
HepG2: Hepatocellular carcinoma
IBD: Inflammatory bowel disease
IARC: International Agency for Research on Cancer
JAK: Janus kinase
MAPK: Mitogen-activated protein kinase
MLH1: MutL homolog 1
MMR: Mismatch repair
MoPH: Ministry of Public Health
MSH2: MutS homolog 2
mt-sDNA: Multitarget stool DNA testing
mAbs: Immunomodulatory monoclonal antibody
mCRC :Metastatic CRC
mTOR: Mammalian target of the rapamycin
MR: Mannose receptor
MW: Molecular weight
NF- κ B: Nuclear factor- κ B
NPs: Nanoparticles
NMR: Nuclear Magnetic Resonance
o/w/o: oil-water-oil
OD: Optical density
PRR: Pattern recognition receptor
PI3K: Phosphoinositide 3-kinase
PGE2: Prostaglandin E2
PLA: polylactic acid
PEG: Polyethylene glycol
PGA: Polyglycolic acid
PAA: Polyaspartate
PLGA: Poly(D,L-lactide-co-glycolic) acid
PCL: Poly ϵ -caprolactone
PPO: Poly propylene oxide

PTX: Paclitaxel
PS: Particle size
RPMI: Roswell Park Memorial Institute
SCFAs: Short-chain fatty acids
SC-RT: Short-course radiotherapy
SLZ: Sulfasalazine
STAT: Signal transducer and activator of transcription
SE: Single emulsion
SCF: Supercritical fluid
SEM: Scanning electron microscopy
SFM: Scanning force microscope
SPMs: Scanning probe microscopes
SA: Succinic Anhydride
STPP: Sodium tripolyphosphate
SD: Standard deviation
TGA: Thermogravimetric analysis
UC: Ulcerative colitis
UV: Ultraviolet
UV-Vis: UV-Visible
UATR: Universal attenuated total reflectance
VEGF: Vascular endothelial growth factor
WHO: World Health Organization
w/o/w: water-oil-water
XRD: X-ray diffraction

Chapter 1: Introduction

1.1 General overview

Cancer is one of the most devastating diseases in humanity with an upward trend in statistics reported annually (1). There are several types of cancers, but for the remit of this thesis, the focus will be on colorectal cancer (CRC). Colon cancer, also referred to as CRC and bowel cancer, is the growth of cancer originating from the epithelial cells within the colon or rectum of the gastrointestinal tract (GIT) (2). Available treatments for CRC include use of cytotoxic drugs, radiotherapy, chemotherapy, and surgery (3,4). Chemotherapy is the most viable treatment option because of ease of administration to patient and the fact that it is least invasive as well, notwithstanding the side effects imposed. However, the side effects remain a significant constraint which impacts negatively on the quality of life of patients (5). Chemotherapy is also associated with non-specificity and cancer relapse through multi-drug resistance is a reality. These poor outcomes are considered the main limitations associated with the chemotherapeutic approaches in CRC therapy (6).

In the past decades, natural products of plant origin have arguably emerged as key contenders to unlocking the aforementioned constraints associated with chemotherapy. In fact, some of these natural products have made significant inroads with regards to chemotherapy and crucially, have been found to manifest fewer side effects (7,8). Curcumin (CUR) typically exemplifies such natural products of plant origins, and has won significant attention by researchers due to reported therapeutic activities, especially CRC (7,8). However, the use of CUR is limited by its low aqueous solubility, poor cellular uptake, instability in aqueous condition and hence poor bioavailability (8). Several approaches have been proposed to address the poor bioavailability of CUR. Structural modification of CUR through conjugation to other

compounds is one approach to enhancing the biological activities of CUR as an anticancer agent (9). Moreover, CUR encapsulation into various formulations such as liposomes(10), micelles (11) and nanoparticles(6) have also been explored as means to improving its therapeutic performance.

In the present study, the main aim is to improve the solubility of CUR through structural modifications of CUR by conjugation to succinic acid. These would then be encapsulated in mannose conjugated chitosan nanopolymeric system. The cellular uptake propensity of the nanoparticles will be assessed as well as the anti-colon cancer-targeting propensity on cancer cell lines. Nanoparticulate dosage forms are ideal delivery systems for drugs due to their extensive surface area to volume ratio, which provides a potential protection of the carried drug from degradation. The prepared formulation is intended for oral administration and is expected to display requisite stability in simulated GIT media until arrival at the colon where uptake and degradation occur. It is anticipated that the prepared formulation would provide a better safety profile and improved therapeutic effectiveness as the used materials are originating from natural sources, and thus serves as a potential and safe therapy for CRC. A review of key aspects that serve as the building blocks to the execution of the project is outlined below.

1.2 Colon and colorectal cancer

1.2.1 Anatomy of the colon

Anatomically, the colon, also named the large intestine, is a muscular tube of 1.5 m length that extends from the ileocaecal valve till the rectum region (12), which is the distal part of the GIT. The colonic region can be divided into 3 regions: (i) the ascending colon, 0.15 m in length and stretches vertically up starting from the ileocecal junction until the inferior surface of the right part of the liver (Figure1). At this stage, it bends to form the right hepatic flexure, and later it binds continuously with the

transverse colon. (ii) the descending colon, about 0.25 m in length and stretches vertically from the splenic flexure until the left iliac fossa where it binds continuously with the sigmoid colon (iii) the sigmoid colon, 0.35-0.40 m in length and crosses the pelvic brim, joining the pelvic cavity and binds continuously with the rectum (12,13). The colonic region is highly viscous due to its large water absorption capacity, which makes the luminal walls thickly layered by mucus. This thickness impeded drug dissolution and lowers absorption(13). A mucus layer covers the epithelial cells including named goblet cells that line up the colonic lamina propria connective layer, producing a single mucus cover layer (2,13). Generally, the mucus layer comprises of mucin glycoprotein, inorganic salts, water, and lipids (13).

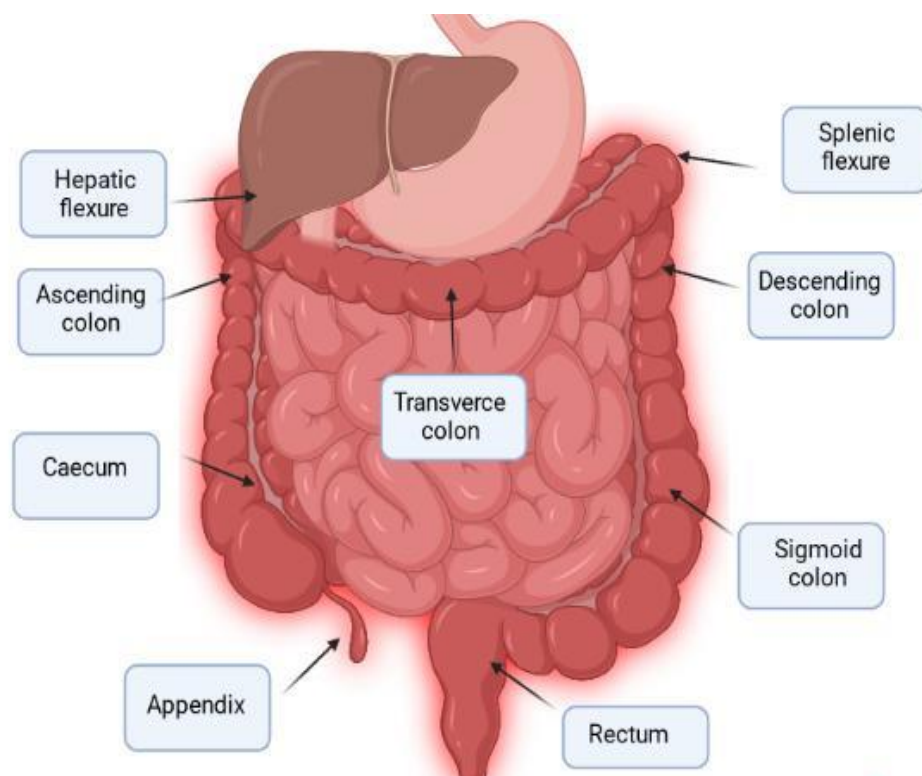


Figure 1. Colonic region representation.

Histologically, the colon comprises several concentric layers including columnar epithelium, lamina propria, muscularis mucosae, submucosa, muscularis propria (includes an outer longitudinal layer and an inner circular layer of smooth muscles), and serosa (14). In the colonic region, the mid colon has a pH of ~ 6.6 , while the left colon has a pH value of 7.0 (15). The human colon serves three key functions: (i) capacity function, related to absorption of water and electrolytes and evacuating stool; (ii) a reservoir function, (iii) a metabolic function associated to complex impacts on body metabolism pathways (16,17).

Within the colon, there are over 400 different species of aerobic and anaerobic bacteria. Moreover, these bacteria ferment carbohydrates, and produce short-chain fatty acids (SCFAs) (14). Colonic dysfunction can be categorized into two broad categories: (i) disorders related to motility, which manifests as constipation, diarrhea, irritable bowel syndrome and diverticular diseases, (ii) colonic mucosal diseases, which could be due to infestation, carcinoma, polyps, inflammatory bowel diseases (14). Furthermore, the colonic tissue may be probe to other diseases including ulcerative colitis (UC) and Crohn's disease (CD). Frequently, these ailments are treated using several drugs including dexamethasone, sulfasalazine metronidazole, hydrocortisone, and prednisolone (18).

Treatment of colonic dysfunction can be brought through oral or rectal administration of drugs, with ultimate deployment to the colon. In this regard, colon-targeted functionality of the delivery system provides specificity and better treatment outcomes, with minimized systemic side effects. Overall, oral administration is preferred over the rectal route due to patient convenience and compliance (18). Moreover, orally administered dosage forms take up the majority of manufactured delivery systems, hosting safe and safe profiles of the pharmaceutical ingredients.

1.2.2 Colorectal cancer

Worldwide, the incidence and mortality from CRC have risen sharply in the past decades, due to sedentary lifestyle and unhealthy food consumption habits. It was reported by the International Agency for Research on Cancer (IARC) that in 2018, 1.8 million CRC cases were recorded, representing 10% of all cancer cases (19), while deaths cases reached 800,000 accounting for about 9% of cancer related deaths. Furthermore, the World Health Organization (WHO) presents that cancer accounted for 10 million deaths in 2020, of which CRC contributed to 1.93 million cases (19.3%) (20). In the State of Qatar, the National Cancer Registry of the Ministry of Public Health (MoPH) recorded that the most common cancer is breast cancer with 16.58% of all cancer cases, followed by CRC at 9.44% (21). Majority of CRC cases are sporadic, while around 5–10% of CRC cases are defined as hereditary (22). Early stages of CRC presents no major symptoms, but may be non-specific, including constant tiredness, abdominal discomfort, changes in bowel habits, and weight loss without apparent reasons (23). Several staging standards are used to assess the progression of the disease within the colon and summarized in Figures 2, 3, and 4 (23–25).

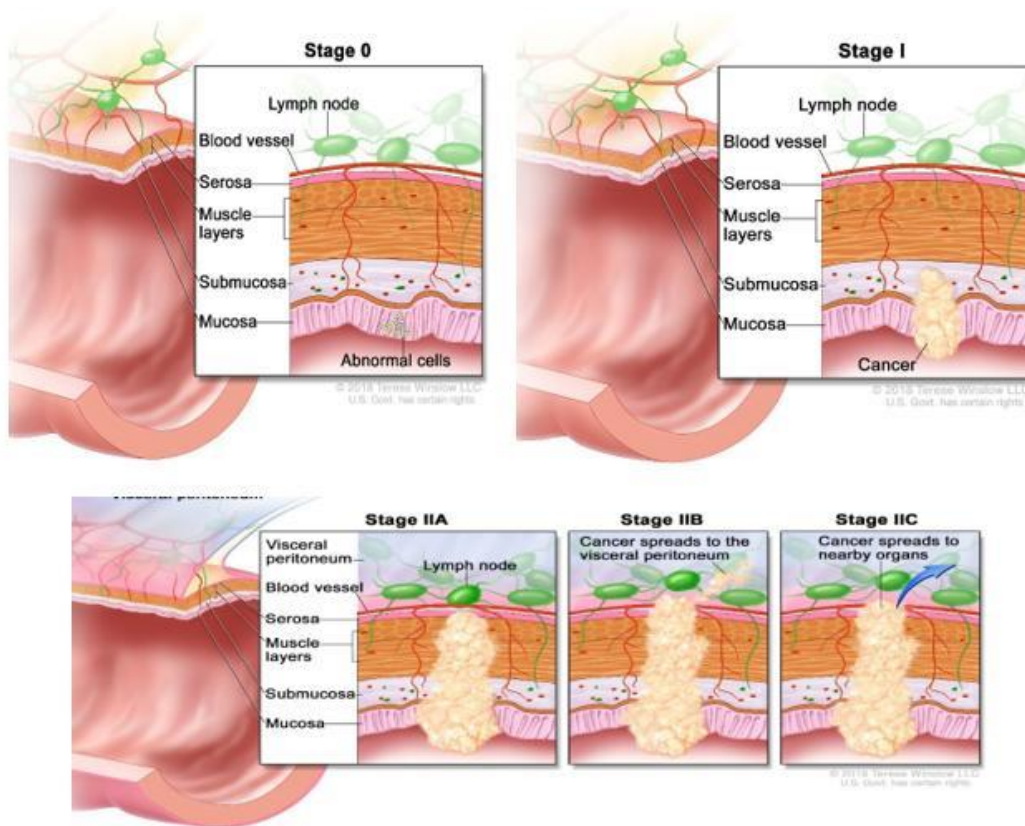


Figure 2. Graphical illustration of stages 0, I, and II of CRC, adapted from (25). In stage 0, the tumor confines to mucosa layer, which is the innermost layer of the colonic wall. In stage I, the cancer cells start to expand towards the submucosa layer. In stage II, the tumor starts to invade through the muscle layer towards the serosa layer, followed by tissues that border the adjacent organs inside the abdomen, finally up to neighboring organs.

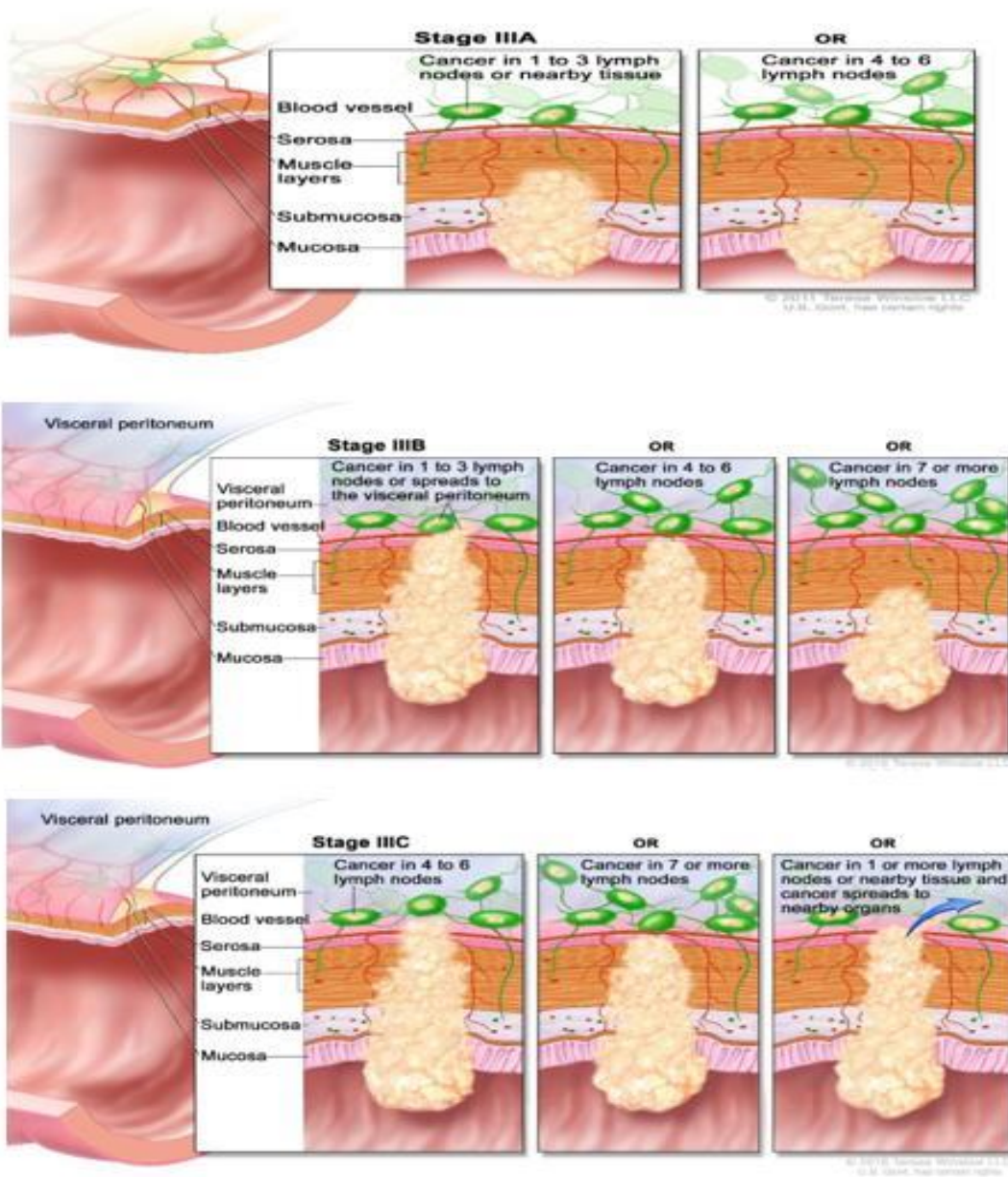


Figure 3. Graphical illustration of stage III of CRC, adapted from (25). In the stage IIIA, cancer started to spread in 2 pathways: (i) across the mucosa towards the submucosa until it reaches one to three nearby lymph nodes, (ii) or to spread inside four to six adjacent lymph nodes. In stage IIIB, the tumor has invaded up to seven or more adjacent lymph nodes. In stage IIIC, the tumor continues to spread until it develops inside tissues close to the lymph nodes.

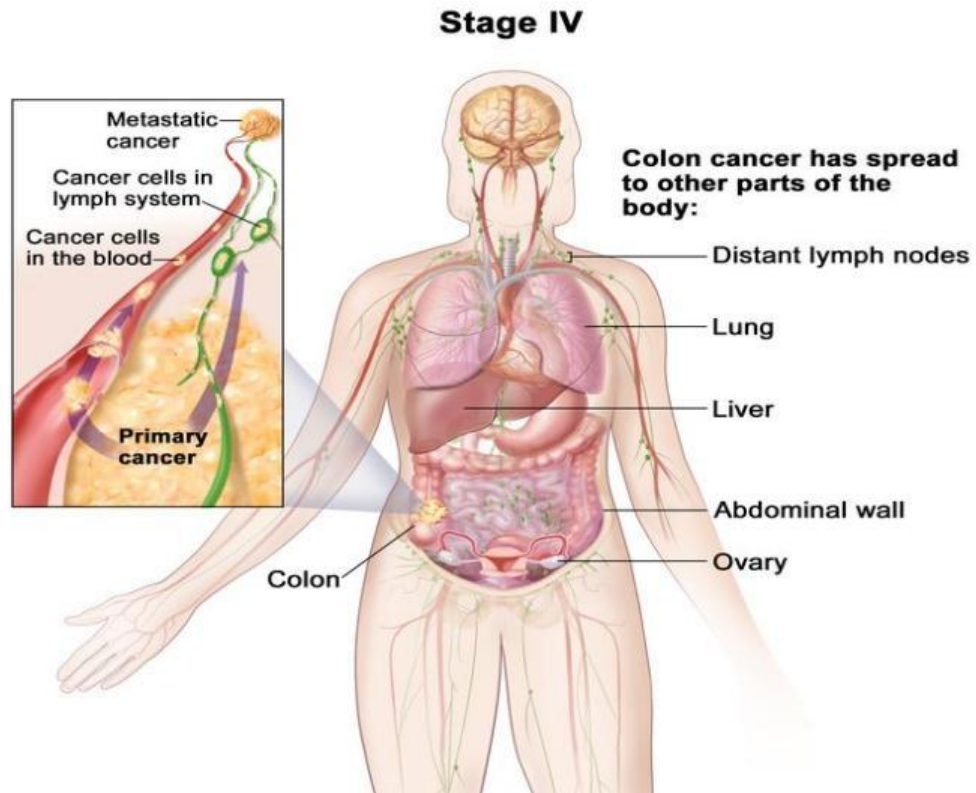


Figure 4. Graphical illustration of stage IV of CRC, adapted from (25). In this stage, the tumor has invaded to one area or organ that are far from the colon, such as towards the lung, liver, ovary, or a distant lymph node.

Early screening is a very effective strategy that reduces mortality from CRC. Screening includes fecal occult blood test (FOBT), double contrast barium enema, endoscopy, flexible sigmoidoscopy, Multitarget stool DNA testing (mt-sDNA), and colonoscopy (13,22,26). FOBT is the widely used option and has contributed to a decline in CRC by 25% (27).

1.2.3 Drug delivery to colon

To be successfully deployed to the colonic region, a drug formulation must retain its integrity throughout the GIT until arrival at the colon in order to avoid premature drug release, which will reduce the effectiveness of the administered dose. Several approaches on formulations have been developed for the colonic delivery of APIs and these are reviewed below.

1.2.3.1 Use of prodrugs

A prodrug is an inactive medication that is converted enzymatically or otherwise into a pharmacologically active drug after administration (28,29). Prodrugs can be used to improve the aqueous solubility of poorly soluble drugs. It can also be used to achieve targeted release. For example, sulfasalazine (SLZ or salazopyrin) is a colon-specific azo prodrug used in UC (30). After oral administration, only a small portion of SLZ is absorbed by the small intestine and 90% reaches the colonic. In the colon, the azo bond within the SLZ is cleaved by the colonic bacteria to liberate sulphapyridine and 5-aminosalicylic acid (5-ASA) (Figure 5).

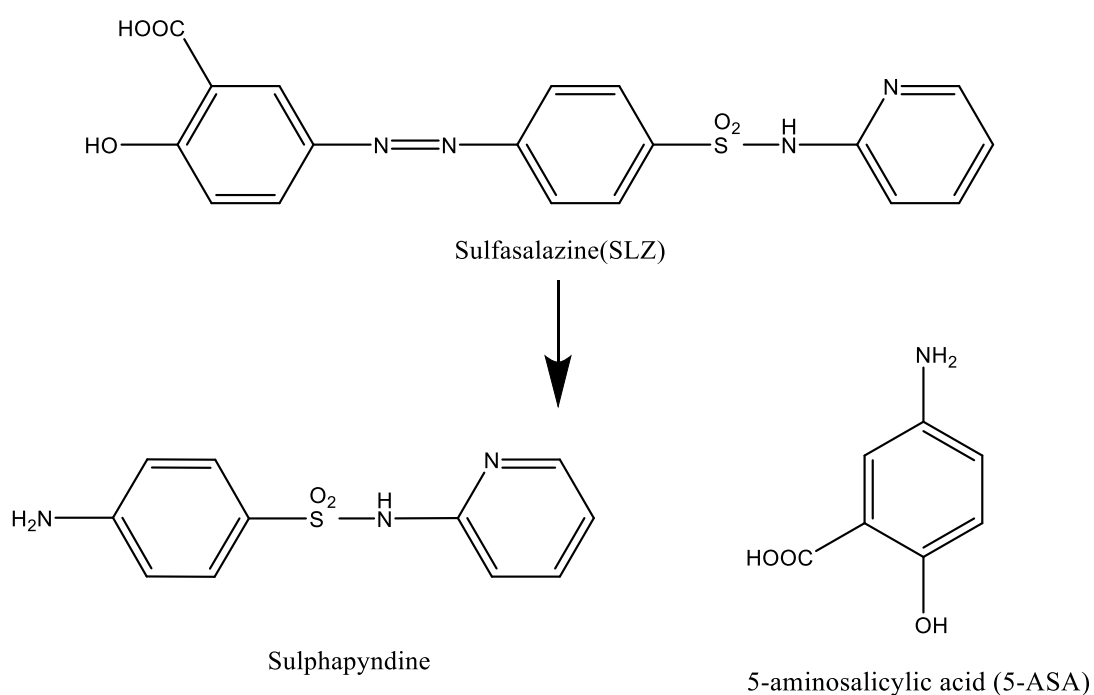


Figure 5. Representation of the hydrolysis pathway of sulfasalazine into sulphapyridine and 5-aminosalicylic acid.

1.2.3.2 Application of pH-sensitive polymers

The pH of the GIT is highly variable and influenced by the disease state of the colonic region, diet uptake, and exhibits intra-subject variability (31). For example, colonic pH decreases in Crohn's disease, which is a relapsing systemic inflammatory

disease that occurs in the GIT (31,32). This variability affects the solubility of drugs in a variety of ways, based on their pKa and thus can be exploited to prompt release accordingly. The pH in the stomach region is 1 – 3.5 so that it is possible to carefully select polymers that are irresponsive at these proximal pH values, but which are responsive at pH values of the colon. Such polymers are enteric polymers (33) and several are in use for delayed drug release in the GIT. For example, aminoalkyl methacrylate copolymer (Eudragit E) approved by the FDA is a cationic polymer which dissolves at above pH 5. Other examples of enteric polymers are summarized in Table 1 (33,34). One drawback about enteric polymers is the imprecision in pH trigger due to variability in GIT pH, thus a substantial amount of drug could be lost in the small intestine before it reaches the colonic region (35).

Table 1. Examples of enteric polymers and pH threshold.

Polymer name	Dissolution pH
Eudragit L100-55	≥ 5.5
Eudragit L30D-55	≥ 5.5
Eudragit L-100	≥ 6.0
Eudragit L12,5	≥ 6.0
Eudragit S-100	≥ 7.0
Eudragit S12,5	≥ 7.0
Eudragit FS30D	≥ 7.0

1.2.3.3 Time-dependent formulations

Time-dependent delivery systems can be used for colon-targeting based on the release of drug cargo at a predefined time (36,37). The principle of this approach is to postpone the drug release time until it reaches the colonic region. For instance,

Budesonide capsules were approved by the FDA for treating mild and moderate active CD, including the ileum and/or the ascending colonic region (Figure 6). Furthermore, Entocort™ EC is a trade name of Budesonide that was established to combine the pharmacological aspects of budesonide and deactivation in the liver with local and time-dependent release inside the ileum and ascending colonic region to treat Crohn’s disease (38). One disadvantage of time-dependent formulations is that gastric emptying varies significantly between subjects, and it depends on the type and amount of food intake. Also, diseased states can affect the timing of release, for example premature deployment of the dosage form is observed in patients with IBD. (39).

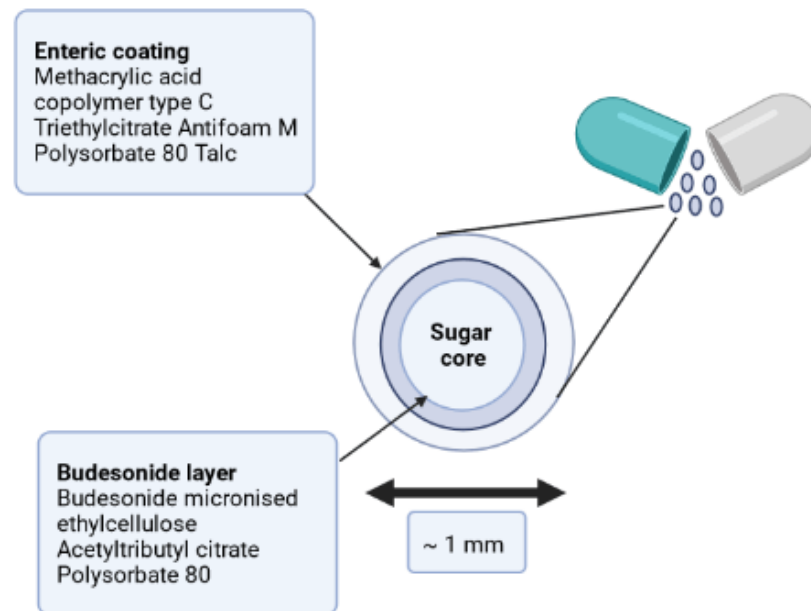


Figure 6. Illustration on the composition of budesonide granules of Entocort™ EC.

1.2.3.4 Microbially-triggered systems

The colonic microflora comprises anaerobic bacteria including *Bacteroides*, *Bifidobacteria*, *Clostridia*, and *Ruminococcus* species that satisfies their energy needs through fermentation of undigested substrates by glucoronidases, xylosidases, and arabinosidases type enzymes (40,41). Microbially-triggered systems represent a

potential for drug delivery systems comprised of non-starch polysaccharides, primed to degrade only in the colonic region (42). However, the enzymatic degradation of a polysaccharides is a slow procedure that typically take over 12 hours to complete.

1.2.4 Management of colorectal cancer

Rational management of CRC is an important key point to reduce morbidities from CRC. Currently, several treatments options are available, and these are summarized in Figure 7. The type of treatment is usually matched to the needs of the patient such as the stage of the cancer and other health concerns. Generally, less invasive procedures are adopted when the case is not severe. In some instances, it is necessary to combine more than one approach to achieve the best outcomes. Treatments for CRC includes surgery (22,43), radiation therapy(44–47), immunotherapy (48–51), and chemotherapy (52).

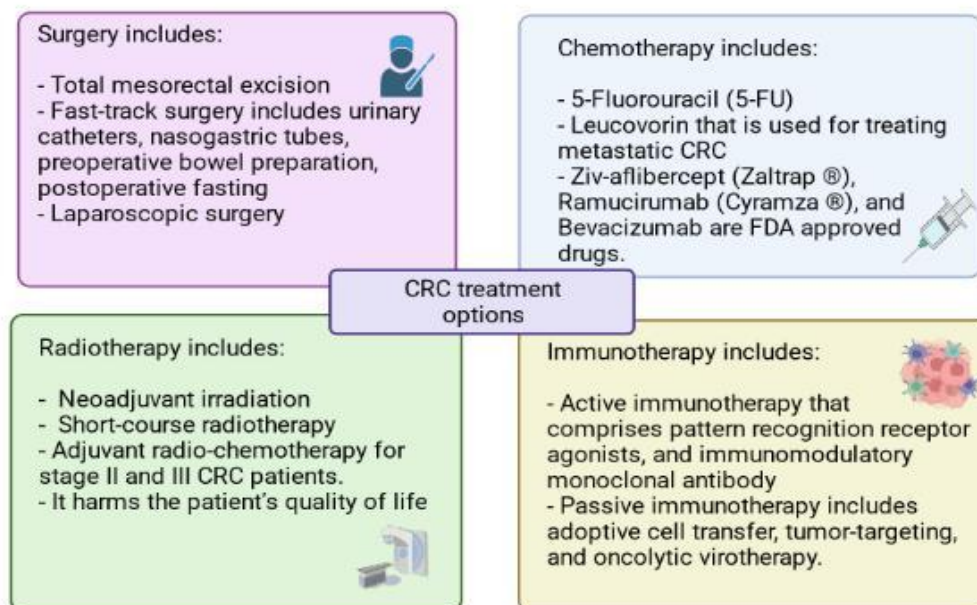


Figure 7. Summary of available treatments for CRC.

1.2.5 Constraints from available treatments

Current CRC treatments are associated with several side effects. In drug resistance, a decline in the therapeutic effectiveness of the treatment (53) occurs so that the same dose becomes ineffective over a period of time. Furthermore, toxicity is another constraint because of the non-specificity to cancer cells (54). On the other hand, several herbal remedies have been found to provide better anti CRC treatment outcomes and thus there is an intensified research interest in studying the therapeutic profiles of some of these constituents (51). In the past few years, more natural products have emerged with formidable potential for use in CRC. Some of these exhibit anti-carcinogenic activities through interference with the initiation, development and progression of cancer through modulating several mechanisms such as cellular proliferation, apoptosis, differentiation, metastasis, and angiogenesis (55). Crucially these agents manifest fewer side effects compared to their chemotherapeutic cousins of synthetic agents(55,56). One such anticancer agent that has won wide attention by researchers is curcumin, the main constituent obtained from the plant *curcuma longa* (7,8). A review of the chemical properties of curcumin is presented below.

1.3 Curcumin

Curcumin (CUR) is a compound present in the rhizome of *Curcuma longa L*, which is a tuberous herbaceous perennial plant belonging to the ginger family native to tropical climates (57). The plant contains two other related compounds: demethoxycurcumin and bis-demethoxycurcumin (Figure 8). Together, these three compounds are named curcuminoid (58). CUR is a crystalline compound that has a bright orange-yellow color. According to the WHO, the acceptable daily intake of CUR is up to 3 mg/kg (58). The therapeutic uses of CUR have been investigated in detail and includes antioxidant, anti-inflammatory, neuroprotective, hepatoprotective, antimicrobial, anti-inflammatory, and anticancer properties (57,59).

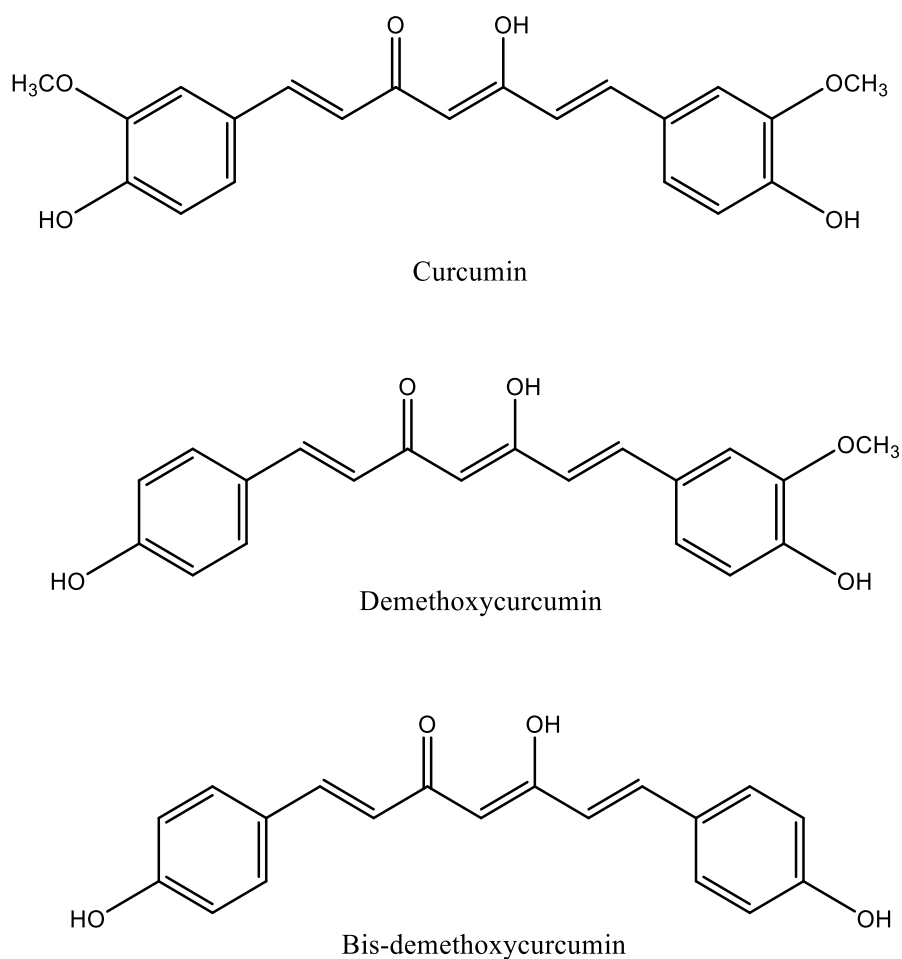


Figure 8. Chemical structure of Curcumin, Demethoxycurcumin, and Bis-demethoxycurcumin.

1.3.1 Chemical and physical properties of curcumin

CUR, (diferuloylmethane), is a diaryl heptanoid photochemical (7,60). The chemical name of CUR is 1,7-bis(4-hydroxy-3-methoxyphenyl)-1,6-heptadiene-3,5-dione. In 1842, CUR was isolated for the first time from a mixture of turmeric oil and resin by two German scientists named Pelletier and Vogel (61). It has a melting point of 183°C, and a molecular mass of 368.37 g/mol, insoluble at acidic and neutral pH, whilst soluble in nonpolar organic solvents such as dimethylsulfoxide (DMSO), ethanol, and acetone (8). CUR undergoes keto-enol tautomerism based on the acidity of the solution. The keto-form is dominant in acidic or neutral, whilst enol-form is dominant in alkaline media, stabilized through resonance-assisted hydrogen bonding

(58). CUR stability is maintained up to 70°C for 10min and beyond this temperature, it starts to decompose (62). CUR has 3 pKa values, where $pK_{a1}=7.75-7.80$, $pK_{a2}= 8.55$, and $pK_{a3}= 9.05$ (58). CUR has an absorption spectra between 408 – 430 nm, while its emission maximum falls between 460 – 560 nm in several organic solvents (63).

1.3.2 Anti-colon cancer activity of curcumin

CUR exhibits its anticancer properties through a wide range of actions at subcellular including apoptosis and inhibition of proliferation (64). Figure 9 summarizes key pathways involved in the initiation and progression of and anticancer activity of CUR (65).

In Wnt/ β -catenin signaling pathway, CUR acts as a blocker of the Wnt/ β -catenin signaling, which performs a vital role in the pathogenesis of CRC and reduces glypican-3 (GPC3) expression. Further, downregulating GPC3 would hinder the expression of β -catenin, c-myc and cyclin D1, which enhances CUR inhibitory effect the Wnt/ β -catenin signaling. When β -catenin accumulates in the cytoplasm, it translocate towards the nucleus and stimulates the expression of various oncogenes and epithelial-mesenchymal transition (EMT)-inducing transcription factors. EMT is linked to the initial stage of cancer invasion and metastasis where the cancer cells start to lose the epithelial cells characteristics, and to gain mesenchymal phenotypes and to spread towards the surrounding tissues (66). Thus, CUR suppresses the EMT process in cancer cells by inactivating the Wnt/ β -catenin signaling.

When ligands such as growth factors and cytokines got attached to their equivalent receptors, an activation of downstream signaling pathways is induced including PI3K/Akt, JAK/STAT, and MAPK signaling pathways as it has a vital role in cell survival, apoptosis, proliferation, angiogenesis, metastasis, and invasion (65).

In other words, CUR is able to coordinate these three pathways and acts as a potential agent in cancer progression. When Akt is activated, p53 signaling and Bad-mediated apoptotic pathway, which promotes the tumor cell survival, are restrained. Moreover, Akt introduces initiation of the NF- κ B signaling pathway. NF- κ B, is a ubiquitous transcription factor responsible in regulating several genes involved in inflammation, growth regulation, carcinogenesis, and apoptosis (67). NF- κ B stimulates the expression of anti-apoptotic proteins such as B-cell lymphoma-2 (Bcl-2) and B-cell lymphoma-extra-large (Bcl-xL), which inhibits cancer cell apoptosis (65,68). Thus, CUR inhibits the activity of NF- κ B, which facilitates cancer cell apoptosis (69). In addition, CUR induces the deactivation of the JAK/STAT pathway through suppressing the phosphorylation of JAK and STAT3, which results in downregulating vascular endothelial growth factor (VEGF), Bcl-xL, and cyclin D1 (70).

In MAPK signaling pathway, where MAPKs are a big family of serine/threonine kinases, MAPK signaling cascades are responsible of regulating various biological activities including carcinogenesis and cell proliferation (65,71). For instance, CUR was found capable to reduce the cell viability of retinoblastoma and has induced the apoptosis of Y79 cells through activating p38 MAPK and JNK pathways (72). Moreover, CUR induced growth and invasion inhibition of human monocytic leukemia SHI-1 cells through the regulation of MAPK signal transduction. Furthermore, cancer cell growth was extensively suppressed after administrating CUR.

In PI3K/Akt pathway, several cellular processes such as cell proliferation and metabolism are controlled, and misregulating PI3K/Akt signaling pathway is frequently linked with cancer progression and carcinogenesis (73,74). For instance, CUR has induced cell cycle arrest through inducing downregulation of cell division cycle 25 (CDC25) and CDC2 and upregulation of p21, which is a cyclin-dependent

kinase (CDK)2/6 inhibitor (75). Furthermore, CUR, has induced cell cycle arrest by suppressing the Akt/mTOR pathway as it has deactivated the Akt/mammalian target of the rapamycin (mTOR) signaling. Moreover, CUR reduced Bcl-2, upregulated B-cell lymphoma-2 (Bax), and cleaved caspase-3, which promotes apoptosis of breast cancer cell. Furthermore, CUR induced cell death, apoptosis, and autophagy were improved through inhibiting PI3K and regulating Bcl-2 family members expression in breast cancer cells, which proves that inactivating the PI3K/Akt pathway could enhance CUR antineoplastic effects against breast cancer (65).

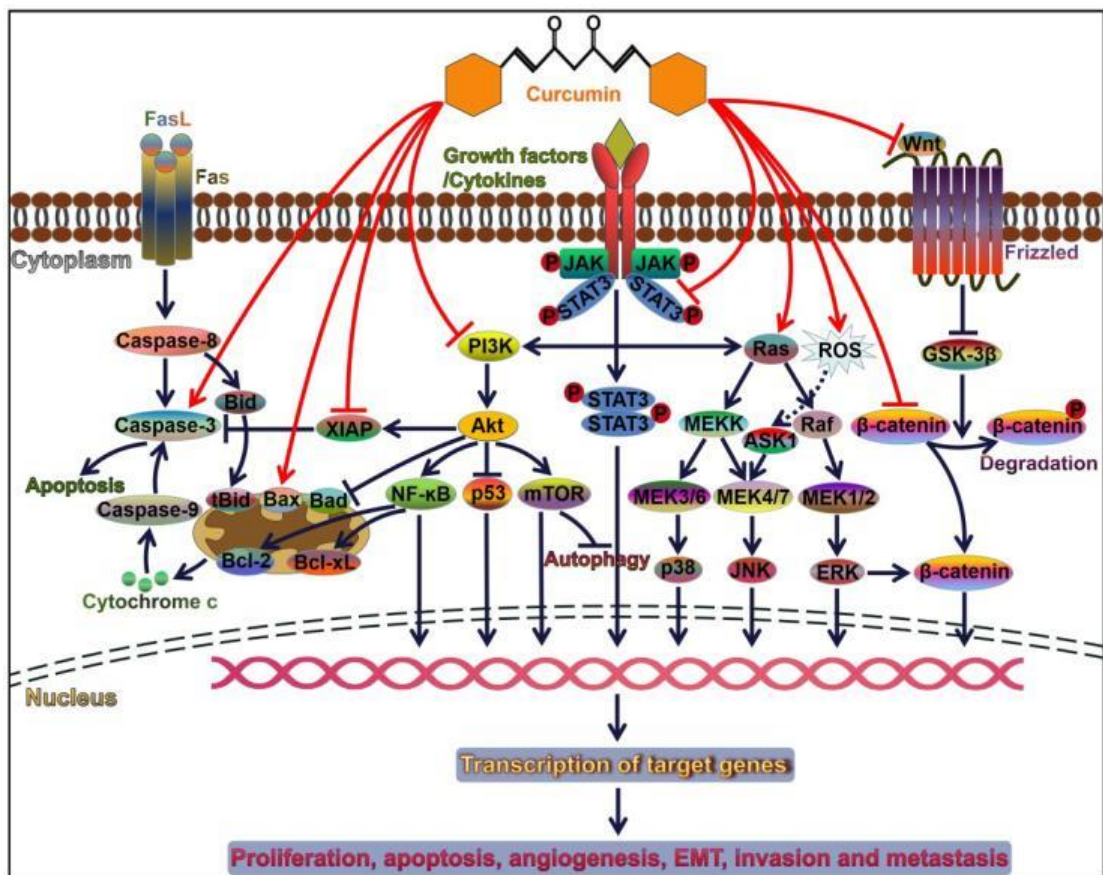


Figure 9. Summary of CUR modulation pathways of cancer progression and regulation of signal transduction pathways, adapted from (65).

1.3.3 Combination therapy with curcumin

Due to its proven anti CRC effects, research has been aimed at further probing the effectiveness of CUR in combination with conventional chemotherapeutic regimen. For example, 5-FU in combination with CUR showed a time- and dose-dependent efficacy on CRC cell lines (HCT116) (76). The results demonstrated that CUR had significantly improved the cytotoxicity of 5-FU against HCT116 cell lines at concentration of 0.1 mM 5-FU. Moreover, the combined treatment significantly enhanced the chemosensitivity effect of 5-FU to HCT116 cell lines compared to 5-FU alone. In another study, polyethylene glycol (PEG)-ylated liposomes containing CUR and doxorubicin demonstrated anticancer effects on murine colon carcinoma cells (C26) (77). The liposomes exhibited significant antiproliferative and improved cytotoxicity towards C26 cells, compared to doxorubicin alone. In another study, a series of chitosan-functionalized camptothecin and CUR loaded nanoparticles were found to exhibit dose-dependent synergism, especially at 4:1 camptothecin/CUR against Colon-26 cells (78). CUR doses of 10-15 $\mu\text{mol/L}$ and celecoxib (5 $\mu\text{mol/L}$) induced synergistic inhibitory effects on cell growth, whereby inhibition was linked with induction of apoptosis and celecoxib inhibition of prostaglandin E2 synthesis (79).

1.3.4 Clinical trials conducted on curcumin

The anticancer activity of CUR investigated on various cancers, including CRC in animal (80–83) and in human CRC trials showed that doses in the range of 0.45-3.6g daily for 4 months (84) was effective. A daily uptake of 3.6 g CUR caused inhibition of prostaglandin E2 (PGE2) induction, but glutathione S-transferases (GST) activity was not affected at this dose. In another phase I trial, CUR liposomal formulation was studied on 32 patients with advanced or metastatic cancer for safety and tolerability. Doses ranged between 100 mg/m^2 over 8 hours to 300 mg/m^2 over 6

hours, where no dose-limiting toxicity was observed among 26 patients (85). A cohort of 50 healthy subjects involved in phase I clinical trial to assess the performance of intravenously administered liposomal CUR at concentrations between 10 – 400 mg/m² over 2 hours, showed that the liposomal CUR was well tolerated up to 120 mg/m² (86). Furthermore, CUR containing exosomes were used to deliver CUR to the colon in a phase I clinical trial. Up to 2022, this on-going trial is aimed at assessing the efficacy of exosomes in deploying CUR carrier to normal and colon tumor (87). A summary of current on-going clinical trials assessing the anticancer effects of CUR against CRC and colon related diseases is shown in Table 2 below.

Table 2. Summary of CUR on-going trial as anti-CRC and colon related diseases drug.

Trial	Trial stage	Disease target	Number of patients	Main objectives
Curcumin in Combination With 5FU for Colon Cancer NCT02724202	Phase I	CRC	13	<ul style="list-style-type: none"> • To identify clinical response rate of combination between CUR and 5FU in CRC patients. • To determine CUR administration effect on systemic alterations in inflammatory and epigenetic biomarkers in patients with chemo-resistant metastatic CRC.
Study Investigating the Ability of Plant Exosomes to Deliver Curcumin to Normal and Colon Cancer Tissue NCT01294072	Phase I	CRC	35	<ul style="list-style-type: none"> • To assess the ability of plant exosomes in delivering CUR to normal and colon tumor cells. • To address the limited bioavailability of CUR delivery by using plant exosomes
Plant Exosomes +/- Curcumin to Abrogate Symptoms of Inflammatory Bowel Disease NCT04879810	NA	IBD	90	<ul style="list-style-type: none"> • to evaluate the safety and tolerability of exosomes with and CUR in patients with IBD and on the symptoms and disease score in patients with refractory IBD.
Curcumin for Prevention of Relapse in Patients with Ulcerative Colitis NCT03122613	NA	UC	172	<ul style="list-style-type: none"> • To assess the efficacy of CUR in preventing relapse in patients with ulcerative colitis.

*NA: Not applicable.

1.3.5 Physicochemical and therapeutic constraints on effectiveness of curcumin

Even though CUR demonstrates proven therapeutic benefits, its implementation is still limited due to poor aqueous solubility (11 ng/mL) (88), instability in aqueous media, especially alkaline pH (89), all of which contribute to poor cellular uptake (9) and hence low bioavailability. Additionally, CUR is significantly metabolized and rapidly eliminated from the body (88). At pH>7, complete degradation of CUR occurs during 30 mins to Trans-6-(40-hydroxy-30-methoxyphenyl)-2, 4- dioxo-5-hexanal, feruloylmethane, ferulic acid, and vanillin (88); whilst at pH<7, CUR degradation is slow with less than 20% of total CUR decomposing in 1 hour. Moreover, CUR undergoes rapid conversion into water-soluble metabolites, including glucuronides and sulfates, which facilitate rapid clearance through urine. CUR metabolism occurs through Phase I and Phase II schemes (90–92). In Phase I, double bonds of the heptadiene-3, 5-dione are reduced by NADPH-dependent CUR/dihydrocurcumin reductase enzyme. In Phase II, CUR and its reduced metabolites from phase I are conjugated along with monoglucuronide through β -glucuronidase (Figure 10). Thus, these limitations have restricted CUR clinical applications.

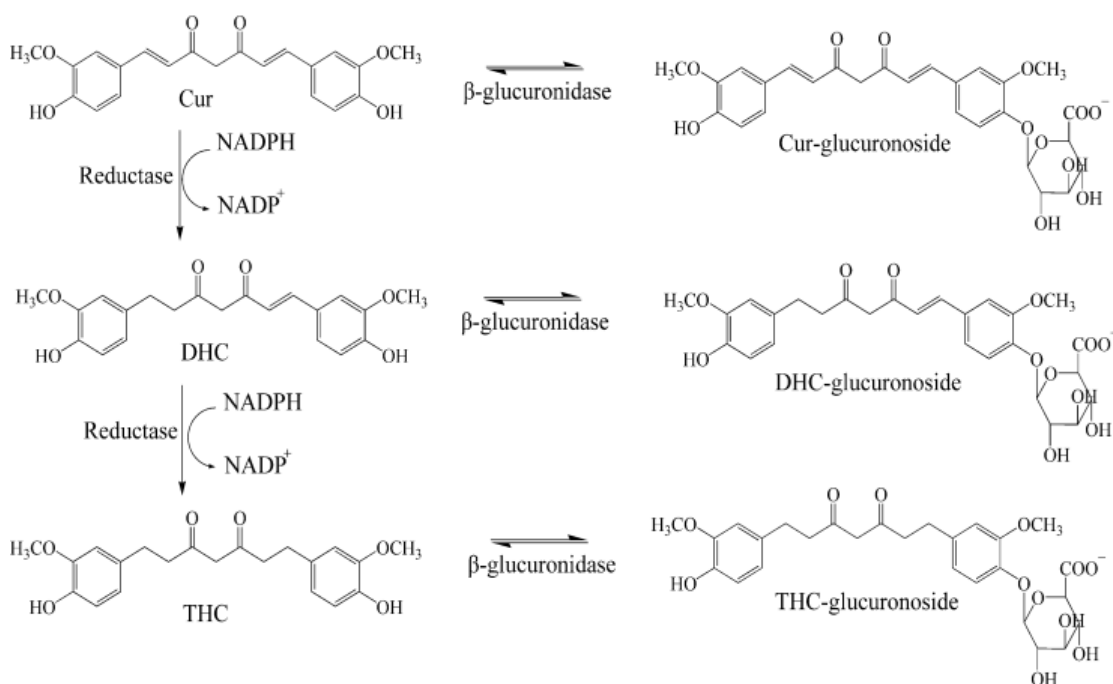


Figure 10. Biotransformation and CUR metabolites, adapted from (88).

1.3.6 Strategies used to overcome physicochemical and therapeutic limitations of curcumin

Researchers have probed various strategies aimed at addressing the constraints akin to CUR therapeutic applications. One strategy that appears to have good traction is chemical modification of CUR or synthesis of CUR derivatives in an attempt to enhance its therapeutic effectiveness, whilst at the same time addressing its physicochemical limitations (93,94). Furthermore, CUR formulation approaches, especially through nanoencapsulation have been probed as a further frontier in addressing the aforementioned constrains.

1.3.6.1 Conjugation of curcumin with relevant moieties

Interests towards synthesizing newer CUR derivatives have grown in recent years, with some success made with regard to some of the limitations associated with the therapeutic use of CUR. Some of these analogues present superior anticancer

properties than free CUR. For example, dimethylaminomethyl-substituted CUR analogues were more stable and soluble than free CUR, but crucially more effective on HCT-116 cell lines (95) compared to free CUR. In another study, a series of CUR succinyl analogs of CUR were less prone to degradation at pH 7.4 compared to CUR prepared (94).

1.3.6.2 Curcumin and nanotechnology

Nanotechnology is considered among the promising technology that with far-reaching consequence in medicine and science. Nanotechnology was introduced to drug delivery with the aim of achieving better therapeutics that current therapeutics cannot surmount. For example, site-specific delivery can be achieved through nanotechnology, whereby reduction in toxicity can be linked with effective treatment outcomes. Improved solubility is tunable from poorly soluble drugs and prolonged drug release profiles can be achieved. Improved uptake from the gastrointestinal tract ensures better bioavailability enhanced drug biodistribution (96,97). The targeted nanocarrier is designed based on the administration route, release profile, circulating pathway, and types of carrier system (98). For instance, polymeric nanoparticles, micelles, liposomes, nanogels, and gold nanoparticles are among the most common types of nanocarriers. Every carrier has distinctive physicochemical properties and distinctive in vitro and in vivo performance, and these will be elaborated subsequently.

1.3.6.2.1 Polymeric nanoparticles

Polymeric nanoparticles (NPs) are polymer-based formulations, usually biodegradable and consist of spherical morphologies in the nano-size (Figure 11). Drug is either encapsulated or physically entrapped within the polymer matrix (nanospheres), or encapsulated inside a cavity bordered by a polymeric membrane, (nanocapsules) (99). These carriers provide a host of advantages including protective

properties, possibility to cargo and deliver multiple drugs, decreased toxicity and improved uptake by cancer cells (100). Furthermore, polymeric nanoparticles possess stability and are homogeneous with controllable physicochemical properties and drug release profile (100,101). Thus, the bioavailability and therapeutic properties of the carried drug are potentially improved. Several FDA approved polymers have been studied, including N-(2-hydroxypropyl)-methacrylamide (HPMA) copolymer, polyglutamic acid and polyglycolic acid (PGA), PEG, polylactic acid (PLA), polyaspartate (PAA), and poly(D,L-lactide-co-glycolic) acid (PLGA) (100,102). On the other hand dextran, albumin, collagen, and chitosan are non-toxic, biodegradable and inexpensive (100,103). Polymeric NPs have been widely studied in delivering CUR as anti-CRC agent.

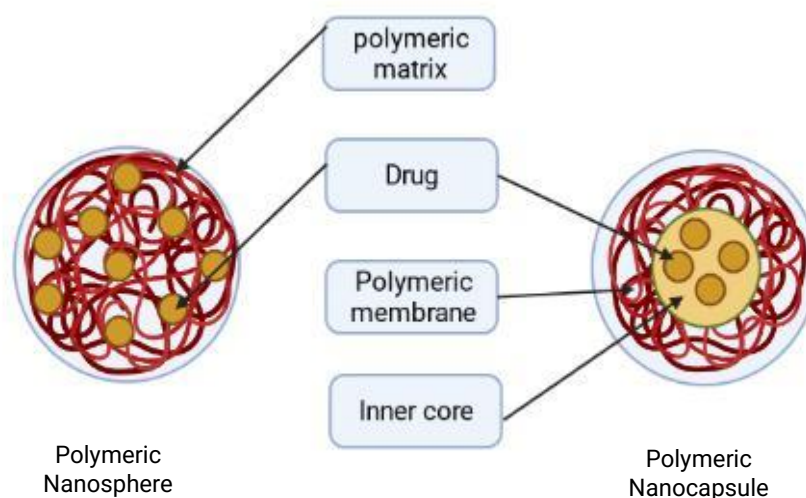


Figure 11. Graphical illustration of polymeric NPs.

1.3.6.2.2 Micelles

Polymeric micelles (Figure 12) are spherical nanoscopic core/shell structures, with a size that ranges between 10 to 100 nm (104). Micelles are consist of amphiphilic copolymers that have distinct hydrophobic tail and a hydrophilic head (105). Generally, the hydrophilic head is made of PEG , while the hydrophobic tail

represents polyethers, polyesters, polyamino acids including poly(ϵ -caprolactone) (PCL), PLA, poly(L-aspartic acid), and poly(propylene oxide) (PPO) (106). Micelles improve the stability of APIs and promote gastrointestinal uptake and hence bioavailability. They also shield the encapsulated cargo from being degraded or metabolized (107). Micelles are relatively simple to prepare, biocompatible, and can be formulated with tumor targetability properties (105).

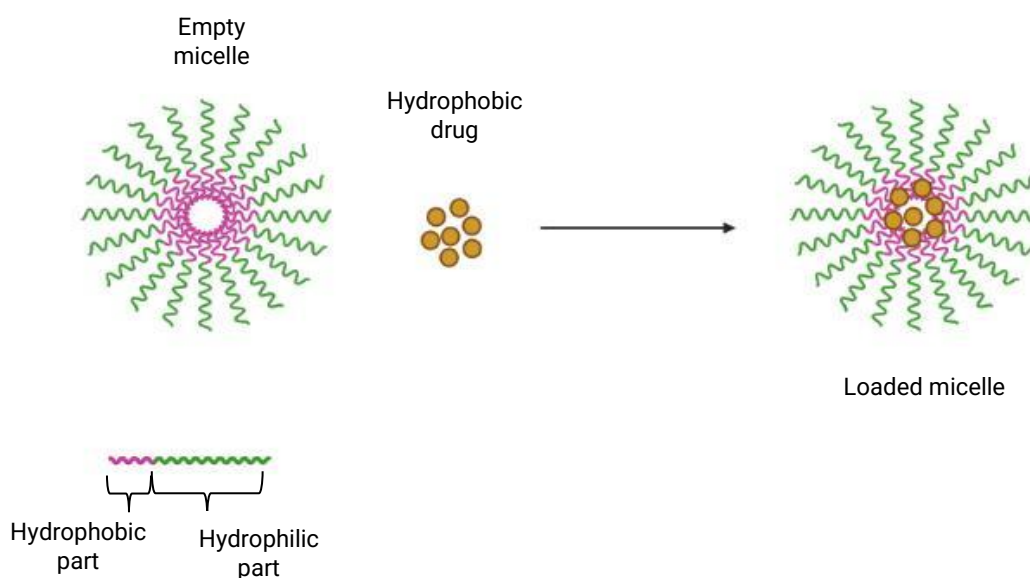


Figure 12. Graphical representation of polymeric micelles used for delivering drugs.

1.3.6.2.3 Liposomes

Liposomes (Figure 13) typically comprise of lipid packed into spherical macrostructure, where a lipophilic bilayer is squeezed between two hydrophilic layers (108). The structure permits loading of hydrophilic APIs within the aqueous compartment and hydrophobic agents inside the lipid space (109). Furthermore, liposomes are more biocompatible than other carrier systems as their composition is similar to that of the cell membranes, which make liposomes useful carries for drug delivery. Liposomes also protect the loaded drug from degradation. Doxil[®] is an anti-cancer chemotherapeutic agent containing doxorubicin within liposomal formulation

approved for treating breast, lung and ovarian cancers (110).

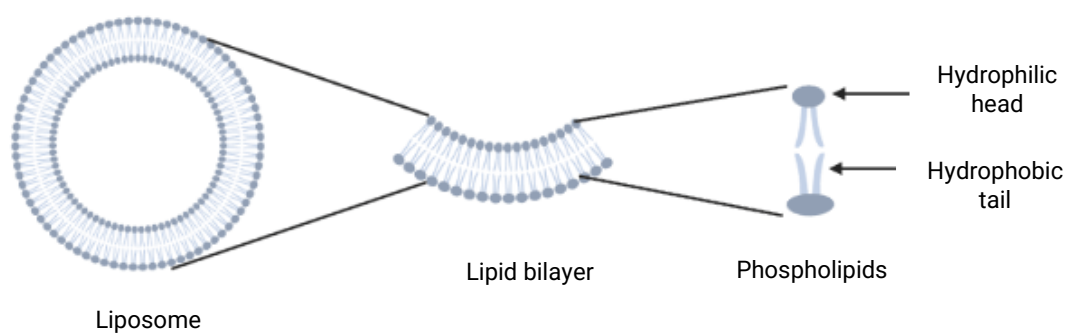


Figure 13. Graphical representation of liposomal carriers for drug delivery.

1.3.6.2.4 Nanogels

Nanogels (Figure 14) are cross-linked hydrophilic delivery systems formed by cross-linking of polymer networks loosely held by hydrophobic or electrostatic interactions (111). Nanogels can be used to deliver chemotherapeutics and they have excellent drug loading capacity, good stability with tumor-specific drug delivery capability (111,112). For example dextran nanogel coated loaded with doxorubicin was used to target breast cancer cells (113).

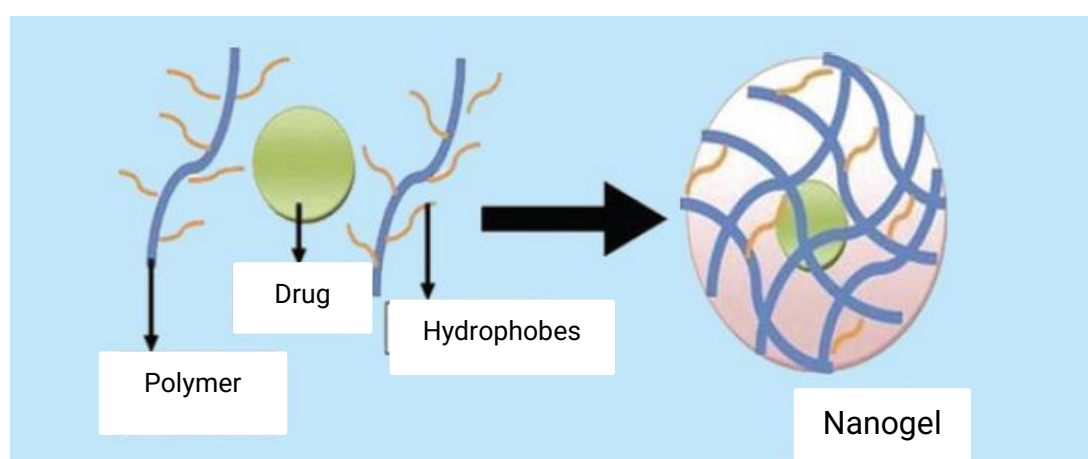


Figure 14. Graphical representation of nanogel carriers as drug delivery systems, adapted and modified from (111).

1.3.6.2.5 Gold nanoparticles

Gold nanoparticles (Figure 15) have high stability and easy synthesis protocols (114). They are non-toxic and non-immunogenic, and possess high permeability and retention, which promotes bioavailability of drug cargoes at cancer sites. Specifically functionalized gold nanoparticles exhibit good biocompatibility and controllable biodistribution properties (115). Gold nanoparticles conjugated to bleomycin maintained cytotoxicity in cancer cells (116).

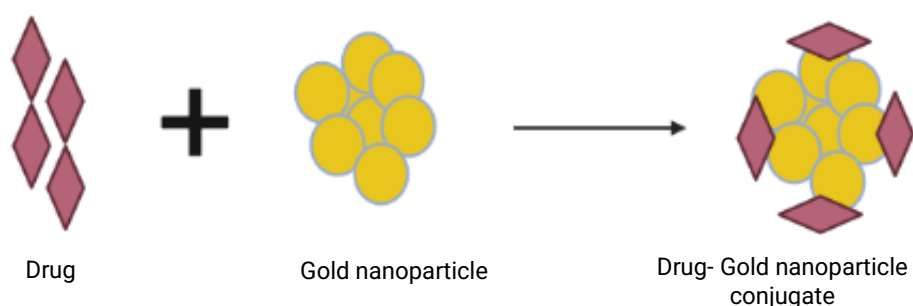


Figure 15. Graphical representation of gold nanoparticles as drug delivery systems.

1.4 Chitosan

Chitosan (CS) (Figure 16) is a high molecular weight and polycationic polysaccharide discovered in 1811 by Henri Braconnot (117). It is isolated from a naturally occurring chitin using alkaline deacetylation in the presence of potassium hydroxide at high temperature (118,119). Chemically, CS is a poly(N-glucosamine) and is poorly soluble in aqueous media but dissolves in acidic media (120) due to protonation of the amine groups (121). Its nontoxicity, biocompatibility and biodegradability (118,122) means it has wide clinical, pharmaceutical and biomedical applications.

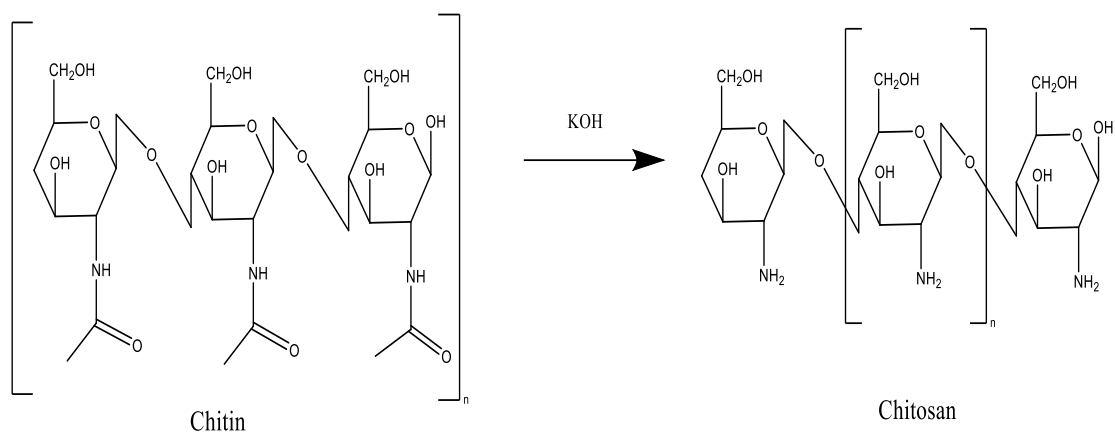


Figure 16. Alkaline deacetylation of Chitin into Chitosan.

Formulated as nanomaterial, CS finds use as antimicrobial agents, used as sensing materials and drug delivery system for the deployment of anticancer agents. CS-based delivery shield API from degraded in the GIT region (120). Furthermore, CS is applied in delivering drugs to the colonic using via tablets (123), CS-based capsules (124), and nanoparticles (125). The positive charge on the chitosan polymer promotes interaction with the negatively charged plasma membrane of mammalian cells, hence mucoadhesion is also favored (126). Thus, APIs encapsulated in NP mucoadheres to cell membranes through electrostatic interactions and successfully delivers the encapsulated drug.

1.4.1 Methods of preparation for polymeric NPs

Several methods are currently available for preparing polymeric NPs. The chosen method is dependent on the type of NPs, the general properties of the encapsulated, the type of used polymer, the prepared NPs properties including size, morphology, encapsulation efficiency (%EE), and drug release profile. The available methods for preparing polymeric NPs will be reviewed below.

1.4.1.1 Solvent evaporation / extraction

Solvent evaporation comprise of single-emulsion (SE) (127) and double

emulsion (DE) (128). In SE-evaporation technique (Figure 17) the organic solution (polymer + drug in water) is dissolved inside a volatile organic solvent (o) and emulsified into an aqueous phase (w). In the second step, the organic solvent is evaporated by either through reducing the pressure or at continuous stirring at room temperature (127,129). Finally, the by polymer is precipitated as nanospheres. In general, the obtained nanoparticles could be retrieved through ultracentrifugation and then rinsed using distilled water in order to remove the excess of free drug. In DE technique (Figure 18), a complex comprised of the droplets from the dispersed phase contain one or more types of smaller dispersed droplets (128). In DE, there are two classes including water-oil-water (w/o/w) and oil-water-oil (o/w/o) emulsions. To prepare DE, two step processes are most frequently followed, in which for w/o/w DE preparation, the inner aqueous phase (W1) is dispersed in oil phase containing lipophilic emulsifier in the first step, which is followed by dispersing the primary emulsion in an outer aqueous phase (W2) that contains a hydrophilic emulsifier (128,130). Finally, an evaporation process of organic solvents takes place and the particles are precipitated out. The SE technique offers high entrapment efficiencies for lipophilic drugs but very low for hydrophilic. On the other hand, and polydispered particles are obtained (131).

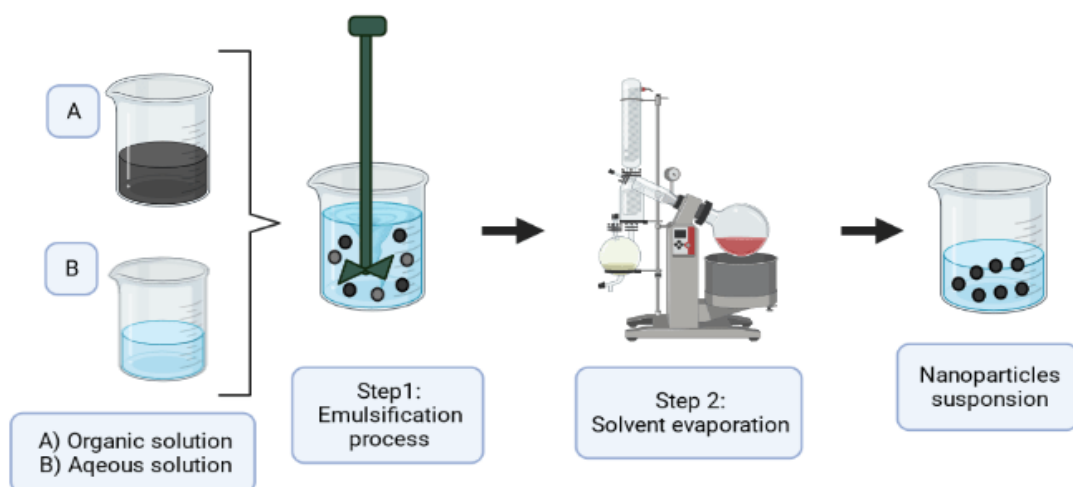


Figure 17. Representation of the Polymeric NPs preparation through single emulsion-solvent evaporation technique.

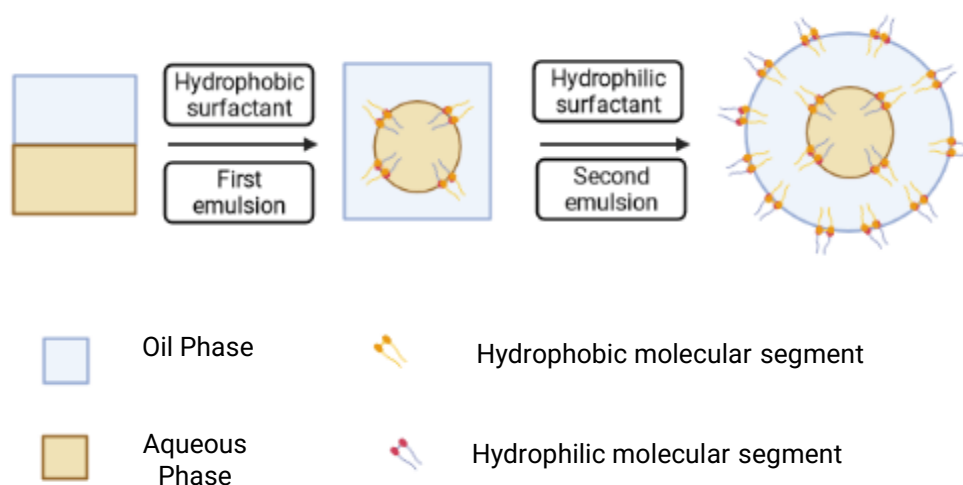


Figure 18. Representation of the two-step processes to produce DE.

1.4.1.2 Salting out

In this technique, polymer and drug are dispersed inside a water-soluble in the presence of a stabilizer and high concentrations of salting-out agent (Figure 19) such as $MgCl_2$, $CaCl_2$ can be used as the salting out agent This is followed by emulsification of the polymer inside an aqueous gel to form an oil-in-water emulsion at elevated

mechanical stirring. The emulsion is further diluted with water to enhance solvent diffusion into the aqueous phase and hardened of the polymers. Finally, the solvent is removed using reduced pressure and ultracentrifugation (132,133). Salting out technique is helpful in obtaining a high yield, large drug encapsulation, small particle size, and possibility to scaling up (132,134,135).

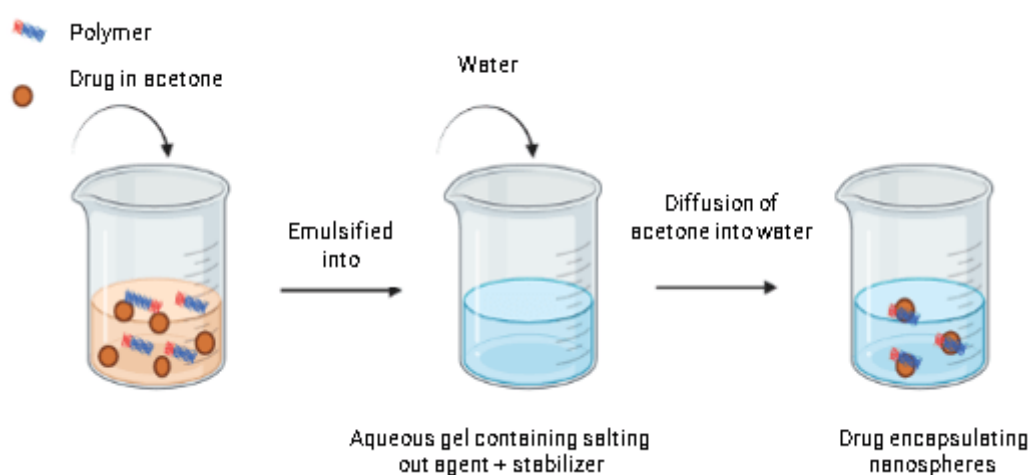


Figure 19. Illustration of salting out procedure for preparing polymeric NPs.

1.4.1.3 Emulsification-diffusion

Emulsification-diffusion technique involves the development of an o/w emulsion between a partially water-miscible solvent that contains drug and polymer, and an aqueous phase that contains a surfactant (Figure 20) (136,137). In the internal phase, the emulsion comprises a moderately hydro-miscible organic solvent that is saturated using water to guarantee a thermodynamic balance between both phases (136). Successive dilution forces the solvent to diffuse from the dispersed droplets towards the external phase whilst the particles start to form. The organic solvent is eliminated through evaporation or filtration based on its boiling point. This technique is simple, cost-effective, and has low energy consumption (138) with high entrapment efficiency. Furthermore, no special processing equipment or advanced production

plants are required for this technique. On the other hand, large water volume should be removed from the suspension when the dilution is achieved. In addition, it needs more steps for processing and longer processing time.

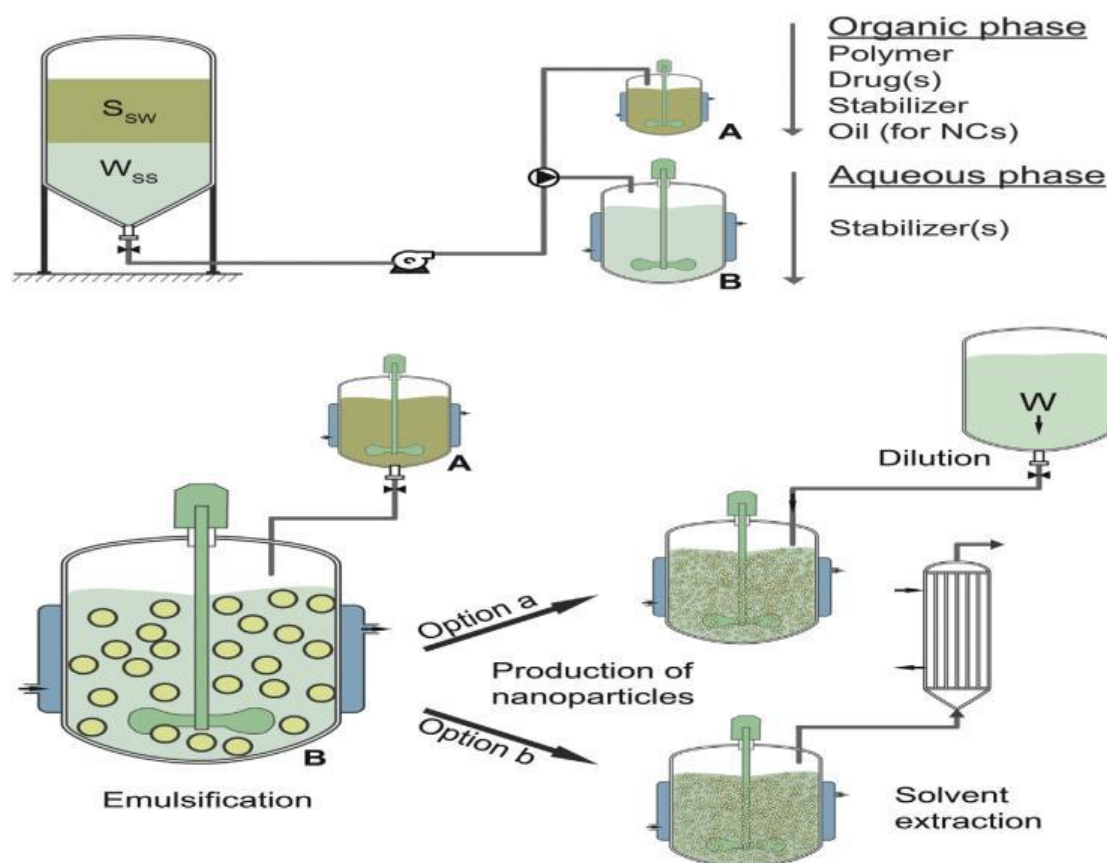


Figure 20. Different stages enrolled in the Emulsification-diffusion technique, adapted from (138).

1.4.1.4 Nanoprecipitation

Firstly, the polymer is dispersed inside a water-miscible solvent with intermediate polarity. The obtained solution is added dropwise to an aqueous solution under continuous stirring. At this stage, the nanoparticles start to form as the polymer solution diffuse spontaneously inside the aqueous phase and precipitate as nanocapsules or nanospheres. In general, surfactants could be used during the reaction in order to ensure that the colloidal suspension is stable. Moreover, the prepared

nanoparticles have a well-defined size and a narrow polydispersity index. Furthermore, nanoprecipitation technique is usually used for preparing polymeric NPs with approximately 170 nm dimensions (139), due to its easy manipulation (140).

1.4.1.5 Spray-drying

In spray-drying (Figure 21), the drug-containing fluid is forced through a nozzle as mist which is dried to generate a fine powdered product (141,142). Spray-drying is a single-step technique and useful for drugs that are heat-sensitive including therapeutic drug (143). On the other hand, the use of hot dry air could cause thermal stress to the used drug. Furthermore, the dehydration process might modify the structure and affect the particle stability.

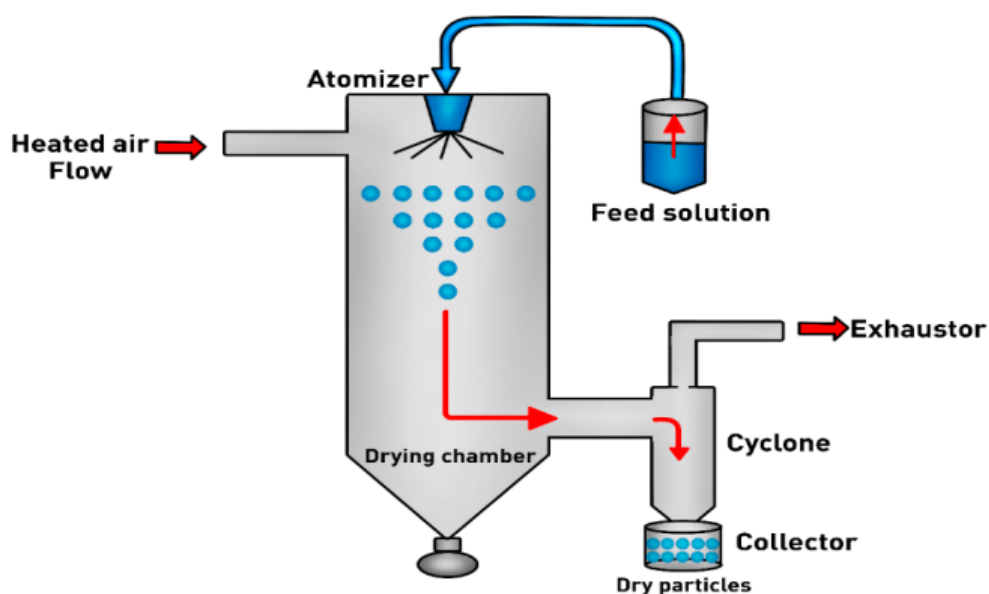


Figure 21. Illustration of the spray-drying process for polymeric NPs production, adapted from (143).

1.4.1.6 Supercritical fluid technology

In supercritical fluid (SCF) technique polymeric NPs are, precipitated from supercritical solutions of the polymer dissolved in a supercritical fluid, followed by rapid expansion of the solution to the air (144). SCF technique is a green technology because the used supercritical fluids are environmental in nature (145). On the other

hand, high pressure, elevated maintenance costs, and the auxiliary equipment are required for SCF technique, which has limited its use in the pharmaceutical field.

1.4.1.7 Iontropic gelation method

This technique (Figure 22) is based on electrostatic interactions between oppositely charged groups from the polymer and a cross-linker (131,146). Polymers such as, alginate, dextran, carrageenan, and chitosan have been widely used as gelation polymers in the formulation of nanoparticles (147). Controlled drug release can be obtained from a matrix –dispersed API .

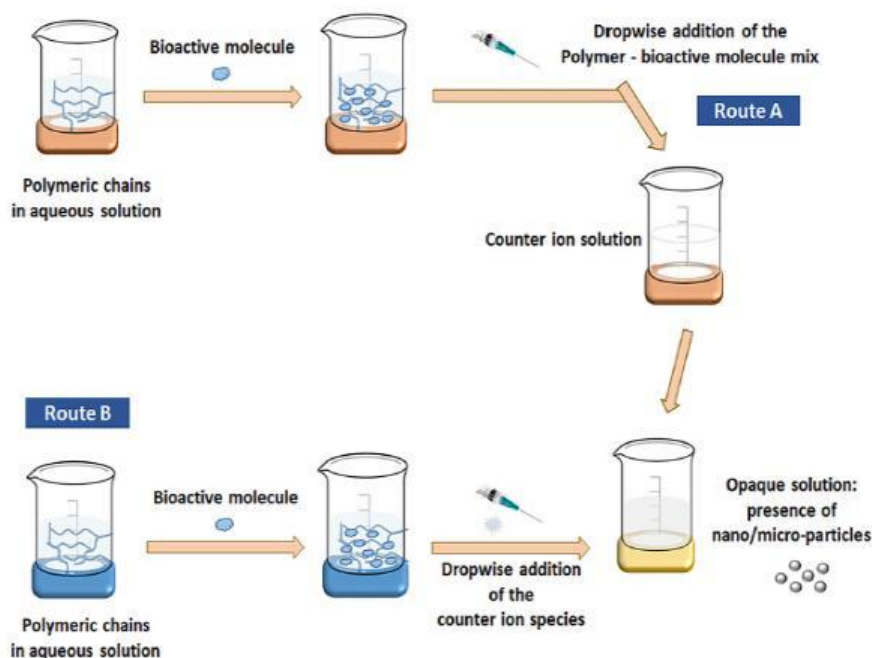


Figure 22. Polymeric NPs synthesis using the ionotropic gelation method, adapted from (148).

1.4.2 Physical techniques for NPs characterization

To physically characterize the formulated polymeric NPs, there are several analytical techniques used to assess size distribution surface charge. The dynamic light scattering (DLS) is used for size analysis whilst morphology is assessed using scanning electron microscopy (SEM) or atomic force microscopy (AFM). The physical status of the drug within the carrier systems is done using thermogravimetric analysis (TGA) and Energy X-ray diffraction (XRD). Ascertaining of chemical structure can

be carried out on the Fourier transform infrared spectroscopy (FT-IR), Nuclear Magnetic Resonance (NMR), and Energy Dispersive X-Ray Analysis (EDX). These instruments were used in the characterization of the CUR-NPs. CUR analysis was carried out using the high-performance liquid chromatography. In the following sections, some of these techniques would be briefly described.

1.4.2.1 Fourier transform infrared spectroscopy

FT-IR spectroscopy is a powerful technique used to determine the functional groups through IR beam irradiation on sample and assessing absorption bands coming out of the sample (Figure 23) (148,149). Fundamentally, the IR spectrum acquired from FTIR spectrometer lies between 4000 and 666 cm^{-1} (150). The main advantage from FTIR technique is that based on the unique characteristic absorption/emission in the IR spectral region of the sample, the collected data could be analyzed both quantitatively and qualitatively (151).

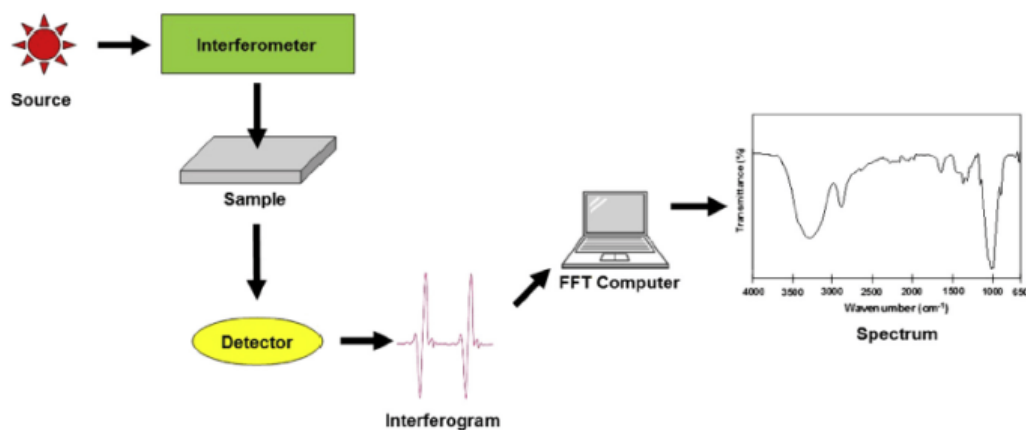


Figure 23. Basic components in the FT-IR spectrometer, adapted from (149).

1.4.2.2 Nuclear Magnetic Resonance

Nuclear Magnetic Resonance (NMR) is one of the most powerful techniques used to elucidate the structure of chemical compounds (152). The basic principle of NMR is that all nuclei are electrically charged and have spin. Thus, once an external

magnetic field would be applied, a transfer in energy occurs from the base energy level towards a higher energy level. The energy transfer has a corresponding wavelength, and once the spin returns to its base level, the energy will be emitted at the same corresponding frequency. The signal matching the difference in energy is measured and processed to obtain an NMR spectrum for the analyzed sample (Figure 24) (153–155).

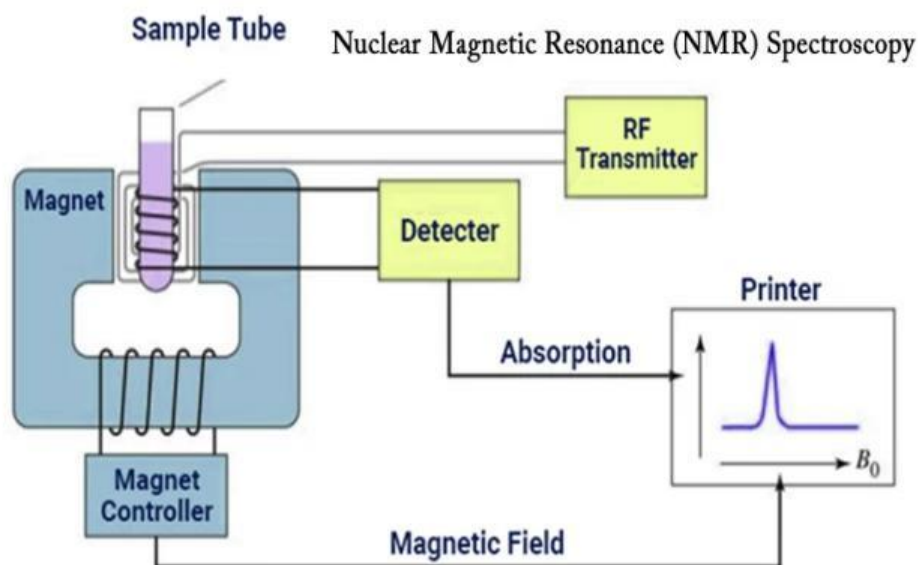


Figure 24. Basic principle of NMR.

1.4.2.3 Atomic Force Microscopy

AFM (Figure 25), also named scanning force microscope (SFM), used to obtain high-resolution images involving surface height information and three-dimensional information about the sample morphology. A cantilever is used to scanning the surface of the specimen (156). Forces between the tip and the sample deflect the cantilever according to Hooke's law (157), creating a imagery of the sample. AFM is versatile because measurements can be taking in fluids as opposed to vacuum thus sample remain in their native state (158).

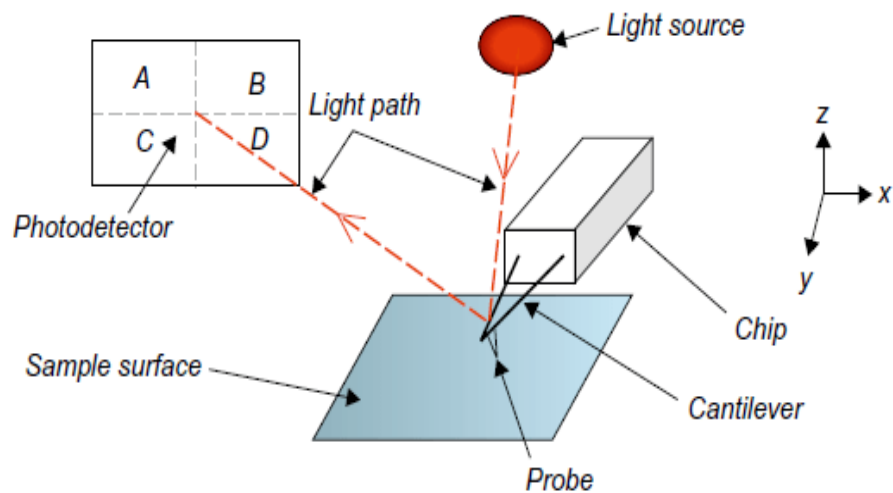


Figure 25. Illustration of AFM set-up, adapted from (159).

1.4.2.4 Dynamic light scattering

In Dynamic light scattering (DLS), the Brownian motion of macromolecules inside a medium directed with beam of light is assessed whereby, smaller particles are moving at greater speeds than larger particles (Figure 26). when other parameters that could affect the particle movement are known, the hydrodynamic diameter could be calculated through measurement of the particles speed. The relation between the particles speed and the particle size is provided by the Stokes-Einstein equation:

$$R=KT/ 6\pi\eta D$$

R: Hydrodynamic diameter. K:Boltzmann constant. T: Absolute temperature.
 η :Viscosity of the solution. D:Diffusion coefficient.

This relationship demonstrates how size is obtained from diffusion speed, when the temperature and phase viscosity of the sample are identified. DLS technique offers several advantages including the ability to run experiments with broad range of sample solvents and temperature. Furthermore, DLS is a non-invasive technique with low amounts of sample are required (159).

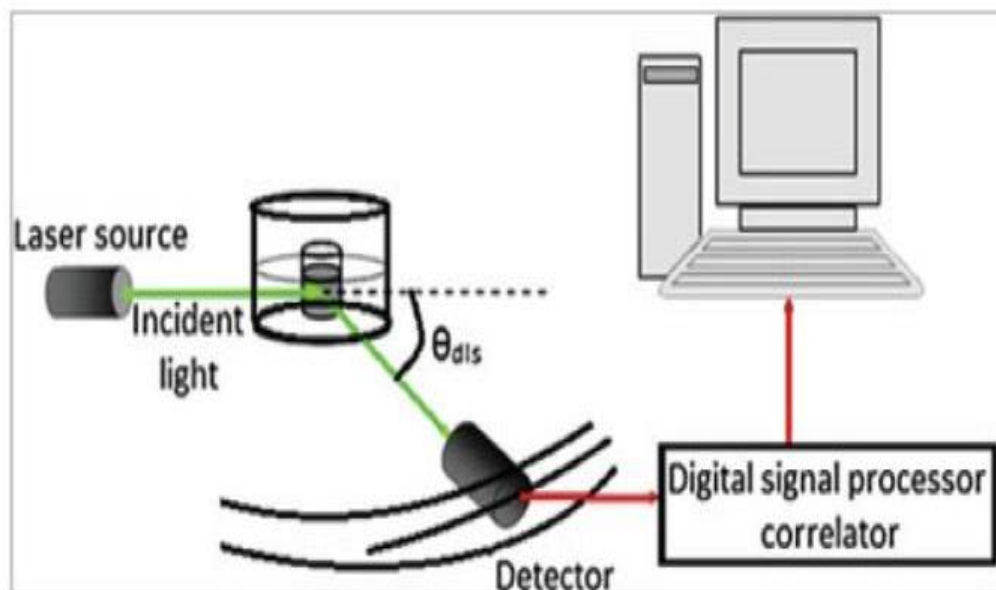


Figure 26. Illustration of DLS instrumentation, adapted from (160).

1.4.2.6 X-ray diffraction

X-ray diffraction (XRD) is a powerful and nondestructive technique used to characterize materials and to provide information on the structure, phase, and crystallinity (160). XRD depends on constructive interference that occurs between monochromatic X-rays and a tested sample (Figure 27). The interfered X-rays are mainly produced by a cathode ray tube, then filtered to obtain a monochromatic radiation that is further collimated and directed to the sample (160). In XRD, problems related to peak overlap are minimized and a precise quantitative analysis could be obtained (161). Further, XRD is a powerful and rapid used to identify unknown samples. Furthermore, it needs minimal sample preparation (160). XRD has been applied as a key technique used for drug analysis as it plays a vital role in all stages of drug developing process, its testing and production (162).

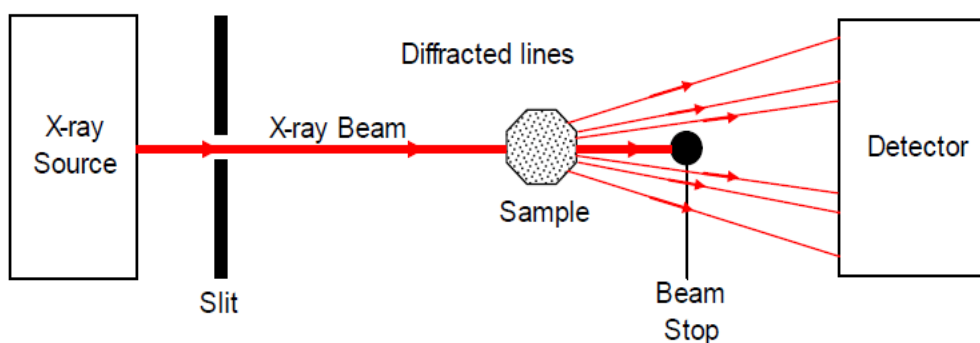


Figure 27. Illustration of X-ray diffraction instrumentation, adapted from (164).

1.4.2.7 Thermogravimetric analysis

Thermogravimetric analysis (TGA) is a unique technique used for studying the thermal decomposition of samples (Figure 28) (163). In TGA, the main principle is that changes in the sample mass is studied as an outcome of the thermal treatment under programmed conditions. Consequently, TGA is principally used to understand particular thermal events including absorption, desorption, adsorption, sublimation, vaporization, decomposition, reduction, and oxidation (164). Furthermore, TGA could be applied in evaluating products lost during chemical reactions including nanomaterials, polymers, and polymer nanocomposites (164,165).

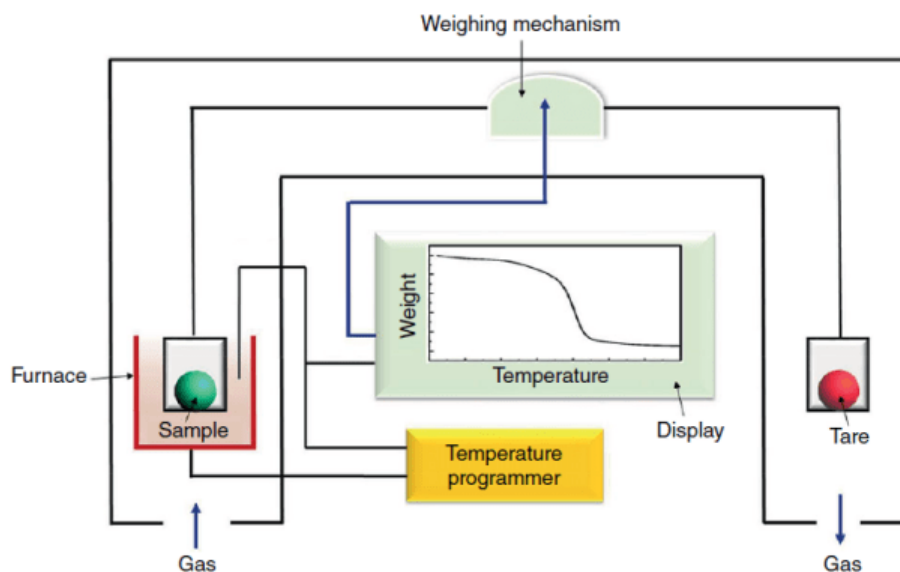


Figure 28. Schematic illustration of TGA instrument, adapted from (167).

1.5 D-Mannose

D-mannose (Figure 29) is a monosaccharide and an epimer of D-glucose at the position of C-2, and an aldose isomer of D-fructose (166). D-Mannose is isolated primarily from larch rod, fruits, herbs, and palm (166,167). It is quickly absorbed by the body, with no side effects from long-term use (167). D-mannose has been linked to chemotherapeutic effectiveness (168), whereby For instance, a previous study showed that after treating tumor cells with mannose, the rate of cell growth has decreased (169). This is because mannose accumulates inside the cancer cells in the form of mannose-6-phosphate, which suppresses hexokinases and phosphoglucose isomerase enzymes involved in glycolysis (169,170). Other sugars were tested for their anticancer effects including galactose, fructose, and glucose whereby mannose hindered more effectively tumor cell growth than other types of tested sugars (169). In another study, mannose demonstrated a potential antitumor activity on lung cancer cell lines by inhibiting cell proliferation, inducing G0/G1 cell cycle arrest, and decrease of the invasive abilities of cancer cells (171). Thus, mannose-targeted systems could help

is overcoming the weak specificity and dose-limiting toxicity of anti-cancer vehicles as it originates from natural sources.

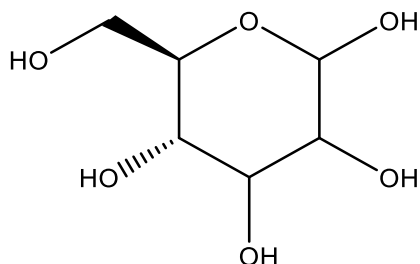
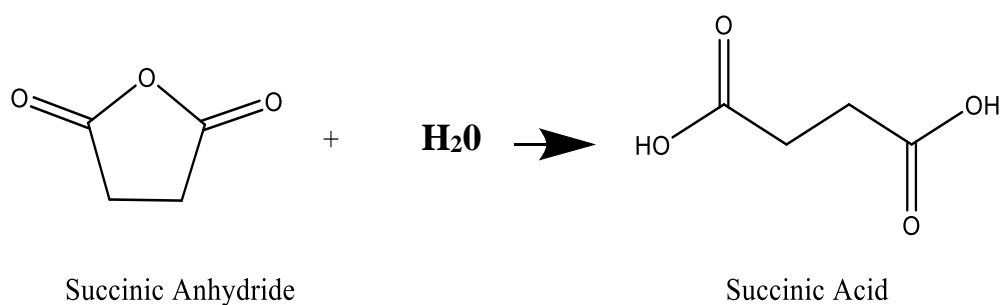


Figure 29. Chemical structure of D-mannose.

1.6 Succinic anhydride

Succinic anhydride is an organic compound that has the molecular formula $(\text{CH}_2\text{CO})_2\text{O}$ and undergoes hydrolysis to succinic acid as follows:



Succinic acid is a diprotic acid present in the undissociated form at pH 3.50 (172). The carbonyl groups in succinic acids undergoes protonation at acidic pH (1.2), and it is ionized under basic pH (7.4) (173). Due to the aforementioned properties of succinic acid, we perceived that conjugation with CUR might improve its physicochemical and biological properties. Furthermore, succinylation reaction has been successfully achieved for various drugs as methylprednisolone (174), metronidazole (175), primaquine (176), and CUR (94). In a previous study, CUR Diethyl Disuccinate (CURDD), an ester prodrug of CUR was investigated in liver

hepatocellular carcinoma (HepG2) Xenograft Mice (177). From the study, CURDD decreased tumor growth better compared to the pure CUR with improved anti-cancer activity of CUR. In another study, a series of succinyl derivatives of CUR were prepared as potential prodrugs for CRC treatment (94), where, an increased in curcumin release was observed in human plasma, which suggested that CUR succinylation is a useful prodrug strategy. Furthermore, these prodrugs inhibited cell growth better than pure CUR (104).

1.7 Study rationale and objectives

Through the literature, there is still a lack of potent anti-cancer CUR conjugates with improved solubility and stability properties although diverse conjugates and derivatives were previously synthesized. It was proven that CUR succinylation using succinic anhydride has improved CUR limitations and anticancer properties against CRC (94). Moreover, mannose receptor (MR), which is a stable marker, has overexpression in many cancers because tumor cells have high affinity to carbohydrate molecules more than normal cells to rapidly proliferate (178). Thus, mannose mediated-NPs having multiple mannose residues are anticipated to deliver stronger binding with MR in cancer cells and to enhance their uptake by cancer cells that overexpress MR (170). In a previous study, it was found that MR is highly expressed in CRC cells such as HCT-116 cells (179). Furthermore, mannosylated-CS-NPs have clearly suppressed tumor growth through in vivo assays (180). Thus, drug encapsulation inside mannosylated-CS delivery systems would enhance the anticancer activity and reduces the drug's cytotoxicity as a natural drug carrier. However, CUR encapsulation in mannosylated-CS NPs targeting CRC has not been studied before. Thus, the objectives of this research are summarized as follows:

- 1- To encapsulate CUR and succinylated CUR in mannosylated-CS NPs carriers

- 2- To evaluate the physical and chemical characteristics of the prepared nanoparticles.
- 3- To test the anti-CRC properties of the nanoparticles using *in vitro* assays targeting cytotoxicity assays, apoptotic assays, and cell cycle evaluations.

This thesis includes five chapters that will illustrate the research directed to achieving the above objectives. Chapter 2 includes the developed protocols of the formulated CM-NPs containing CUR and CUR.SA. Chapter 3 consists of the characterization and *in vitro* evaluation of the formulated nanoparticles. Chapter 4 contains the obtained findings compared to the literature. Chapter 6 includes a summary of the fundamental findings of this work and illustrates the future prospective of the research.

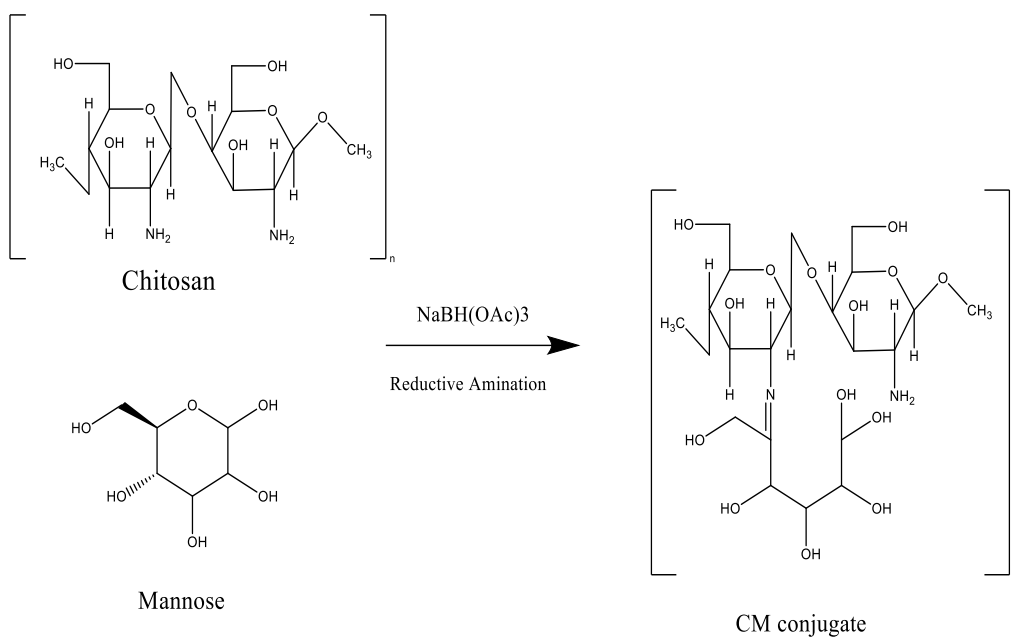
CHAPTER 2: MATERIALS AND METHODS

2.1 Materials

Curcumin (mixture of Curcumin, demethoxycurcumin, and bisdemethoxycurcumin, 98%) and Chitosan (MW: 100.000-300.000) were purchased from Acros Organics. D-Mannose, 4-(Dimethylamino) Pyridine ($\geq 98\%$), Ethanol ($\geq 99.8\%$), Methanol ($>99.9\%$, HPLC gradient), acetonitrile ($>99.9\%$, HPLC gradient) and Acetic acid were purchased from Honeywell Fluka. Succinic Anhydride ($\geq 99\%$), Dimethyl sulfoxide ($\geq 99.9\%$), Sodium triacetoxyborohydride and chloroform were purchased from Sigma Aldrich. Sodium tripolyphosphate (Granular) was purchased from Alfa Aesar. Diethyl ether ($\geq 98\%$) and Ethyl acetate $\geq 99.5\%$ were purchased from VWR. Other organic chemical and solvents used were of reagent grade and used as directed.

2.2 Synthesis of chitosan-mannose conjugate

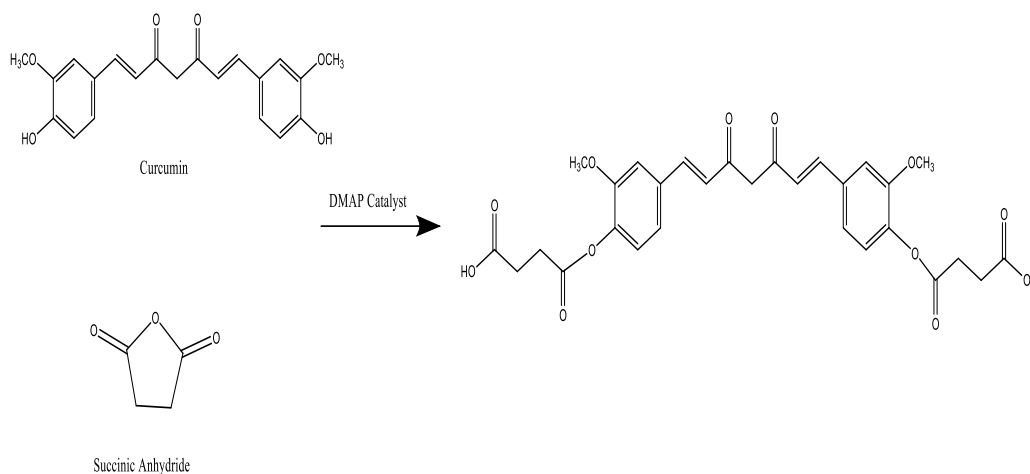
Chitosan-mannose conjugate (CM) was synthesized as described in the literature (181–183) with some modifications. Mannose conjugation to CS was conducted via reductive amination of CS with D-mannose (Scheme 1) in the presence of sodium triacetoxyborohydride ($\text{NaBH}(\text{OAc})_3$). Briefly, chitosan (169 mg) was dissolved in 1% acetic acid and pH adjusted to 5.5 with 2 M NaOH. D-mannose (17 mg) and sodium triacetoxyborohydride were then added. The obtained solution was stirred at 210 rpm at room temperature for 48 hours. CM was precipitated out of the mixture at basic pH using 2 M NaOH, followed by centrifugation at 4000 rpm for 10 mins. Finally, the sample was dried in the oven at 40°C overnight. The chemical structure of CM conjugate was elucidated using FT-IR spectrophotometer and NMR (^1H and ^{13}C).



Scheme 1. CM conjugate synthesis pathway.

2.3 Curcumin-Succinic anhydride Conjugate synthesis

CUR-succinic anhydride (CUR-SA) conjugate was synthesized according to scheme 2. Briefly, CUR and SA were dissolved completely in chloroform followed by the addition of dimethyl amino pyridine (DMAP) as a catalyst. The solution was stirred at 400 rpm at 25°C followed by vacuum refluxing while stirring at 20°C. Excess solvent was removed via rotary evaporation at 70°C while stirring at 60 rpm. The retrieved sample was washed with diethyl ether, filtered using vacuum filtration and then dissolved in ethanol and left to dry overnight at 25°C. Thin layer chromatographic (TLC) analysis was performed on silica gel G F254 (Merck Aluminum plate) with ethyl acetate: ethanol (2:3) as a mobile phase to assure the occurrence of conjugation reaction. The structure of CUR-SA conjugate was elucidated using FT-IR, ^1H and ^{13}C NMR spectroscopy.



Scheme 2. CUR.SA conjugate synthesis pathway.

2.4 CUR.SA -loaded CM-STPP nanoparticles synthesis

CUR.SA-loaded CM nanoparticles were prepared using ionotropic gelation method (Figure 30) as described by Jahromi et al. before with slight modifications (184). Firstly, 1 mg/mL stock solution of CM was prepared in 2% (V/V) acetic acid solution. Similarly, a 1mg/ml sodium tripolyphosphate (STPP) solution was prepared in ultra-pure H₂O. Secondly, 1 mL of CM solution was ultra-sonicated until totally dissolved and volume adjusted to 1.5 mL with DW. Thirdly, 1 mg/mL stock solution of CUR.SA was prepared by dissolving the conjugate in 99.8% ethanol followed by the addition of 1 ml to the CM solution. Subsequently, a 100 μ L aliquot of the STPP solution was added dropwise as a cross linker to the CUR.SA-CM. The obtained mixture was further stirred at 700 rpm for 30 mins, followed by centrifugation at 4000 g for 15 mins. Finally, the supernatant was transferred to Eppendorf[®] microcentrifuge tubes for consequent analysis. Blank CM-NPs and CUR-NPs were similarly formulated. Various formulations were made by varying the compositions of the components as presented in Table 3.

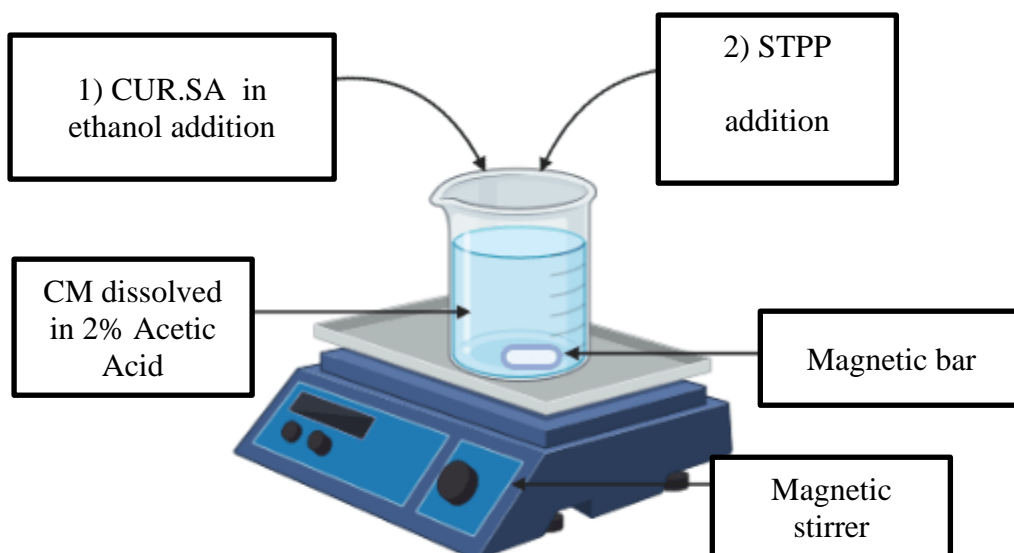


Figure 30. Method for CUR.SA-NPs production using ionic gelation under constant magnetic stirring.

Table 3. Optimization process of the prepared nanoparticles.

Formulation	Chitosan (1mg/mL)	Curcumin (1mg/mL)	STPP (1mg/mL)
A	1mL	1mL	200 μ L
B	1mL	1mL	100 μ L
C	1mL	1mL	300 μ L
D	0.5mL	1mL	100 μ L
E	1.5mL	1mL	100 μ L

2.5 Stability test of CUR and CUR.SA

A methanolic stock solution of CUR and CUR.SA conjugate was prepared at 250 μ g/mL and exposed to three different conditions, in dark, at room temperature, and sunlight, each for 0.5, 1, 2, 4, and 6 hours to assess the degradation profiles of CUR and CUR.SA as a function of time. A reversed-phase HPLC with UV-VIS detection at 425 nm was used to detect both CUR and CUR.SA. A 100 μ L aliquot was aspirated from

each vial and analyzed using HPLC system as described in section 2.7.6.

2.6 Solubility of CUR and CUR.SA conjugate test

The solubility of CUR and CUR.SA conjugate as a function of different media was evaluated according to previous protocols with slight modifications (185). Briefly, an excess amount of CUR or CUR.SA conjugate was dispersed in ultra-pure water and stirred at 300 rpm for 24 hours at ambient room temperature until saturated equilibrium was attained. 1 mL aliquot of the saturated solution was filtered and diluted to a 1:1 ratio with methanol and analyzed using HPLC method as described in section 2.7.6. For CUR and CUR.SA solubility study in ethanol, the same procedure was followed.

2.7 Characterization of the nanoparticles

2.7.1 FT-IR Analysis of samples

FT-IR analysis of CUR, CS, mannose, SA, CUR.SA conjugate, CM conjugate, STPP, CM-NPs, CUR-NPs, and CUR.SA-NPs were achieved using Spotlight 400 FTIR Spectrophotometer (Perkin Elmer, USA). Data were collected between 4000cm^{-1} - 400cm^{-1} .

2.7.2 NMR spectroscopic analysis

^1H and ^{13}C NMR spectroscopic analyses of CUR, CS, mannose, SA, CM and CUR.SA conjugates were conducted on a JNM-ECZR (600 MHz) FT Spectrometer (JEOL, USA). The chemical shifts were collected in parts per million (ppm) relative to the solvent peak and the coupling constant (J) was recorded in Hertz (Hz).

2.7.3 Zeta size and potential

Particle size and zeta potential analyses were conducted on a Zeta sizer Nano ZS (Malvern Instruments, UK) in order to assess the colloidal stability of nanoparticles. Polydispersity index (PDI) was also measured using the Zeta-sizer to assess homogeneity within the samples. All data is presented as mean \pm SD (n=3).

2.7.4 Atomic force microscopy

AFM analysis was used to investigate the surface morphology and size distribution of the prepared nanoparticles. A few drops from the previously collected supernatants were deposited on freshly cleaved MICA sheets and air-dried, then mounted on the platform of the AFM (MFP3D, Asylum Research UK) operated in scanning and nano indentation mode. The mica deposited samples were fixed on a glass coverslip with a double-sided adhesive that was oriented for access by the cantilever at a force constant of 0.7 N.m^{-1} , resonance frequency of 150 kHz and scan area of $5 \times 5 \mu\text{m}$.

2.7.5 X-Ray Diffraction (XRD) Analysis

XRD analysis was conducted to study the crystallographic structure of the raw ingredients and prepared nanoparticles to assess any changes in phase. The diffractograms of CS, mannose, CM conjugate, CUR, SA, CUR.SA conjugate, CM-NPs, CUR-NPs, and CUR.SA-NPs were obtained using an X-ray diffractometer (PANalytical, Netherlands) operated at 45 kV and 40 mA with scan angles from 5° to 75° with a scanning speed of $0.02^\circ/\text{step}$ and the used step time was 0.5 s.

2.7.6 HPLC assay for CUR quantification

An HPLC system (series 1260 quaternary pump, Agilent, USA) equipped with a UV/Vis detector (G1315C, Agilent, USA) set at 425 nm was used for the analysis. The stationary phase comprised of a reverse phase column (XBridge UPLC Waters, 150 mm x 3 mm, $2.5 \mu\text{m}$, USA) and the mobile phase; methanol: 0.01% acetic acid: acetonitrile (5: 43: 52 %). The mobile phase was filtered using $0.45 \mu\text{m}$ regenerated cellulose membrane filter paper (WHATMAN, UK) prior to analysis which was run at a flow rate of 0.3 ml/min with injection volume of $5 \mu\text{l}$. Standard solutions of CUR were prepared in methanol (0.005-0.03 mg /mL) and injected on the HPLC system to obtain peak areas, which were used to build a standard calibration curve (Figure 31).

2.7.7 Evaluation of encapsulation parameters

To estimate the percentage encapsulation efficiency (%EE) of drug loaded within the nanoparticles, the obtained supernatant from the centrifuged CUR-NPs and CUR.SA-NPs formulations were assayed for absorbance spectra at 425nm using the HPLC system. The calibration curve was used to determine the free CUR concentration and the following equations were used for calculating the % EE (Equation 1) and drug loading content (Equation 2).

$$\% EE = \frac{\text{initial amount of CUR or CUR.SA} - \text{free CUR or CUR.SA}}{\text{initial amount of CUR or CUR.SA}} \times 100\% \quad (1)$$

$$\% DL = \frac{\text{Weight of drug in the Nanoparticles}}{\text{Weight of the Nanoparticles}} \times 100\% \quad (2)$$

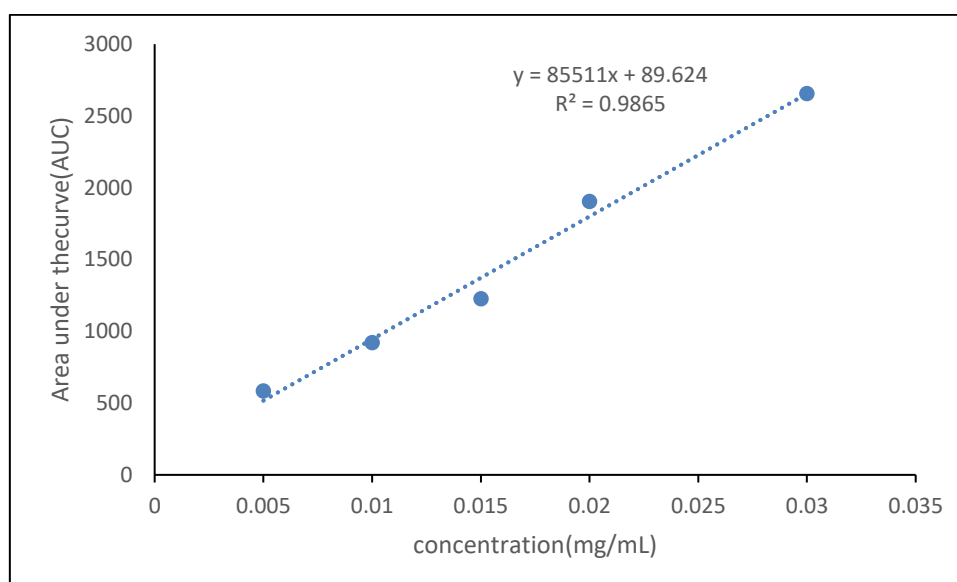


Figure 31. Calibration curve of CUR through serial dilution of the respective standard CUR solution in methanol

2.8 Drug release from prepared NPs

Drug release from the NP was performed based on a modified procedure from (186–188). In brief, the NPs suspension was placed inside Phosphate Buffer Saline (PBS) as a releasing media with pH 6.8 to simulate the colonic region pH of the gastrointestinal tract and in pH 1.2 to simulate the stomach pH at a ratio of 2:1 (v/v). The suspension in each case was divided into 10 Eppendorf[®] tubes of 500 µl each. The

Eppendorf® tubes were maintained at 37°C under 150 rpm shaking. At predetermined time intervals of 0 (initial), 1, 4, 6, 24, 48, and 72 hours, one Eppendorf tube was withdrawn and centrifuged at 14,000 rpm for 7 min to separate the released CUR from the NPs (pellet form). The released CUR was redissolved in 0.5 ml ethanol, filtered, and then used to quantify the amount of CUR using the HPLC method described in section 2.7.6. The reported data is expressed as the mean of three independent runs. The percentage of CUR released was estimated by

$$\% \text{ Amount of CUR released} = \frac{\text{Amount of CUR or CUR.SA released}}{\text{Total CUR or CUR.SA in NP}} \times 100\%$$

2.9 Morphological and elemental analyses of NP by Scanning Electron Microscopy (SEM) and Energy dispersive X-ray (EDX)

The morphology of the formulated nanoparticles was examined on a Nova Nano (SEM) (Model Nova Nano SEM 450, ThermoFisher Company, USA). The SEM was equipped with an EDX detector. A few drops of the nanoparticles were deposited on the stub of the SEM and left to air drying at ambient temperature. The dried samples were placed in the vacuum chamber of the SEM and operated at 5kv. Images of the nanoparticles were recorded and stored for further analyses. EDX analysis was conducted on the nanoparticles in order to study the elemental composition of CS, STPP, CM-NPs, CUR-NPs and CUR.SA-NPs. A small amount of sample was placed on a carbon tape and made to air dry, to be further placed in the SEM for identification of the elemental composition.

2.10 Thermogravimetric analysis (TGA)

Thermogravimetric analyzer (TGA 4000, PerkinElmer, USA) was used to analyze the thermal stability of CM-NPs, CUR-NPs and CUR.SA-NPs as a function of heat. The samples were heated from 25 to 500 °C at a rate of 10 °C /min under a gentle stream (30 mL/min) of nitrogen.

2.11 Stability test of nanoparticles

2.11.1 Structural assessment

The stability of formulated CM-NPs, CUR-NPs, and CUR.SA-NPs was assessed in 1 X Gibco® DMEM (Thermo Fisher Scientific, USA), and 1X Gibco® RPMI media (Thermo Fisher Scientific, USA), both supplemented with 10% Gibco® fetal bovine serum (Thermo Fisher Scientific, USA) and 1% PenStrep antibiotic (Thermo Fisher Scientific, USA), and 1% Gibco® GlutaMAX (Thermo Fisher Scientific, USA) to assess the impact of these media on the structural integrity (94). Changes in the hydrodynamic diameter of the nanoparticles in DMEM with 10% FBS and RPMI with 10% FBS over 48 hours were assessed after placing drops of the nanoparticles on MICA sheet to air-dry and then analyzing using AFM. Structural changes were ascertained by comparing the images obtained with those of untreated samples.

2.11.2 Effect on storage conditions

The physical stability of CUR-NPs, and CUR.SA-NPs as a function of duration of storage at 3 and 37°C was determined at 0, 1, 7, 14 and 28 days by analyzing changes in hydrodynamic diameter, PDI, and zeta potential of the nanoparticles (189).

2.12 *In vitro* cell evaluation of formulations

2.12.1 Maintenance of cell culture media

Human colorectal adenocarcinoma cell lines (HCT116 and SW480) were cultivated in RPMI and DMEM medium, respectively, supplemented with 10 % FBS and 1 % penicillin-streptomycin. Both cell types were incubated at 37 °C in an incubator supplied with 5 % CO₂ until % confluency of 70-80% was reached. The cells were viewed daily under optical light microscope at 10× magnification (Nikon Eclipse TS100, Japan) to check the health state of the cells.

2.12.2 Subculturing of cells

Subculturing of the cells was conducted in a T-75 filtered tissue culture flask (Thermo Fisher Scientific, USA) after confluency, at which point, the medium was discarded, and the flask was washed with PBS. The cells were detached from the flask using trypsin–EDTA, followed by incubation for 3 mins at 37 °C to allow the complete detachment of cells. The flask was tapped gently to detach the cells, which were viewed under the optical light microscope to confirm their detachment. Once detachment was confirmed, the culturing medium was used to wash the flask, and centrifuged at 1300 rpm for 5 min, followed by re-suspension of the pellet in the corresponding medium. Finally, dilution with trypan blue (Sigma–Aldrich, USA) was carried out followed by counting the required number of cells using an automated cell counter (TC20, BIO-RAD, USA). The cells were introduced into different flasks for further subculturing.

2.12.3 Cell counting

After resuspension of the pellet in the growing medium as described in section 2.12.2, 10 µL of the cells were mixed with 10 µL of trypan blue and added to the counting chamber of an automated cell counter. The automated cell counter displays the total number of viable cells per 1 mL of solution. The total number of cells was calculated as follows:

Total number of cells per 1 mL(given by the automated counter) x total volume of corresponding medium (mL).

2.12.4 Cell cytotoxicity

The cytotoxicity of due to CUR-NPs and CUR.SA-NPs was assessed using a cell counting Kit-8 (CCK8) assay. SW480 and HCT116 cell lines were chosen as they comprise the major mutations of colon cancer. Furthermore, both cell lines are among the most aggressive and manifesting types among other CRC cell lines. The SW480 and HCT116 cell lines were cultured for 24 hours inside 96 well plates (Thermo Fisher

Scientific, USA) at 5000 cells/well and incubated at 37 °C inside a CO₂ incubator. After 24 hours, the cells were treated with free CUR, CUR.SA conjugate, CUR-NPs and CUR.SA-NPs at different concentrations (1, 10, and 25 μM) for a period of 24 and 48 hours. Cells in medium alone, DMSO and CM-NPs (50 μM) act as controls. After each time point, the cell viability was determined through CCK-8 assay using WST-8 reagent (Cat. No:5015944001, Sigma- Aldrich, USA) as provided by the manufacturer's protocol: in each well, 20μl of the reagent was added and incubated at 37 °C for 1 hour, and the quantification of the formazan dye produced by metabolically active cells was analyzed by a spectrophotometer (Teccan, Switzerland). Generally, the amount of the formazan dye that is generated due to the activity of dehydrogenases inside the cells is directly proportional to the number of viable cells. The absorbance was measured at 450 nm and the percentage of cell viability was calculated.

2.12.5 Cell Cycle analysis

Cell cycle analysis was used to evaluate the cellular distribution in the different phases of cell cycle. SW480 and HCT116 cells were seeded in T-75 flasks for 24 hours to allow cell adherence. Further, cells were treated with 10 and 25 μM of CUR-NPs and CUR.SA-NPs. Untreated cells were used as a control. After treatment for 24 hours, cells were trypsinized and centrifuged at 1300 rpm for 5 minutes. Further, 1×10^6 cells were collected, centrifuged at 300g for 5 minutes, and resuspended in 300 μl PBS. Lastly, 700μl of 100% ethanol was added drop by drop while vortexing for cell fixation, and the cell suspension was kept overnight at 4°C. The next day, cells were washed and centrifuged at 500g for 5 minutes, resuspended in 250 μl propidium iodide (PI)/RNase staining solution (Cat. No. 550825), incubated at room temperature for 15 minutes, centrifuged at 500g for 5 minutes, and the pellet was resuspended in 250 μl PBS. Finally, stained cells were investigated for DNA content using flow cytometry (Flow

FACS BD Bioscience, USA).

2.12.6 Cellular apoptosis analysis

Cell apoptosis assay was used to assess the percentage of cells that are undergoing apoptosis. HCT116 and SW480 cells were seeded in T-75 flasks. After 24 hours, cells were treated with 10 and 25 μM of both CUR-NPs and CUR.SA-NPs. Untreated cells were considered the control. After 24 hours, cells were trypsinized, centrifuged at 1300 rpm for 5 minutes, and 5×10^5 cells were collected, the cells pellet was suspended with 94 μl with Annexin Binding Buffer (Cat. No. 556454), 5 μl Annexin and 1 μl PI. Further, cells were incubated for 30 minutes in the dark at 25 $^{\circ}\text{C}$, washed with 250 μl PBS, and lastly analyzed using flow cytometry (Flow FACS BD Bioscience, USA).

2.12.7 Western Blotting

Cells were seeded using T75 flask, and treatment was carried out at concentrations of CUR- NPs (10 and 25 μM) and CUR.SA-NPs (10 and 25 μM) for both cell lines. After treatment incubation for 24 hours, proteins were collected and quantified using Rapid Gold BCA Protein assay kit (Thermo Scientific, USA). A 50 mg of total proteins were separated using sodium-dodecyl sulfate polyacrylamide gel electrophoresis, transferred to polyvinylidene difluoride (PVDF) membrane to be probed after blocking using the following primary antibodies against total PARP (1:1000, 9542S, Cell Signaling Technology, USA), cleaved Caspase 8 (1:1000, 9496S, Cell Signaling Technology, USA), and β -actin (1:1000, 4970L, Cell Signaling Technology, USA). Subsequently, the membrane was incubated in horseradish peroxidase-conjugated goat anti-rabbit polyclonal immunoglobulin G secondary antibody (1:2000; Cat. No. sc-2004, Santa Cruz Biotechnology) for 1 hour. The bands were further detected using enhanced chemiluminescence solution (Broaddus) and visualized using a ChemiDocTM MP imaging system (BioRad, USA).The

densitometric analysis of proteins was performed using image J software. The marker protein bands were calculated and adjusted using a loading control (β -Actin).

2.13. Statistical analysis

All presented data are expressed as average of mean \pm SD of at least three replicates (n=3). Statistical significance of the data was determined using a one-way ANOVA and Student's t-test, as required, using a GraphPad Prism 9 software. The difference is considered statistically significant at p-values < 0.05 .

CHAPTER 3: RESULTS

In this work, CUR and a new CUR conjugate (CUR.SA) were encapsulated in chitosan-mannose nanoparticles by ionic gelation method. A graphical presentation of the prepared nanoparticles including CUR-NPs and CUR.SA-NPs are shown in Figure 32.

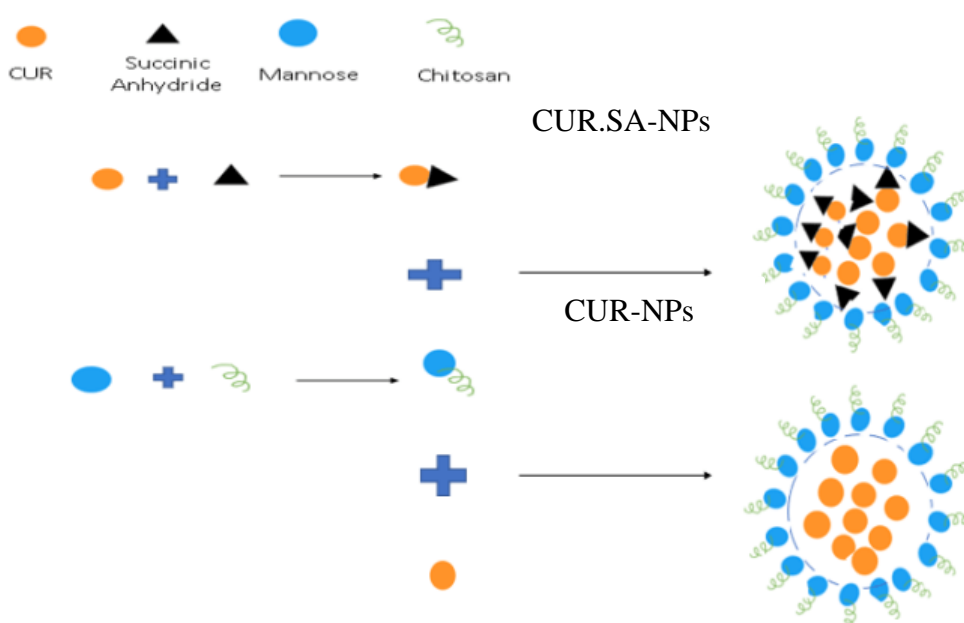


Figure 32. Graphical representation of the formulated NPs

Physicochemical characterization

3.1.1 FT-IR analysis

FT-IR was used to identify the main chemical functional groups within the raw materials, conjugates and nanoparticles (Figure 33).

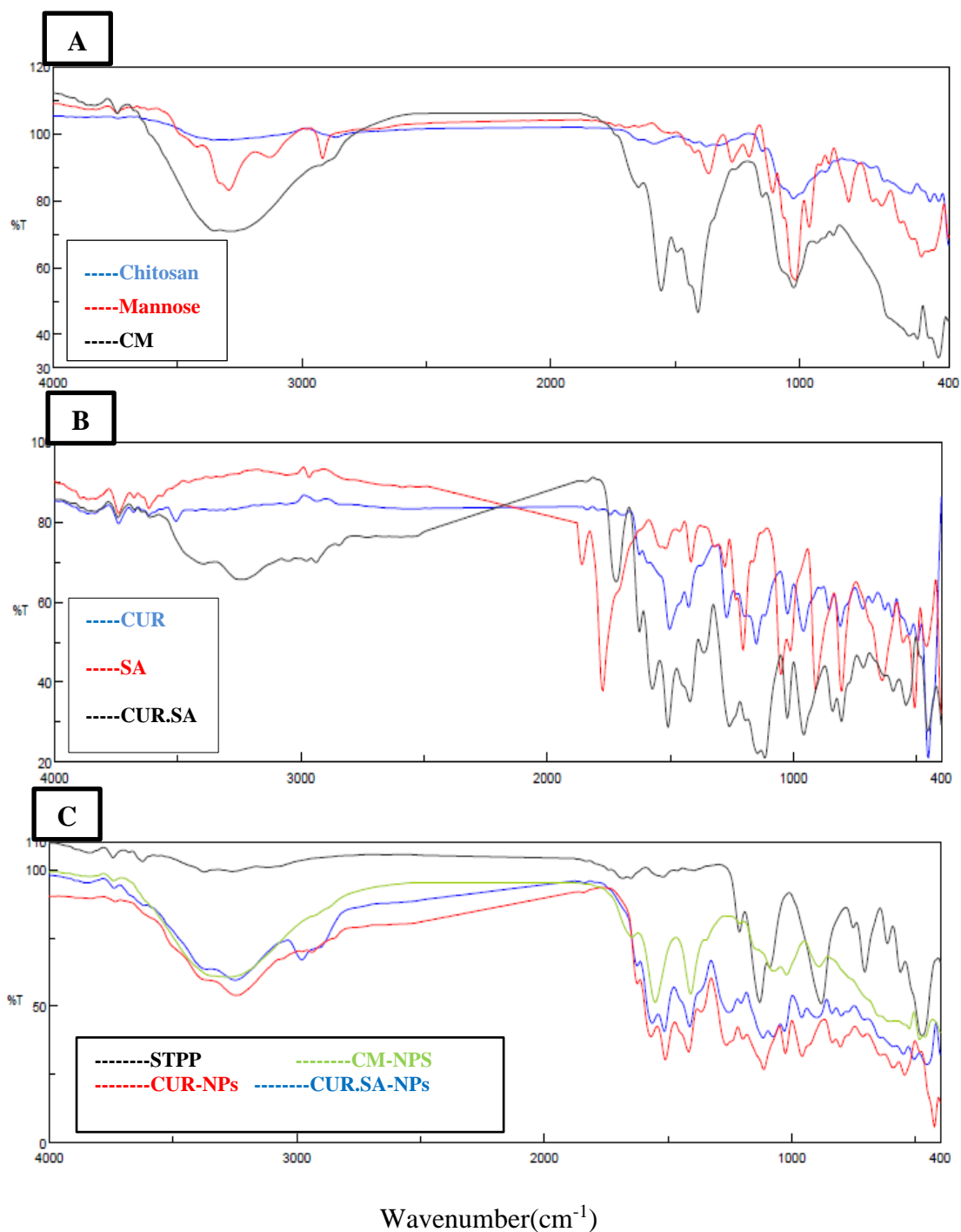


Figure 33. FT-IR spectra of (A) CS, Mannose, and CM Conjugate, (B) CUR, SA, and CUR.SA conjugate and (C) STPP, CM-NPS, CUR-NPs, and CUR.SA-NPs.

Evidence of chemical conjugation between D-mannose and CS is shown in Figure 33.A. In the FT-IR spectra of CS (Fig. 33.A), transmission peaks at 3355.53 (NH) cm^{-1} and 2865.7 cm^{-1} (CH) refer to the symmetric amine and methylene groups vibrations respectively. In general, peaks at the range 3500–2500 cm^{-1} refer to X-H vibrational stretching, where X could be O, C or N. The band at 1585.2 cm^{-1} (NH_2) is assigned to the stretching vibration of $-\text{NH}_2$ group present in CS, while the peak at 1373.07 cm^{-1} (CH) is due to vibration of C-H. The broad peak at 1022.09 cm^{-1} (CO) refers to C-O stretching vibration. FTIR spectrum of pure mannose (Figure 33.A) shows 2 characteristic peaks at 3293.82 cm^{-1} and 3127.97 cm^{-1} , which refer to the C-H vibrational stretching. Another peak at 1697.05 cm^{-1} was due to C=O aldehyde stretching. The transmission peak at 1365.35 cm^{-1} refers to methylene $-(\text{CH}_2)-$ bending vibrations, while a peak at 1014.37 cm^{-1} confirmed the vibrational stretching and wagging of C-O in mannose. In case of CM (Fig. 33.A), a strong sharp peak at 1554.34 cm^{-1} (N-H) refers to the bending of secondary amine and a peak at 1407.78 cm^{-1} (C=N) confirmed the formation of Schiff's base, which assures the formation of a new bond between mannose ligand and amine termination in CS (R-CH=N-R bond). Moreover, an intense and broad strong peak at 3282.25 cm^{-1} (OH) for mannose and a strong peak at 1022.09 cm^{-1} (CO) confirmed the presence of hydroxyl groups for mannose in high amounts within the CM conjugate.

In case of CUR (Figure 33.B), a peak at 3505.95 cm^{-1} (OH) refers to hydroxyl groups of CUR. Moreover, C=C aromatic stretching vibration at 1427.07 cm^{-1} and high intensity band at 1500.35 cm^{-1} refer to the mixed vibrations that includes stretching carbonyl bond vibrations (C=O), in plane bending vibrations around aliphatic C-C, in plane bending and stretching vibrations of aromatic C-C-H and C-C in the keto and enol configurations of CUR. Furthermore, a significant intense band at 1268.93 cm^{-1} is

attributed to the bending vibration of the C-O phenolic group. In the case of SA (Figure 33.B), a strong peak at 1774.19 cm^{-1} refers to C=O stretching. Another peak at 1203.36 cm^{-1} is due to C-O stretching of the vinyl ether in SA. For CUR.SA (Figure 33.B), a broad peak at 3251.4 cm^{-1} and a medium sharp band at 2938.98 cm^{-1} refer to O-H stretching in the carboxylic acid from SA. A strong peak at 1025.94 cm^{-1} is due to C-O stretching of the primary alcohol moiety in SA. Furthermore, a strong peak at 1261.22 cm^{-1} refers to C-O stretching in CUR. Moreover, a peak at 1720.19 cm^{-1} is due to C=O stretching coming from the carboxylic acid group in SA. Based on these observations, there is strong evidence of the formation of CUR.SA conjugate.

In the nanoparticles: CM-NPs, CUR-NPs and CUR.SA-NPs, key signatures observed previously are also present as shown in Figure 33.C, however, peaks appeared smoothed with slight shifting which can be attributed to ionic interactions between STPP and CS during gelation. The presence of CUR within the nanoparticles is largely physical, however weak interaction with STPP and CS can be attributed to the broad peaks in CUR.

3.1.2 NMR spectroscopic analysis

In order to add more credibility to the FT-IR data, ^1H NMR study was performed on CS and CM (Figure 34), with spectra obtained in deuterium oxide (D_2O). CS showed peaks at 1.90 and 3.00 ppm protons bonded to C atoms of the glucosamine ring, while signals between 3.60 and 3.90 ppm correspond to protons bonded to C atoms in the glucopyranose that are overlapped (Figure 34. A). Another peak at 4.9 ppm corresponds to protons bonded to the anomeric carbon in CS. After mannosylation (Figure 34.B), a weak peak at 2.63 ppm occurred that refers to proton linked to $-\text{NH}_2$ group that became sterically hindered by the presence of mannose. Moreover, a peak

at 8.14 ppm occurred in CM in contrast to CS, and this is due to protons from mannose within in CM. The peaks of CM have been shifted as compared to that of CS, which is a strong signal of mannosylation reaction.

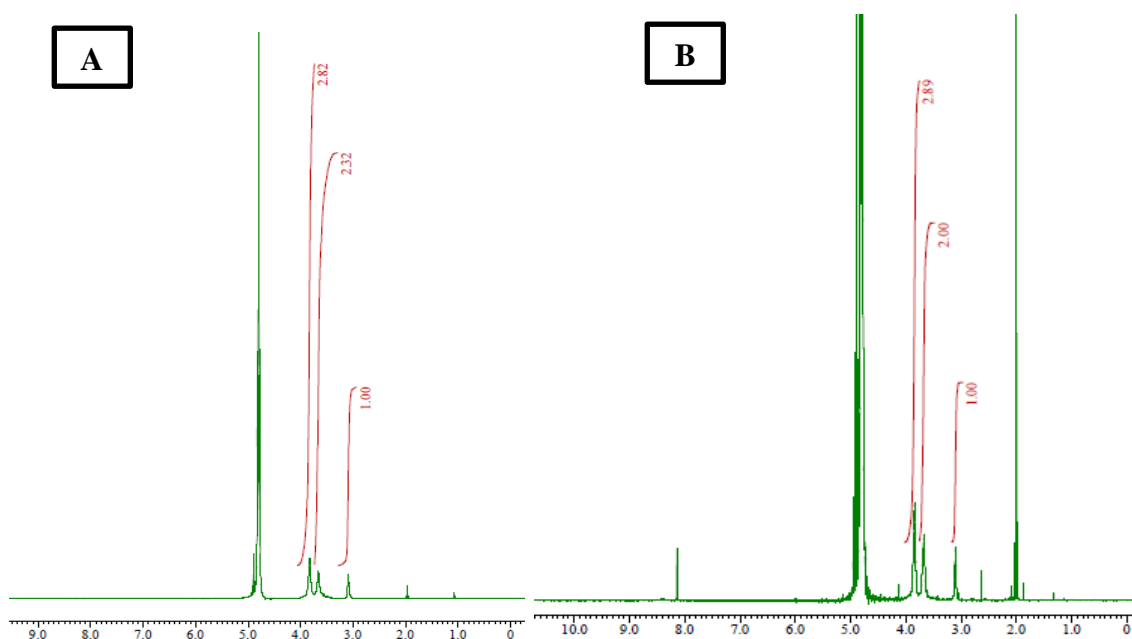


Figure 34. ¹H NMR Spectra of CS (A), and CM conjugate (B) after dissolving 4 mg of the samples in D₂O/HCl (650 μL/ 20 μL) under sonication (3 mins), at 25°C.

¹H and ¹³C NMR spectroscopy were performed on CUR.SA conjugate (Figure 35), where a new peak at 2.60 ppm appears in CUR.SA conjugate (Figure 35.B), attributable to -CH protons present in SA in contrast to free CUR (Figure 35.A). In ¹³C NMR (Figure 35.C,D), a peak at 30 ppm represents C in -CH₂ group present in SA. In addition, 2 peaks occurred at 172 ppm and 173 ppm emerging from two different C, namely carbonyl C and carboxylic acids C within SA (Figure 35.D). Thus, a conclusion with a fair degree of certainty that CUR was successfully conjugated to SA is obtained.

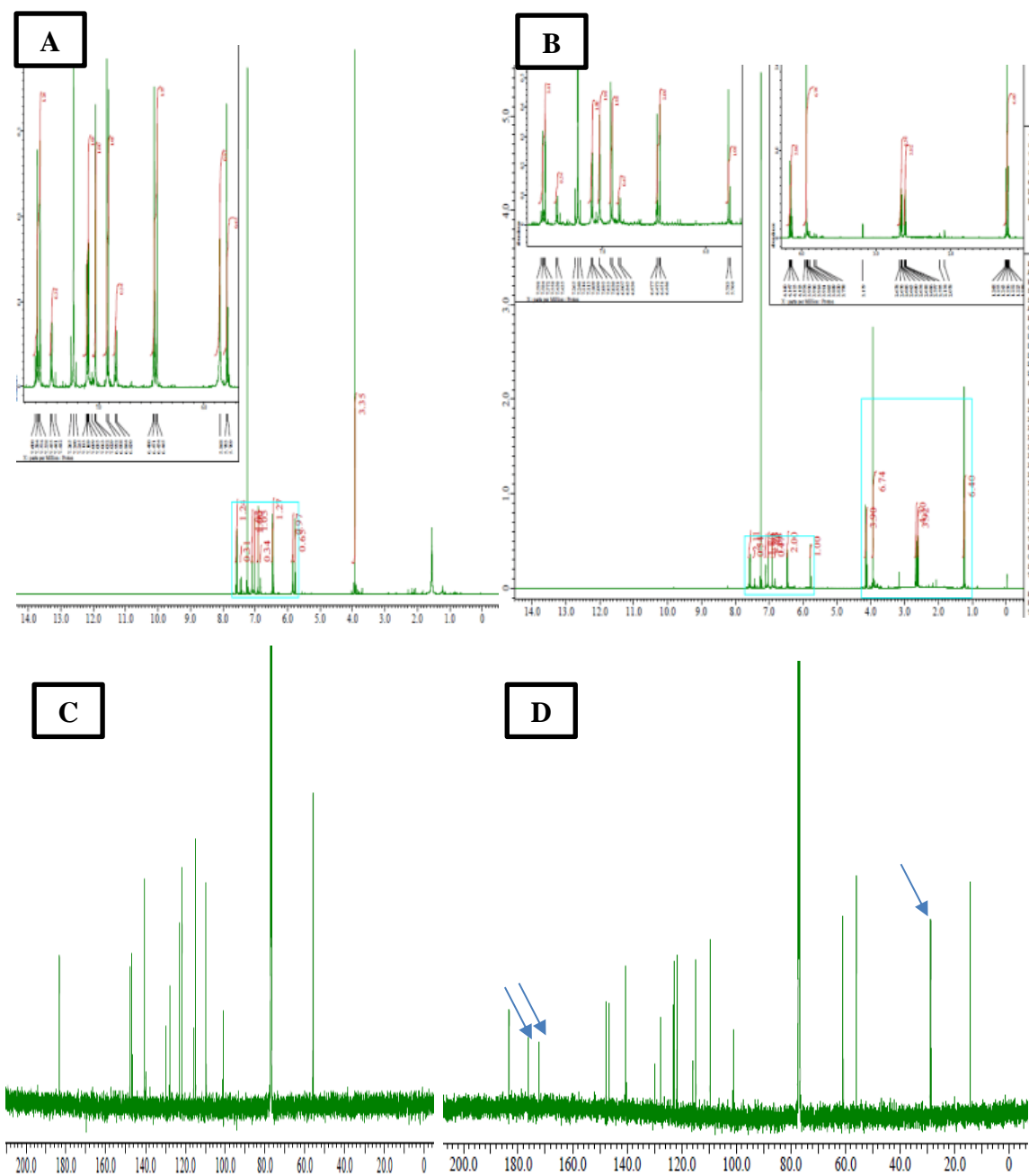


Figure 35. ^1H NMR spectra of CUR(A), CUR.SA (B) and ^{13}C NMR spectra of CUR(C), CUR.SA (D). Samples were dissolved in 600 μL of deuterated chloroform (CDCl_3).

3.1.3 Particle size and charge analysis

Various nanoparticle formulations (CM-NPs, CUR-NPs and CUR.SA-NPs) were fabricated and characterized with regard to size and surface charge using as the Zeta-sizer[®]. Table 4 presents the data, which also includes the PDI and %EE From the

data, we observed that formulation B provided the most optimal characteristics based on the formulation for further analysis and biological applications. For CM-NPs, the mean size of was 101 ± 4.3 nm, PDI value of 0.32 ± 0.05 , and zeta potential of 41.2 ± 0.15 mV. In case of CUR-NPs, the mean size was 268 ± 6 nm, PDI value of 0.294 ± 0.019 and zeta potential of 11 ± 0.75 mV. For CUR.SA-NPs, the mean size of was 342 ± 4.6 nm, PDI value of 0.137 ± 0.043 and zeta potential of 13.6 ± 0.8 mV.

Table 4. Optimization of prepared formulations

Formulation name	Nanoparticle name	Particle size (nm)	Zeta potential (mV)	%EE
A	CM-NPs	1689 ± 17	13.2 ± 0.5	-
	CUR-NPs	2348 ± 183	-1.55 ± 0.45	91.32 ± 0.03
	CUR.SA-NPs	2661 ± 2101	3.24 ± 0.98	92.45 ± 0.01
B	CM-NPs	101 ± 4.3	41.20 ± 0.15	-
	CUR-NPs	268 ± 6	11.00 ± 0.75	93.34 ± 0.40
	CUR.SA-NPs	342 ± 4.6	13.60 ± 0.80	98.46 ± 0.06
C	CM-NPs	3400 ± 432	6.84 ± 1.67	-
	CUR-NPs	4531 ± 2689	-3.75 ± 0.52	95.54 ± 0.25
	CUR.SA-NPs	30620 ± 3790	-0.74 ± 0.05	95.57 ± 0.03
D	CM-NPs	125.2 ± 1.8	32.30 ± 1.85	-
	CUR-NPs	355 ± 30	3.72 ± 0.48	34.94 ± 0.15
	CUR.SA-NPs	538 ± 22	-1.95 ± 1.4	38.34 ± 0.06
E	CM-NPs	120.4 ± 1.47	32.40 ± 1.05	-
	CUR-NPs	642 ± 50	16.80 ± 1.71	98.67 ± 0.004
	CUR.SA-NPs	686 ± 11	13.20 ± 0.72	98.49 ± 0.005

3.1.4 The encapsulation and loading efficiency of nanoparticles

After preparing CUR-NPs and CUR.SA-NPs, the amount of CUR and CUR.SA that remained in the supernatant of the solution was analyzed using HPLC system. From the optimal formulation B, the % EE was equal to 93.34 ± 0.40 for CUR-NPs, and 98.46 ± 0.06 for CUR.SA-NPs (Table 4). Furthermore, formulation B has yielded a drug loading 39.81 ± 0.17 for CUR-NPs, and 42.02 ± 0.02 for CUR.SA-NPs.

3.1.3 Stability test of CUR and CUR.SA conjugate

The chemical stability of free CUR and CUR.SA conjugate was assessed over 6 hours using a reversed-phase HPLC with UV-VIS detection at 425 nm. Stability stresses included dark, roomlight (florescent), and in sunlight. Plots of the area under the curve (AUC) vs. time (Figure 36.A) showed no significant degradation rate of free CUR in dark and roomlight conditions ($p > 0.05$) after 6 hours of exposure, signifying that free CUR was stable in the tested conditions. On the other hand, CUR degradation was significant (Figure 36.A) in sunlight condition after 6 hours of exposure ($p < 0.0001$). However, CUR.SA degradation was not significant ($p > 0.05$) in dark and roomlight conditions after 4 hours of exposure, whilst significant degradation rate was noticed after 6 hours of exposure to sunlight (Figure 36.B).

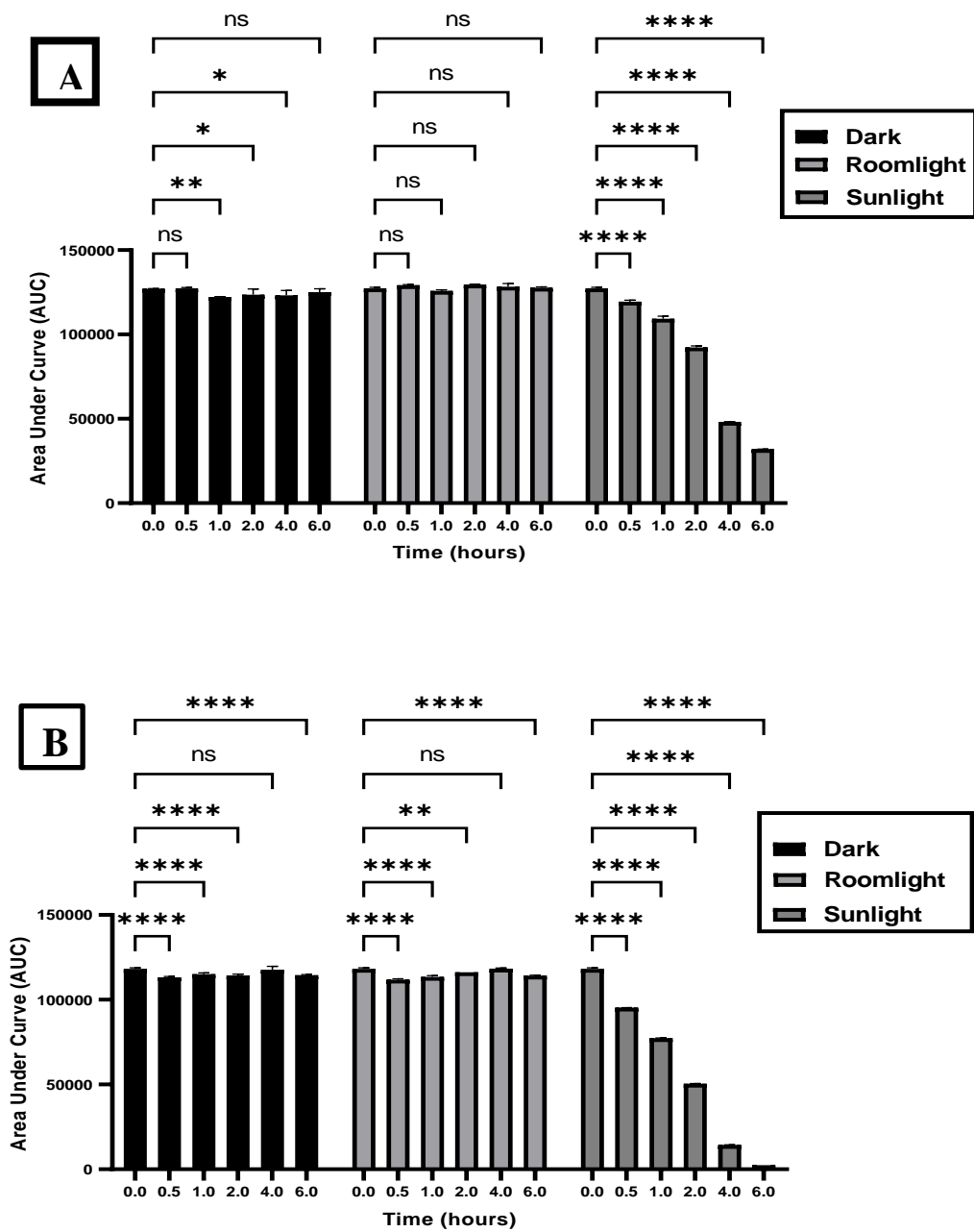


Figure 36. Stability test of free CUR (A), and CUR.SA conjugate (B). Data is expressed as mean \pm SD (n=3), statistical analysis using two-way ANOVA, Dunnett's test, (ns = not significant, * p< 0.05, **p < 0.01 and ***p < 0.001, and ****p < 0.0001 indicates statistical significance compared to control cells (time 0)).

3.1.6 Solubility of CUR and CUR.SA conjugate test

To determine whether the synthesized CUR.SA conjugate is more soluble than pure CUR in aqueous and ethanolic media, a solubility study was conducted (Figure 37). The resulted data indicate that pure CUR was more soluble than CUR.SA conjugate ($p < 0.05$) in ethanol. In contrast, CUR.SA conjugate showed a higher solubility in water compared to free CUR ($p < 0.05$). Thus, the improvement of CUR solubility in aqueous media for the prepared conjugate is confirmed.

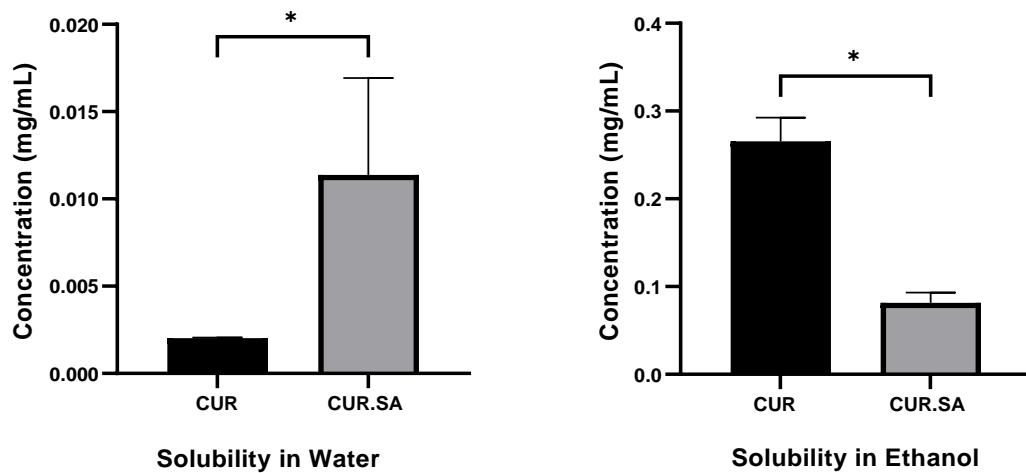


Figure 37. Solubility test of CUR.SA conjugate in different media (water and ethanol). Data is expressed as mean \pm SD (n=3). Statistical significance was calculated using student' t-test (* $p < 0.05$ indicates statistical significance).

3.1.7 AFM analyses

The surface topography and morphology of the produced nanoparticles were observed on AFM. Figure 38 displays the 2D and 3D rendered images of CM-NPs (A), CUR-NPs (B), and CUR.SA-NPs (C). The figures show distinct nanoparticles that are spherical in shape and have a uniform distribution. The average surface roughness is a parameter used to assess the surface roughness and this value was ranged between -13.590 nm to 27.109 nm for CM-NPs (Skewness= 0.34 nm), from -13.801 nm to 21.792 nm for CUR-NPs (Skewness= 0.57 nm), and between -36.602 nm

to 74.815 nm for CUR.SA-NPs (Skewness= 2.91 nm). Overall, it is also clear that the prepared NPs have a smooth surface, while observed roughness is much smaller than that of plane size of NPs. This could be explained by the composition of used CS polymer (CS) which is flexible and prone to collapse from tapping by the cantilever of the AFM.

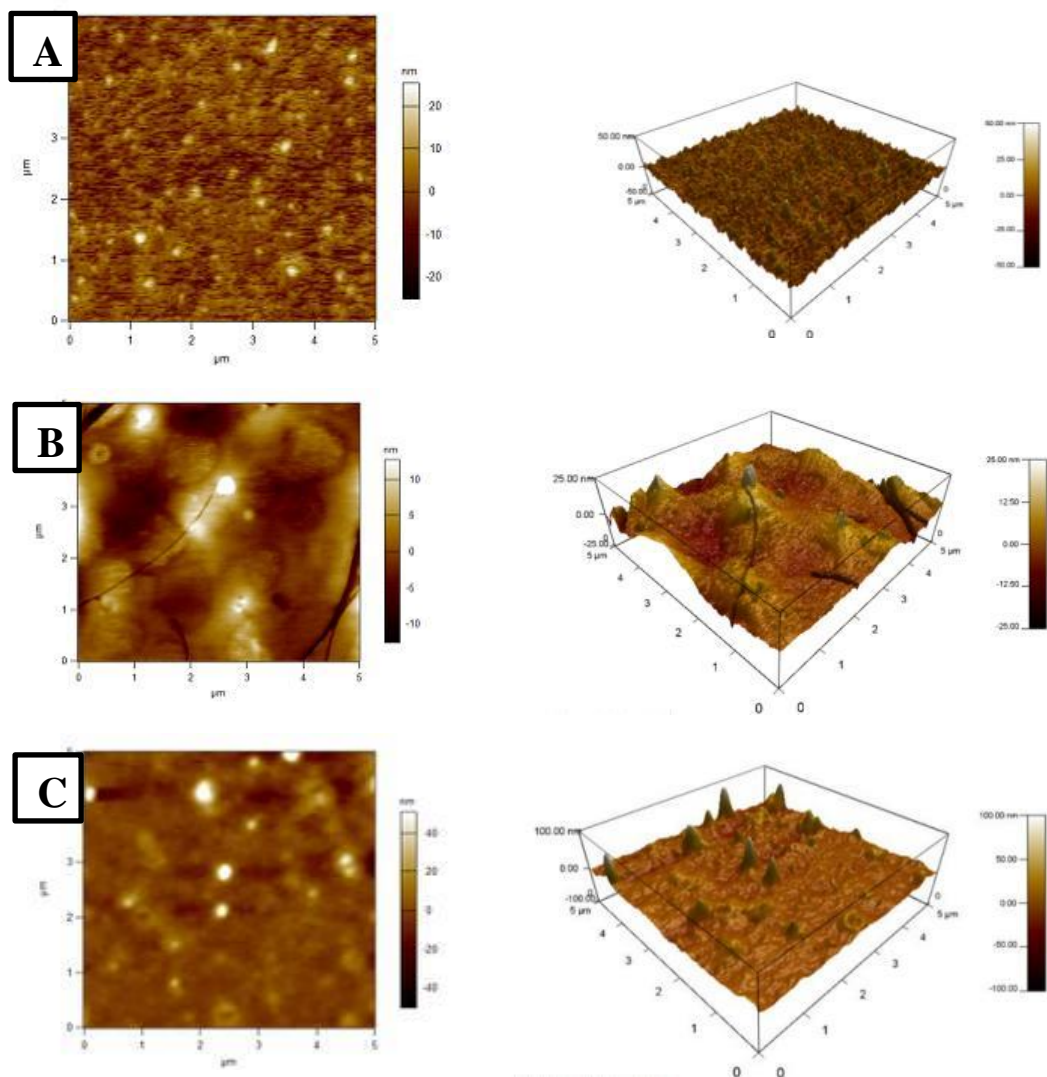


Figure 38. AFM images of CM-NPs (A),CUR-NPs (B), and CUR.SA-NPs (C).

3.1.8 EDX Analysis

The EDX analysis is presented in Figure 39, for CS, STPP, CM-NPs, CUR-NPs, and CUR.SA-NPs. The targeted elements include carbon (C) oxygen (O), nitrogen (N), sodium (Na) and phosphorus (P). The intensity values of the elements for CS, and extracted data is presented in Table 5. The presence of Na and P in the formed nanoparticles is an indication that the formation of crosslinking with STPP was successful. Furthermore, EDX analysis confirmed the absence of impurities.

Table 5. Elemental composition of samples (% Wt).

Sample	% N	% O	% C	% Na	% P
CS	18.01	27.91	54.08	-	-
STPP	-	49.11	-	28.48	22.41
CM-NPs	27.40	32.02	34.22	4.91	1.45
CUR.SA-NPs	26.59	27.83	36.16	9.04	0.38
CUR-NPs	18.80	24.51	51.53	4.68	0.48

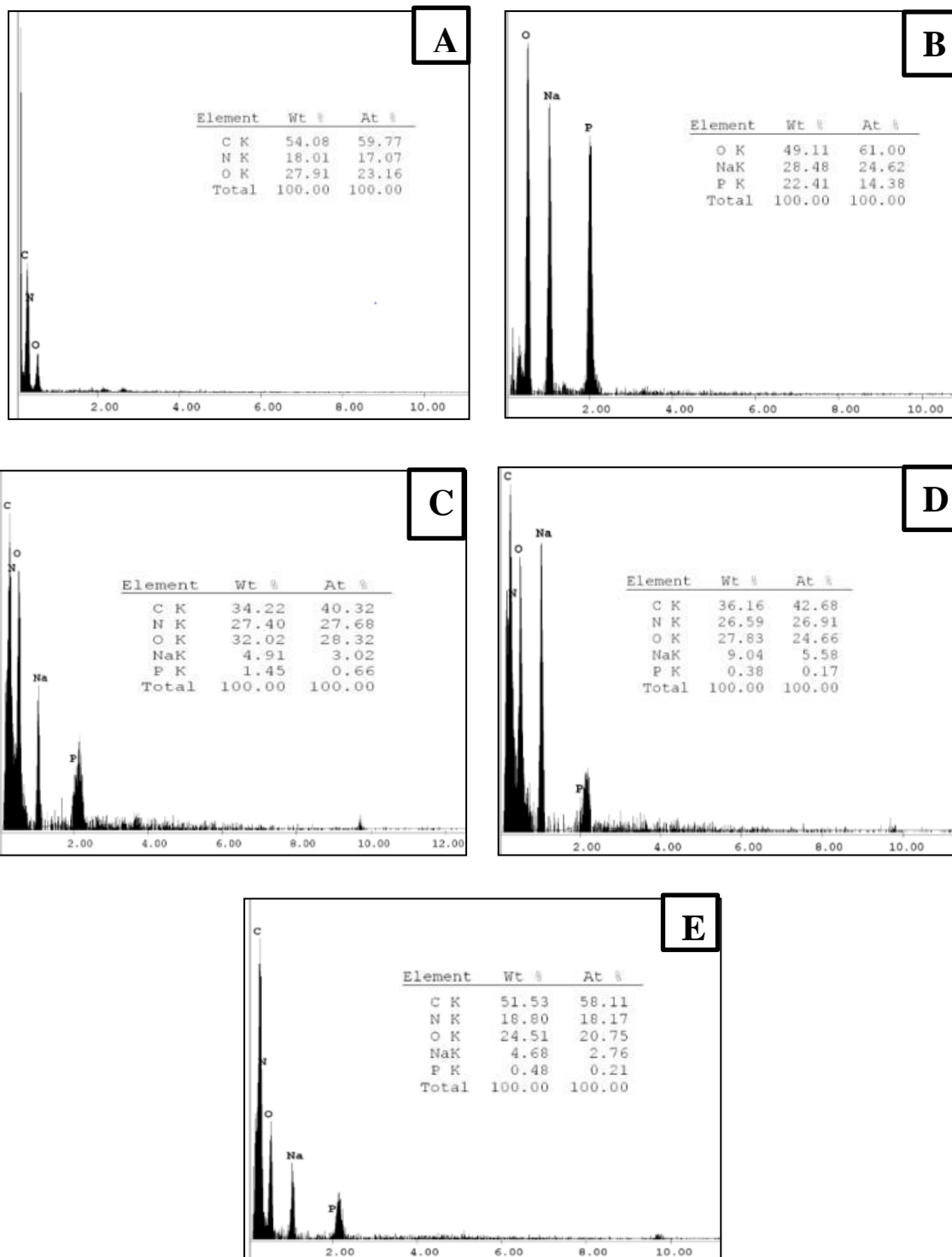


Figure 39. EDX spectra of CS (A), STPP (B), CM-NPs (C), CUR-NPs (D), and CUR.SA- NPs (E).

3.1.9 Morphology analysis of NPs

The morphology of the CM-NPS, CUR-NPs, and CUR.SA- NPs was assessed through SEM. As shown in Figure 40, the NPs are spherical and uniform in shape and in agreement with the results obtained in the Zeta Sizer analysis, which were 101 nm (± 4.3 nm) for CM-NPs (A), and 268 nm (± 6 nm) for CUR-NPs (B), and 342 nm (± 4.6 nm) for CUR.SA-NPs (C).

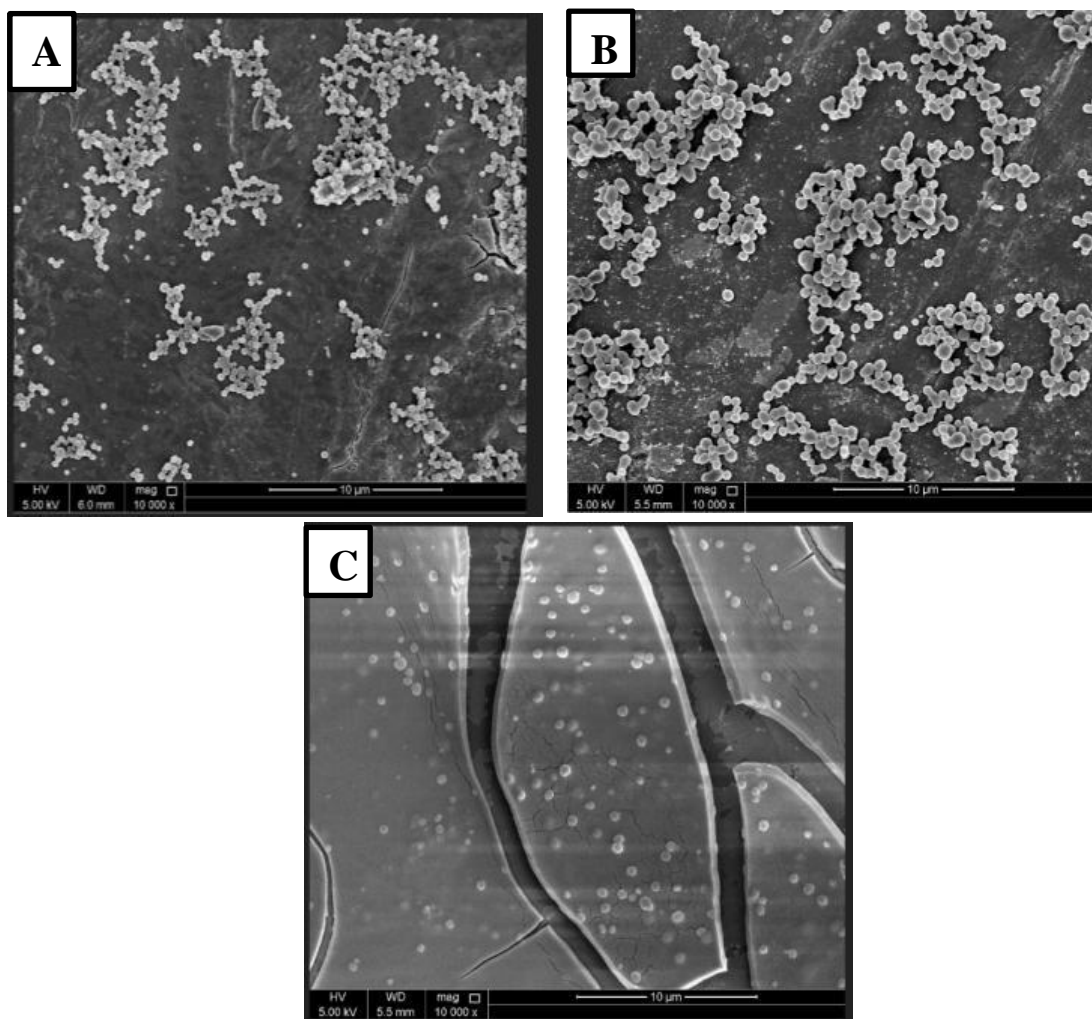


Figure 40. SEM images proving the formation of CM-NPs (A), CUR-NPs (B), and CUR.SA-NPs (C).

3.1.10 XRD analyses

XRD analysis was used to gather information about the physical state of CUR and CUR.SA within the nanoparticle carriers. In the case of free CS, as shown in Figure 41, two strong diffraction peaks are observed at $2\theta = 10.5^\circ$ and 20.43° . However, after mannosylation of CS the peak at 10.5° disappeared and peak at 20.43° decreased in intensity as compared to free CS. Furthermore, after formulation of CM-NPs, both peaks disappeared completely, which reflects a transformation to an amorphous form of the obtained NPs. In the XRD patterns for free CUR, multiple crystalline signals are observed at 8.93° , 12.25° , 14.60° , 17.28° , 18.29° , 21.36° , 23.50° , 24.64° , 25.67° , 27.36° , and 29.08° , which confirms the crystalline property of free CUR. However, after conjugation to SA, all peaks present in free CUR disappeared, which demonstrates the disruption of the crystalline form of CUR after conjugation to SA. Upon further encapsulation of CUR and CUR.SA within CM-NPs, no sharp peaks were noticed, which confirms the transformation of CUR-NPs and CUR.SA-NPs into the amorphous configuration. Amorphous manifestation ensures improved solubility, which is desirable in the present circumstance since deployment in cells will promote effective therapeutics.

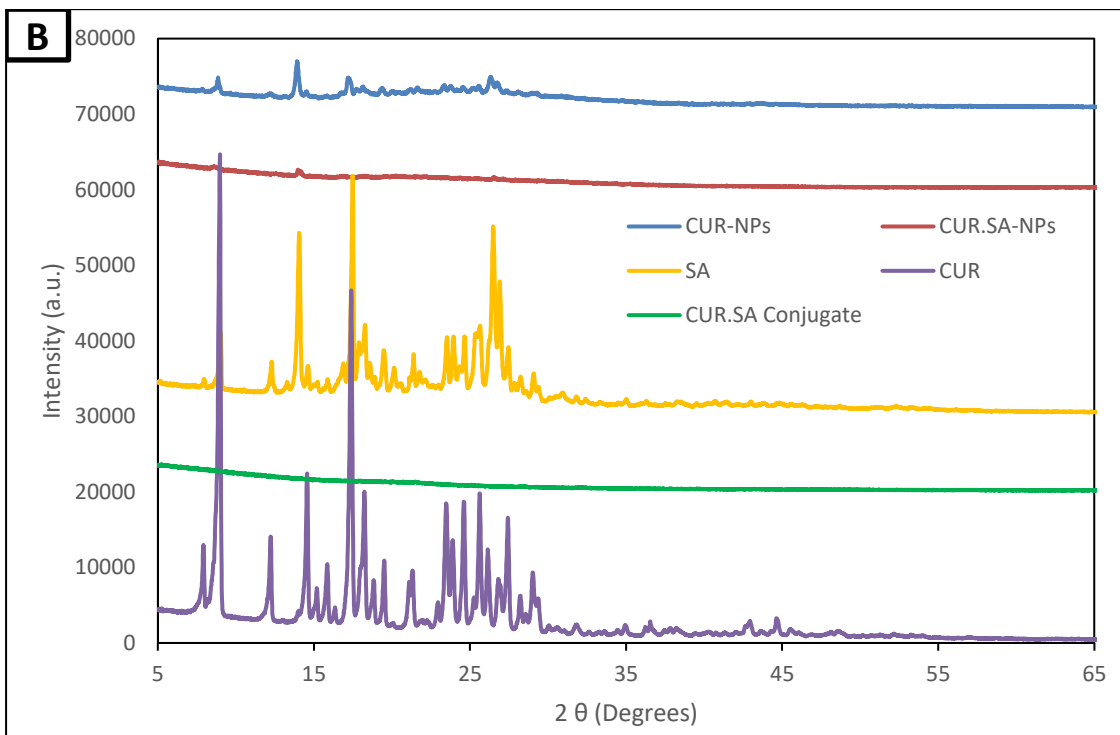
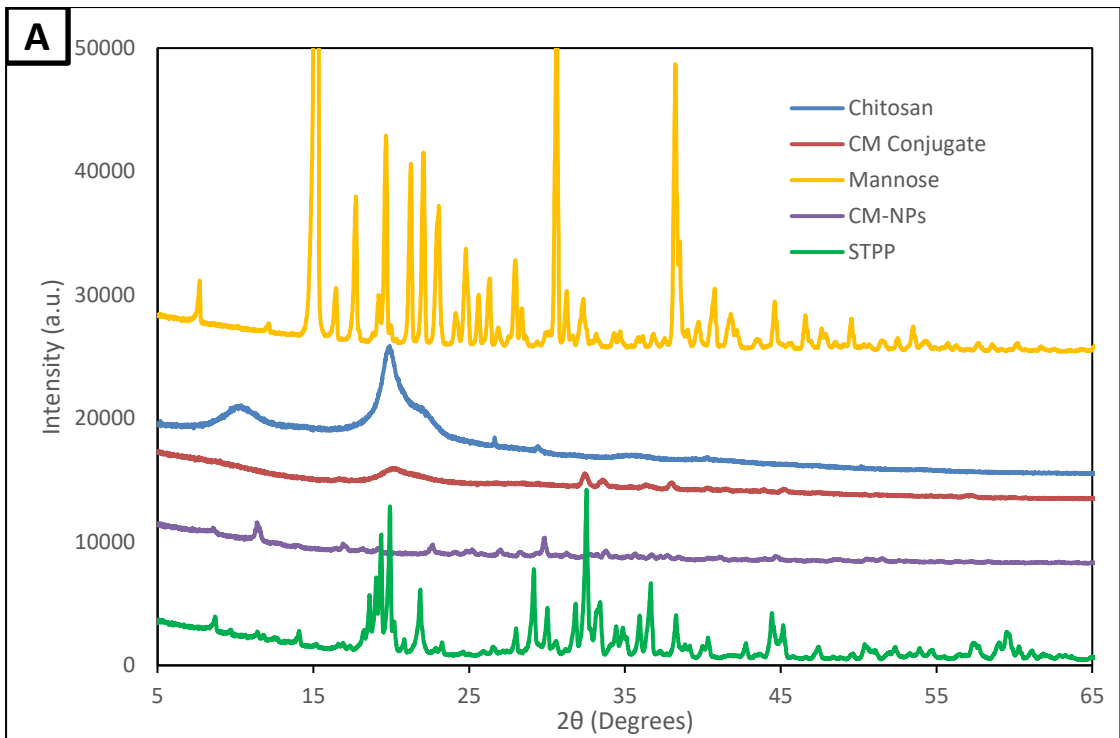


Figure 41. XRD patterns of CS, Mannose, CM Conjugate, STPP and CM-NPs (A), CUR, SA, CUR-SA Conjugate, CUR-NPs, and CUR.SA-NPs (B).

3.1.11 TGA Analyses

Thermogravimetric analysis of CS, mannose, CUR, CUR.SA, CM-NPs, CUR-NPs, and CUR.SA-NPs was conducted in order to study their thermal stability profile. The thermal degradation profiles of the formulated nanoparticles are shown in Figure 42. A similar degradation profile was observed for both CUR and CUR.SA conjugate with only 2% of weight loss until 200 °C. A weight loss of 50% for CM conjugate compared to CS that underwent 60% loss in weight at 500 °C was observed, which indicates that CS mannosylation improved CS stability by 10%. Up to 500 °C, CUR-NPs, and CUR.SA-NPs underwent a uniform and smooth weight loss of approximately 60%, which reflects a higher thermal stability compared to the observed profile of free CUR at 500 °C.

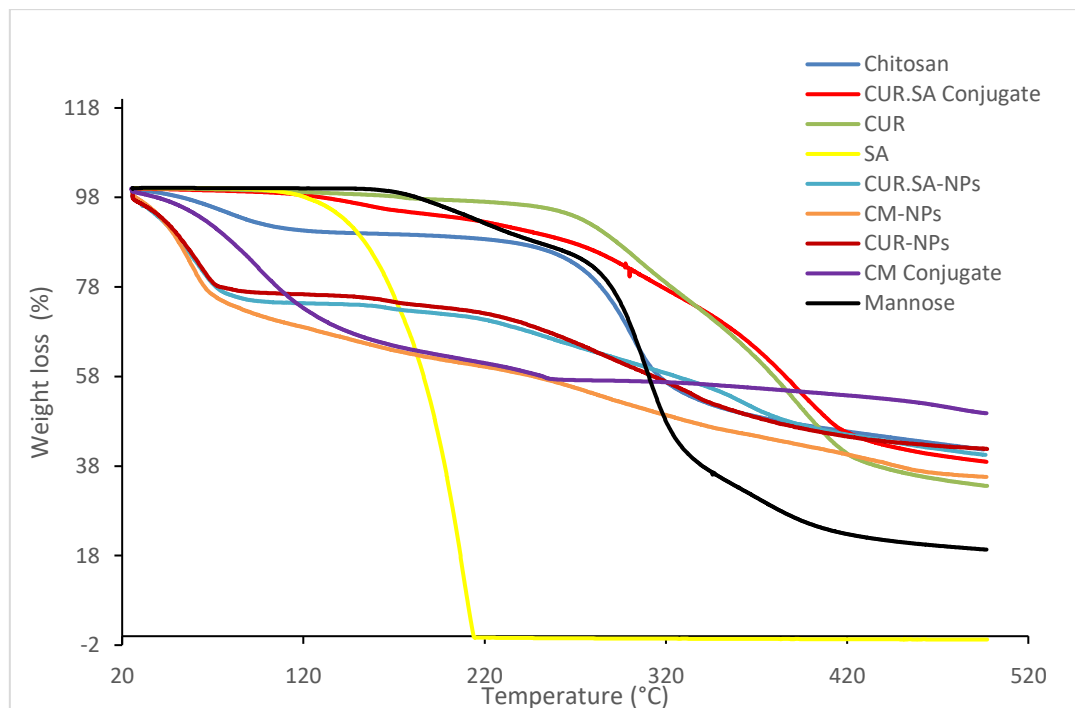


Figure 42. TGA curves of Chitosan, Mannose, CM Conjugate, CM NPs, CUR, SA, CUR.SA Conjugate, CUR-CM NPs, and CUR.SA-CM NPs.

3.2 Drug release from prepared NPs

Drug release profiles of CUR and CUR.SA- loaded CM-NPs were investigated to assess the potency of the studied carrier in delivering the drug towards the targeted colonic region. Drug release profiles of the prepared CUR-NPs and CUR.SA-NPs were assessed in PBS (pH 6.8 and pH 1.2) at predetermined intervals until 72 hours to assess the release rate of the drug from the carriers. From the data presented in Figure 43.A, CUR release from the prepared CUR-NPs indicates a burst release in the first 2 hours by 30% at pH 1.2 and pH 6.8, followed by a constant and slow release up to 72 hours. In the case of Figure 43.B, a similar drug release profile was observed from CUR.SA-NPs by at 32% at pH 1.2 and 30% at pH 6.8 in the first 2 hours followed by a constant and slow release up to 72 hours. Consequently, the constant release of CUR from both prepared nanoformulations indicates the protective properties of the carrier. Furthermore, CUR release from both nanoformulations was slightly higher in pH 1.2 compared to pH 6.8.

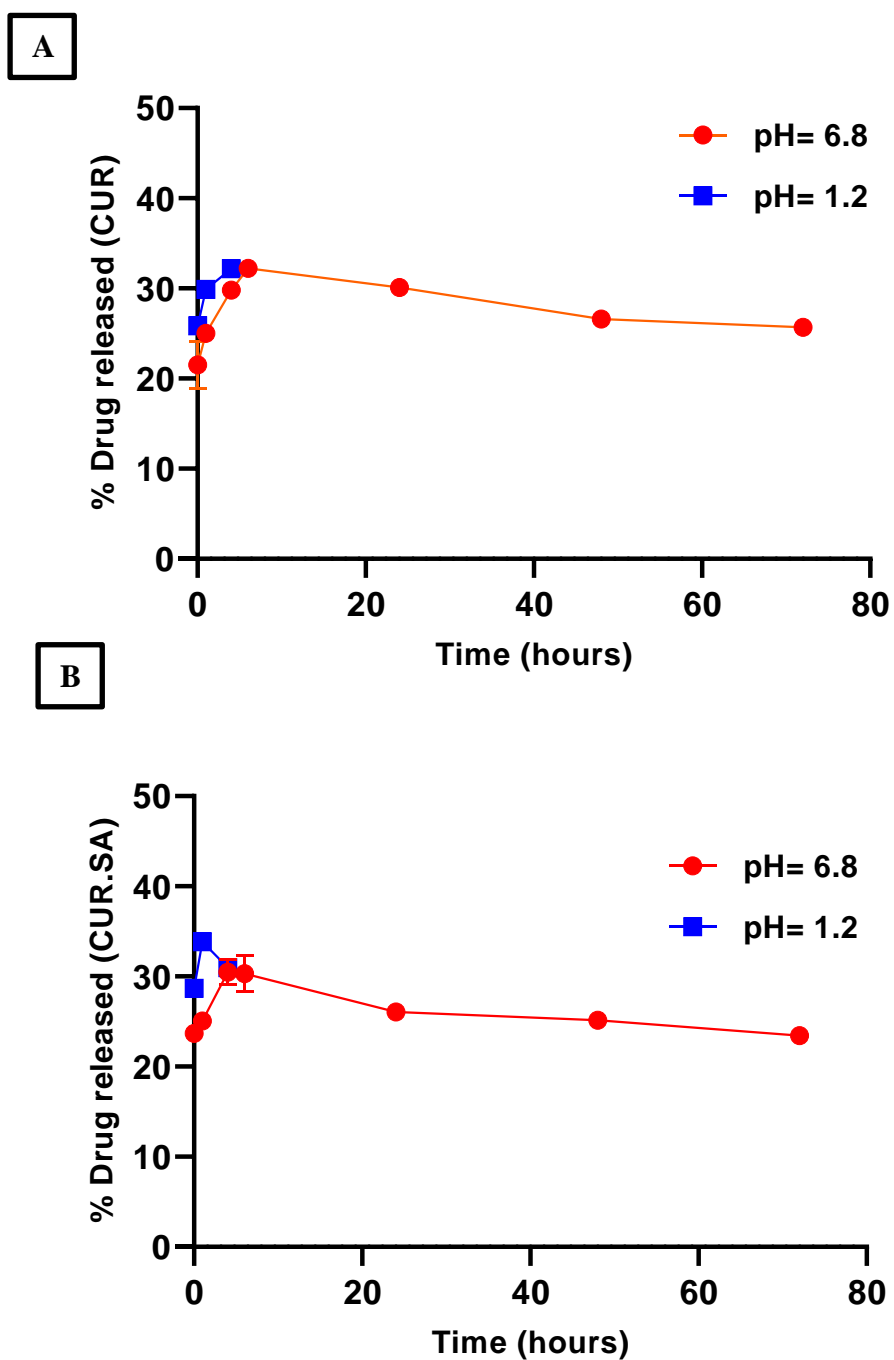


Figure 43. In vitro drug release profiles of the prepared CUR-NPs (A), and CUR.SA-NPs (B) in PBS, at pH 6.8 and pH 1.2. Data is expressed as mean \pm SD (n=3).

3.3 Stability test of nanoparticles

3.3.1 Structural assessment

To assess the structural integrity of the under typical cell growing conditions, CM-NPs, CUR-NPs, and CUR.SA-NPs were incubated in DMEM and RPMI media supplemented with 10% FBS for 24 and 48 hours in typical cell growing conditions. After the incubation periods, variations in surface morphology were assessed using AFM, and resulting images are shown in Tables 6 and 7. The obtained results display that the NPs retained their spherical morphology in both media during the incubation period up to 48 hours. Thus, the stability of the NPs is confirmed for this time period, and it is expected that uptake of the nanoparticles is likely to occur during this time frame.

Table 6. NPs incubation in DMEM culture media.

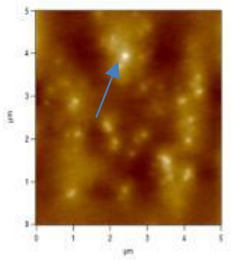
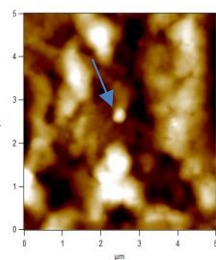
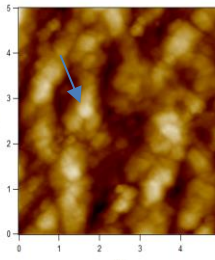
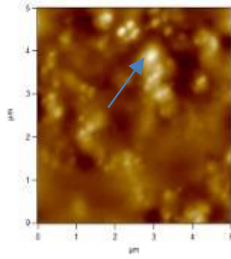
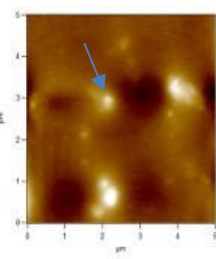
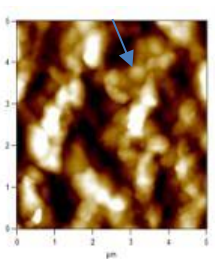
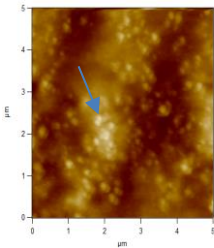
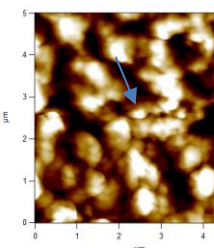
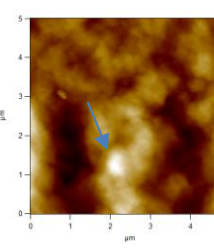
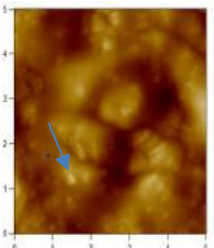
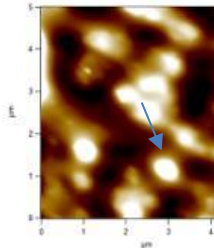
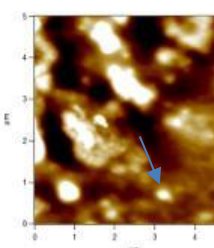
Incubation time (Hours)	CM-NPs	CUR-NPs	CUR.SA-NPs
24 Hours			
48 Hours			

Table 7. NPs incubation in RPMI culture media.

Incubation time (Hours)	CM-NPs	CUR-NPs	CUR.SA-NPs
24 Hours			
48 Hours			

3.3.2 Storage condition effect

The stability of formulated CUR-NPs and CUR.SA-NPs during storage at 4°C and 37°C was assessed by measuring changes in particle size, zeta potential and PDI (Figure 44). No significant changes in size of CUR-NPs after 28 days at 4°C were noticed (Figure 44.A). However, at 37°C, a significant increase (539 ± 15) was observed on day 28 compared to the average size on day 1, 7, 14, and 21 days. The PDI was always <0.5 in all at both storage conditions with no differences observed between their means ($p > 0.05$). Furthermore, the zeta potential remained positive and high at both temperatures. In the case of CUR.SA-NPs, no significant variations in the size of nanoparticles were noticed after 28 days of storage at 4°C, (Figure 44.B). However, at 37°C, a significant rise (536 ± 2) was observed on day 28 compared to averages on day 1, 7 and 14, and 21. Moreover, the PDIs of CUR.SA-NPs remained <0.5 at both

temperatures with no difference in their means ($p > 0.05$). The Zeta potentials also remained positive and high at both temperatures. Thus, the prepared formulations exhibit a temperature-dependent stability pattern.

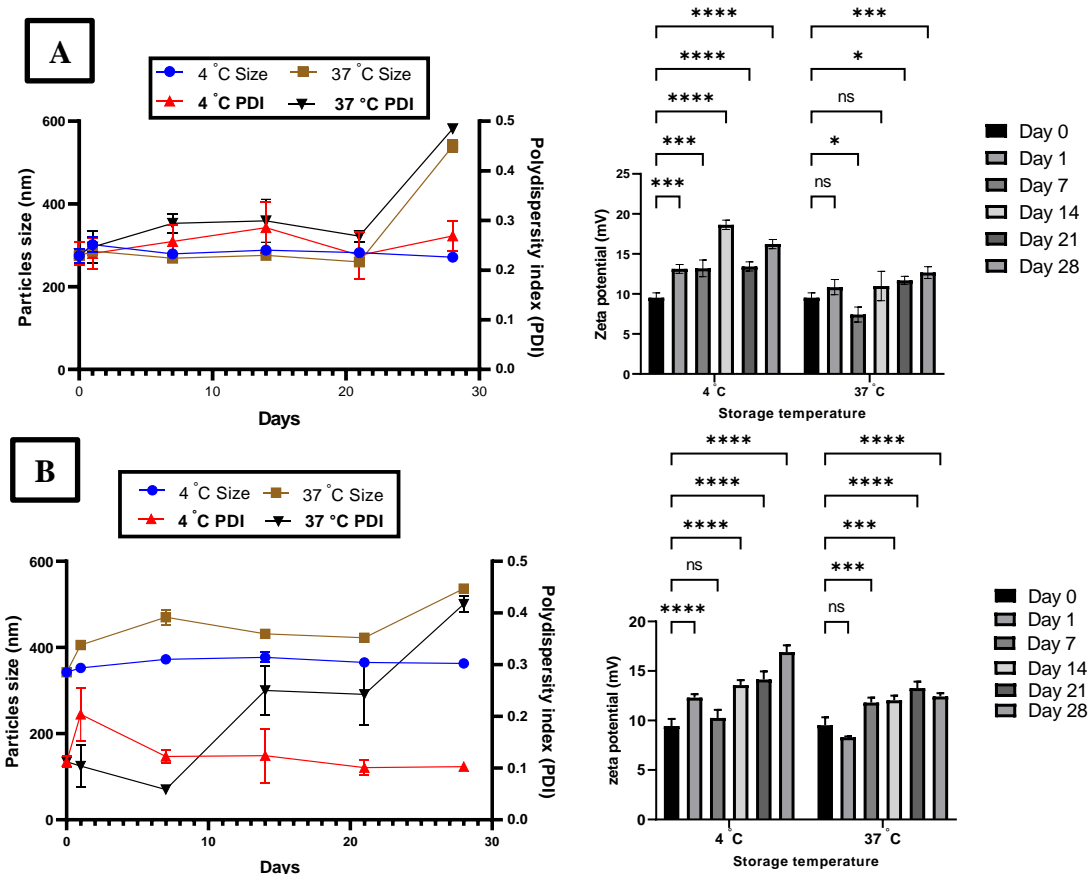


Figure 44. Stability test of the mean size (nm), Zeta potential (mV), and PDI of the CUR-NPs (A) and CUR.SA-NPs (B), at 4 °C and 37 °C, during 28 days of storage. Results are expressed as mean \pm SD. Statistical analysis using two-way ANOVA, Dunnett's test, (ns= not significant, * $p < 0.05$, ** $p < 0.01$ and *** $p < 0.001$, and **** $p < 0.0001$ indicates statistical significance compared to control cells (time 0)).

3.4 In vitro cell evaluation of formulations

3.4.1 Cell cytotoxicity

Cell viability studies are used to assess the anti-cancer properties of formulations on various CRC cell lines, as well as analyzing their time and dose responses to the applied treatments. CCK-8 assay, which is a highly water-soluble tetrazolium salt, is a colorimetric assay that exhibits greater detection sensitivity

compared to other tetrazolium salts-based assays such as MTT assay (190). There is a correlation between the amount of the produced formazan dye by cellular dehydrogenase enzymes and the number of living cells. Thus, the cell viability is estimated by measuring the optical density (OD) of the formazan at 450 nm using a microplate reader. The effect of different doses of CUR-NPs and CUR.SA-NPs on cell viability was assessed using HCT-116 and SW-480 cell lines exposed to different the concentrations of the formulations for 24 and 48 hours.

Figure 45 illustrates the effect of free CUR, CUR.SA conjugate, CM-NPs, CUR-NPs, and CUR.SA-NPs on the % cell viability of SW480 cells. From Figure 45.A, we observe that a decrease in the % cell viability was occurred upon increase in CUR-NPs concentration, which illustrates that CUR-NPs induced a dose response effect on the treated cell line, and a significant difference was detected between the treatment concentrations (10 and 25 μ M) compared to free CUR ($p < 0.05$). A similar trend was observed with CUR.SA-NPs treatment where a dose response effect was also noted, and a significant difference was noticed between the treatment concentrations (10 and 25 μ M) compared to CUR.SA conjugate ($p < 0.05$). After 48 hours of treatment (Figure 45.B), significant differences between the % viability of cells treated with free CUR and CUR-NPs were observed at all doses ($p < 0.05$). A similar trend is also observed between CUR.SA conjugate and CUR.SA-NPs treatment shown in Figure 45.B. SW480 cells were also treated with free SA (10 and 100 μ M), and no cytotoxic effect was observed until 48 hours of treatment (Figure 46). Thus, CUR anticancer property was not altered after conjugation to SA.

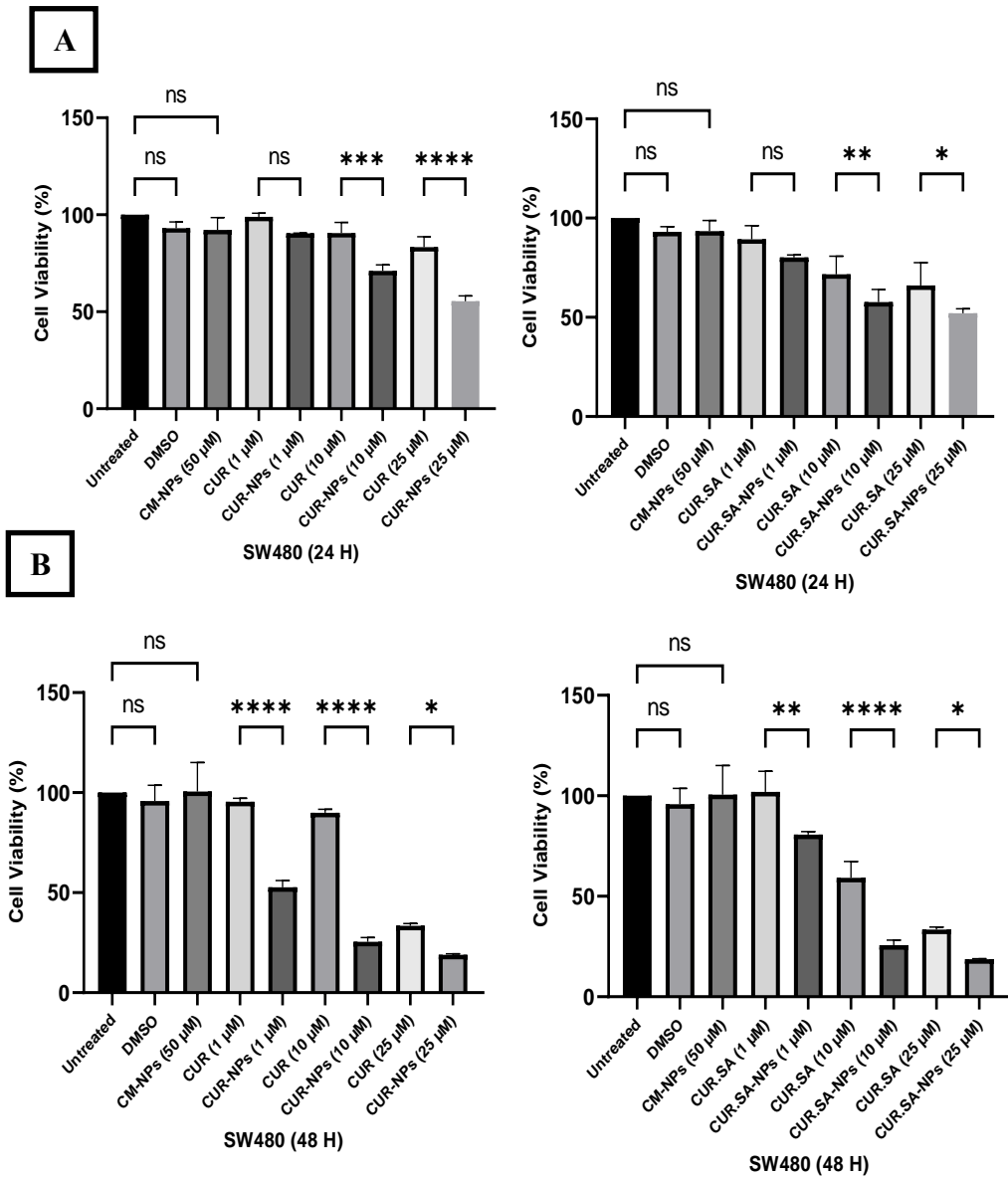


Figure 45. SW480 cell viability treated after 24 hours (A) and after 48 hours (B) using CCK-8 assay. Data are expressed as a percentage of the untreated control, viable cell levels < 75% were taken to indicate cytotoxic induction (error bars = SD; n=3). Statistical significance was calculated using 1-way ANOVA and Šidák test (ns: not significant; (*p < 0.05, **p < 0.01; ***p < 0.001, ****p < 0.0001 indicates statistical significance).

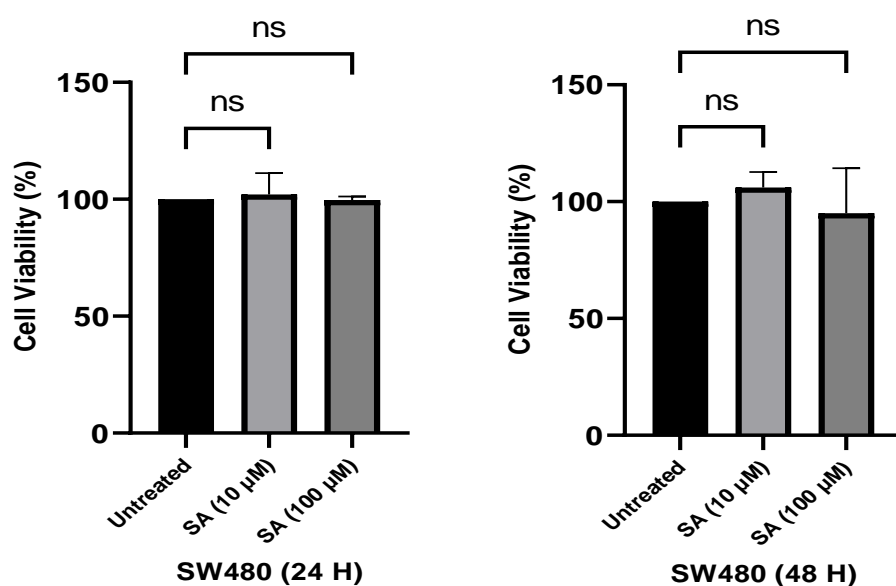


Figure 46. SW480 cell viability treated Free SA (10 and 100 μM), after 24 and 48 hours using CCK-8 assay. Data are expressed as a percentage of the untreated control, viable cell levels $< 75\%$ were taken to indicate cytotoxic induction (error bars = SD; $n=3$). Statistical significance was calculated using 1-way ANOVA and Dunnett's test (ns: not significant; $*p < 0.05$, $**p < 0.01$; $***p < 0.001$, $****p < 0.0001$ indicates statistical significance).

Figure 47 shows the effect of free CUR, CUR.SA conjugate, CM-NPs, CUR-NPs, and CUR.SA-NPs on the % cell viability of HCT116 cell line within 24 and 48 hours. The % cell viability was calculated in relation to untreated cells. From Figure 47.A, a significant decrease in the % cell viability was observed upon CUR-NPs treatment (10 μM) compared to free CUR ($p < 0.05$) after 24 hours. In Figure 47.A, a similar trend was observed with CUR.SA-NPs treatment where a dose response effect was observed, and a significant difference was noticed between treatment concentrations (1 μM) compared to CUR.SA conjugate ($p < 0.05$). After 48 hours, significant differences between the % viability of cells treated with free CUR and CUR-NPs were observed at 1 μM dose ($p < 0.05$). A similar trend is also displayed in Figure 47.B between CUR.SA conjugate and CUR.SA-NPs treatment with a significant difference at 1 and 10 μM doses ($p < 0.05$).

Cells were also treated with free SA to confirm that CUR cytotoxicity was not affected after the conjugation. After cell treatment using different concentrations of free SA (10 and 100 μM), no significant cytotoxic effect ($p > 0.05$) was noticed after 48 hours of treatment (Figure 48).

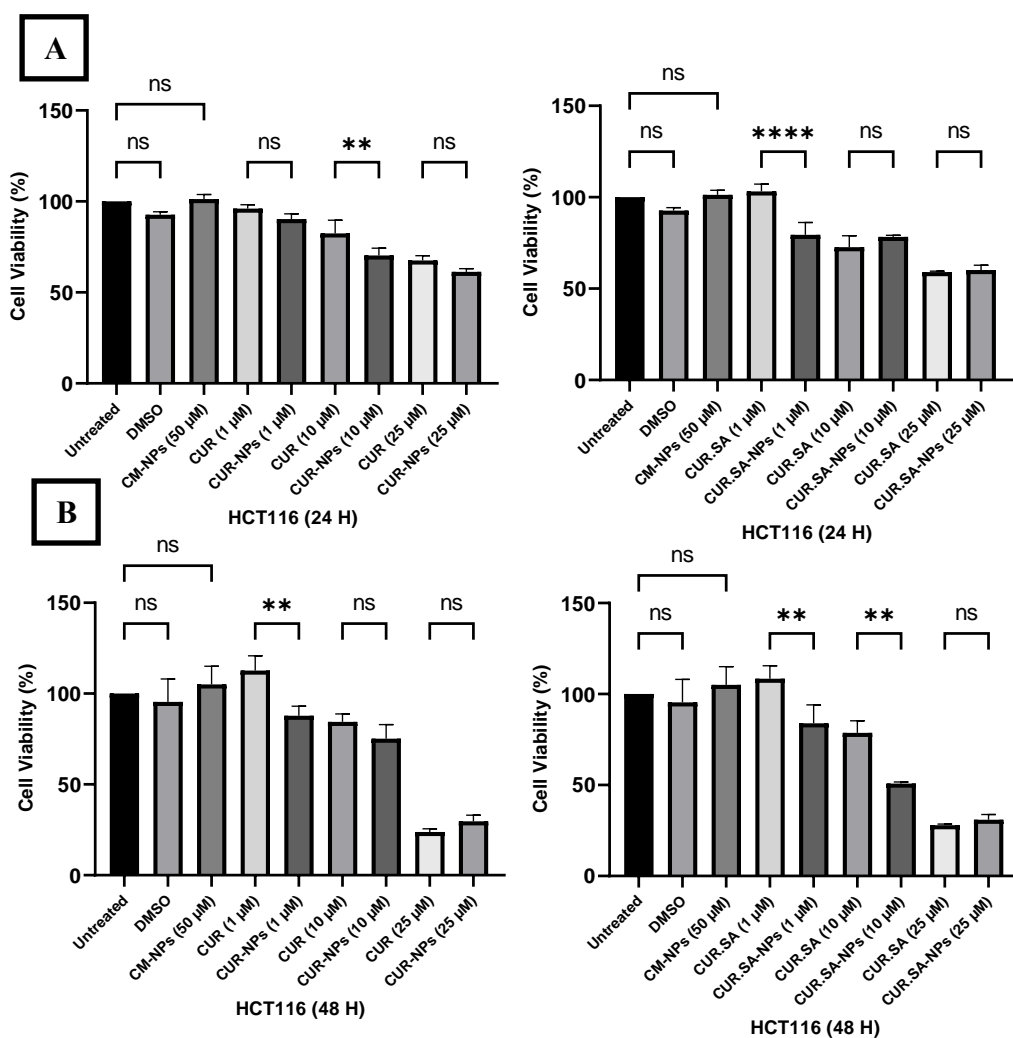


Figure 47. HCT116 viability treated after 24 hours (A) and after 48 hours (B) using CCK-8 assay. Data are expressed as a percentage of the untreated control, and viable cell levels $< 75\%$ were taken to indicate cytotoxic induction (error bars = SD; $n=3$). Statistical significance was calculated using 1-way ANOVA and Šidák test (ns: not significant; $*p < 0.05$, $**p < 0.01$; $***p < 0.001$, $****p < 0.0001$ indicates statistical significance).

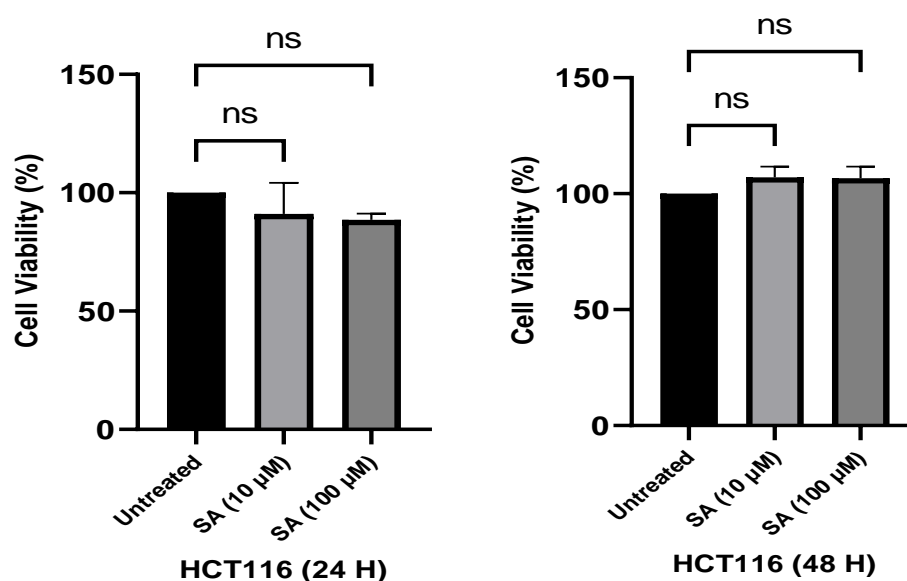


Figure 48. HCT116 cell viability treated Free SA (10 and 100 μM), after 24 and 48 hours using CCK-8 assay. Data are expressed as a percentage of the untreated control, viable cell levels < 75% were taken to indicate cytotoxic induction (error bars = SD; $n=3$). Statistical significance was calculated using 1-way ANOVA and Dunnett's test (ns: not significant; $*p < 0.05$, $**p < 0.01$; $***p < 0.001$, $****p < 0.0001$ indicates statistical significance).

3.4.2 IC₅₀ Calculation

In order to calculate the IC₅₀ of CUR-NPs and CUR.SA-NPs in SW480 and HCT116 cell lines, different concentrations were used, ranging between 1 μM to 25 μM . The IC₅₀ data are described in Table 8. From the obtained results of up to 48 hours of treatment (SW480 and HCT116), both CUR-NPs and CUR.SA-NPs displayed lower IC₅₀ values compared to free CUR and CUR.SA.

Table 8. IC₅₀ values in μM of CUR-NPs and CUR.SA-NPs on colonic cell lines. Each value is represented as means (n=3).

	24 H		48 H	
	SW480	HCT116	SW480	HCT116
Free CUR (μM)	70.58	33.58	19.57	18.21
CUR-NPs (μM)	26.82	32.44	8.64	17.84
Free CUR.SA (μM)	52.07	27.29	17.34	17.70
CUR.SA-NPs (μM)	24.05	32.10	11.01	15.86

3.4.3 Effects of nanoformulations on morphology of CRC cell lines

A phase-contrast inverted microscope was used in order to observe the morphological changes of SW480 and HCT116 cells after treatment with free CUR, CUR.SA conjugate, CUR-NPs, CUR.SA-NPs, and untreated cells. In the case of SW480 cells, untreated cells clearly exhibited flattened attachment on the surface (Figure 49). Upon treatment with 10 μM of free CUR, CUR.SA, CUR-NPs, CUR.SA-NPs, the surface morphology changed into spherical shape and cytoplasmic shrinkage was observed. Cell detachment and cells departure from each other was also observed dramatically upon treatment with 25 μM of free CUR, CUR.SA, CUR-NPs, and CUR.SA-NPs. In the case of HCT116 cells, a similar profile was also observed upon increasing concentrations of treatments compared to untreated cells (Figure 50).

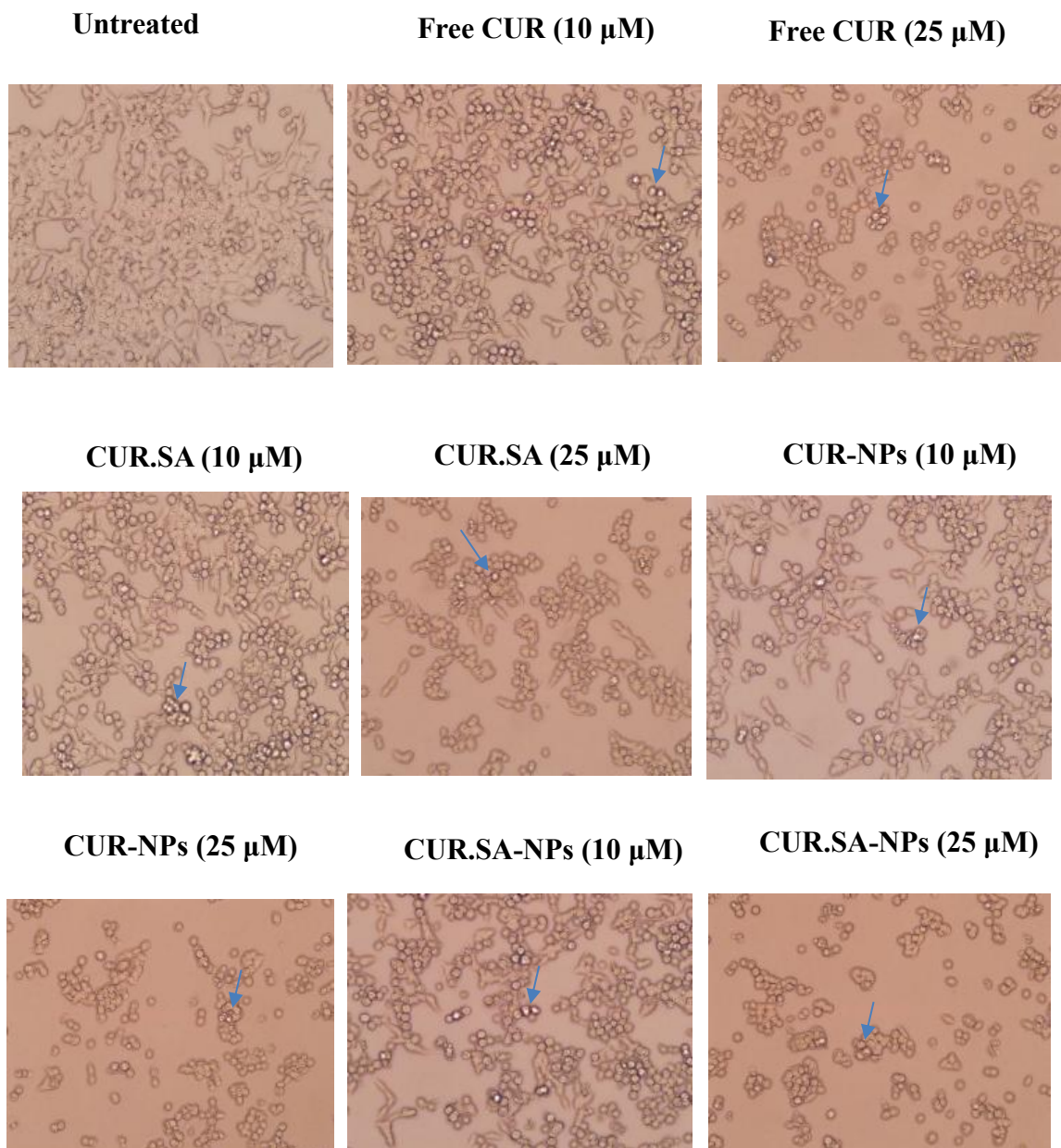


Figure 49. Representative microscopic images of live and dead cells showing morphological changes in SW480 cells after different treatments for 24 hours. Morphological features were observed under an inverted microscope with objective lens x20. Arrows indicate that rounded cells resulted from abnormal morphological changes and cytoplasmic shrinkage with increasing concentration of treatments.

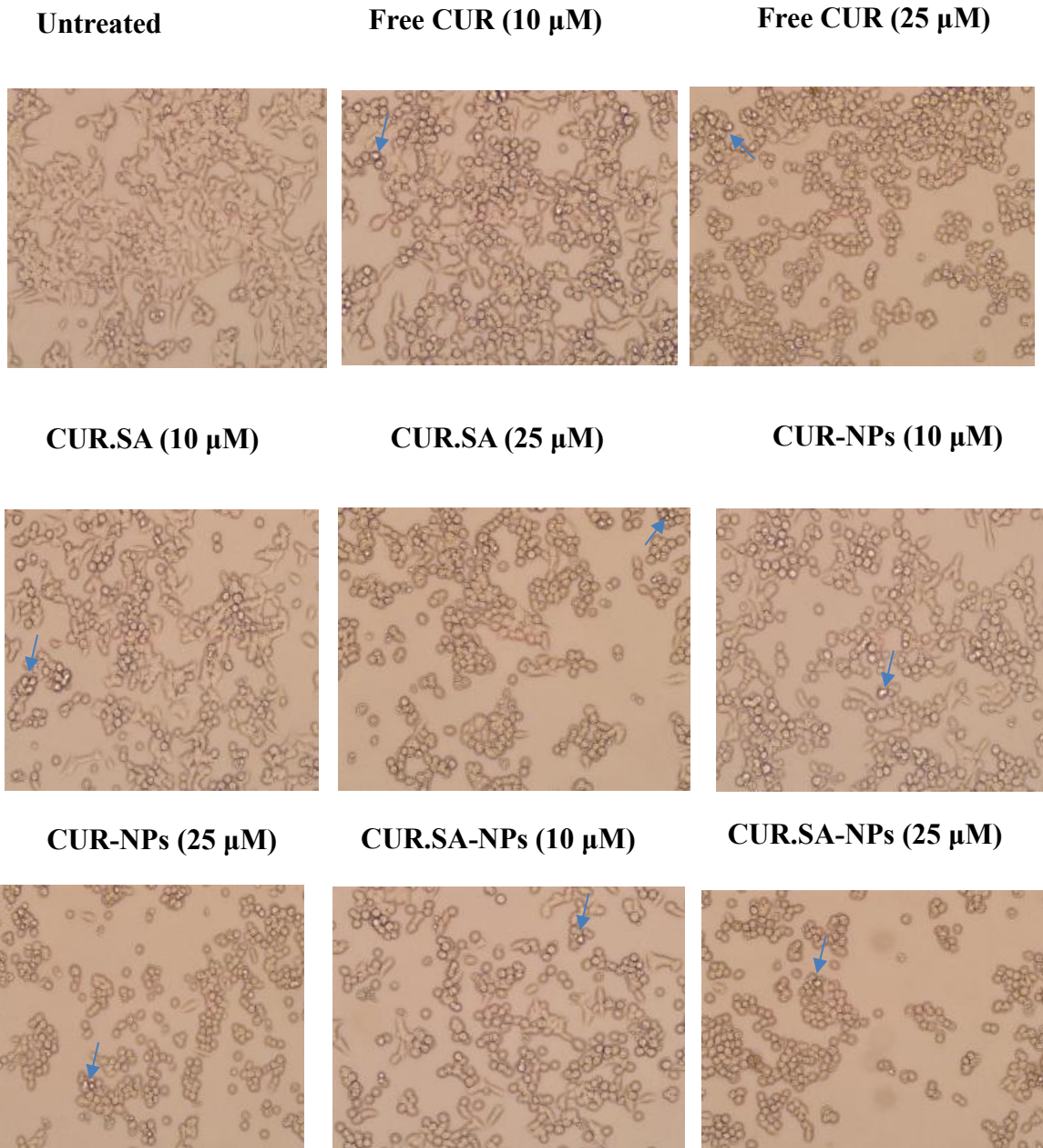


Figure 50. Representative microscope images of live and dead cells showing morphological changes in HCT116 cells after different treatments for 24 hours. Morphological features were observed under an inverted microscope with objective lens x20. Arrows indicate the rounded cells resulted from abnormal morphological changes and cytoplasmic shrinkage with increasing concentration of treatments.

3.4.4 Cell cycle

Cell cycle analyses was conducted to investigate the effects of CUR-NPs and CUR.SA-NPs on SW480 and HCT116 cell proliferation. The cellular distribution in different phases of the cell cycle were obtained by analyzing the DNA content of cells using flow cytometry. The results are presented as cellular DNA content frequency histograms (Figure 51 and 52).

In the case of SW480 cell line, Figure 51 clearly showed that both 10 μ M and 25 μ M of CUR-NPs and CUR.SA-NPs have altered the distribution of SW480 cells in the cell cycle phases significantly. Compared to untreated cells, an increased number of cells in G2/M phase was observed after treating cells with 10 μ M and 25 μ M CUR-NPs by $27.40 \pm 1.13\%$ and $48.53 \pm 1.06\%$, respectively, compared to untreated cells ($25.10 \pm 0.84\%$), which confirms induction of cell arrest at the G2/M phase. This change was followed by a drop of number of cells in the G0/G1 phase ($57.15 \pm 0.21\%$ at 10 μ M, and $31.10 \pm 0.98\%$ at 25 μ M) and decreases in S phase ($6.79 \pm 0.22\%$ at 10 μ M, and $12.09 \pm 0.01\%$ at 25 μ M) compared to untreated cells. A similar profile in G2/M phase was also observed after treatment using with 10 μ M and 25 μ M CUR.SA-NPs ($27.05 \pm 0.49\%$ and $48.40 \pm 3.25\%$, respectively). This change was followed by decreases in G0/G1 phase ($58.65 \pm 0.91\%$ at 10 μ M, and $30.35 \pm 2.05\%$ at 25 μ M) and decreases in S phase ($6.37 \pm 0.19\%$ at 10 μ M, and $11.05 \pm 1.20\%$ at 25 μ M) compared to untreated cells.

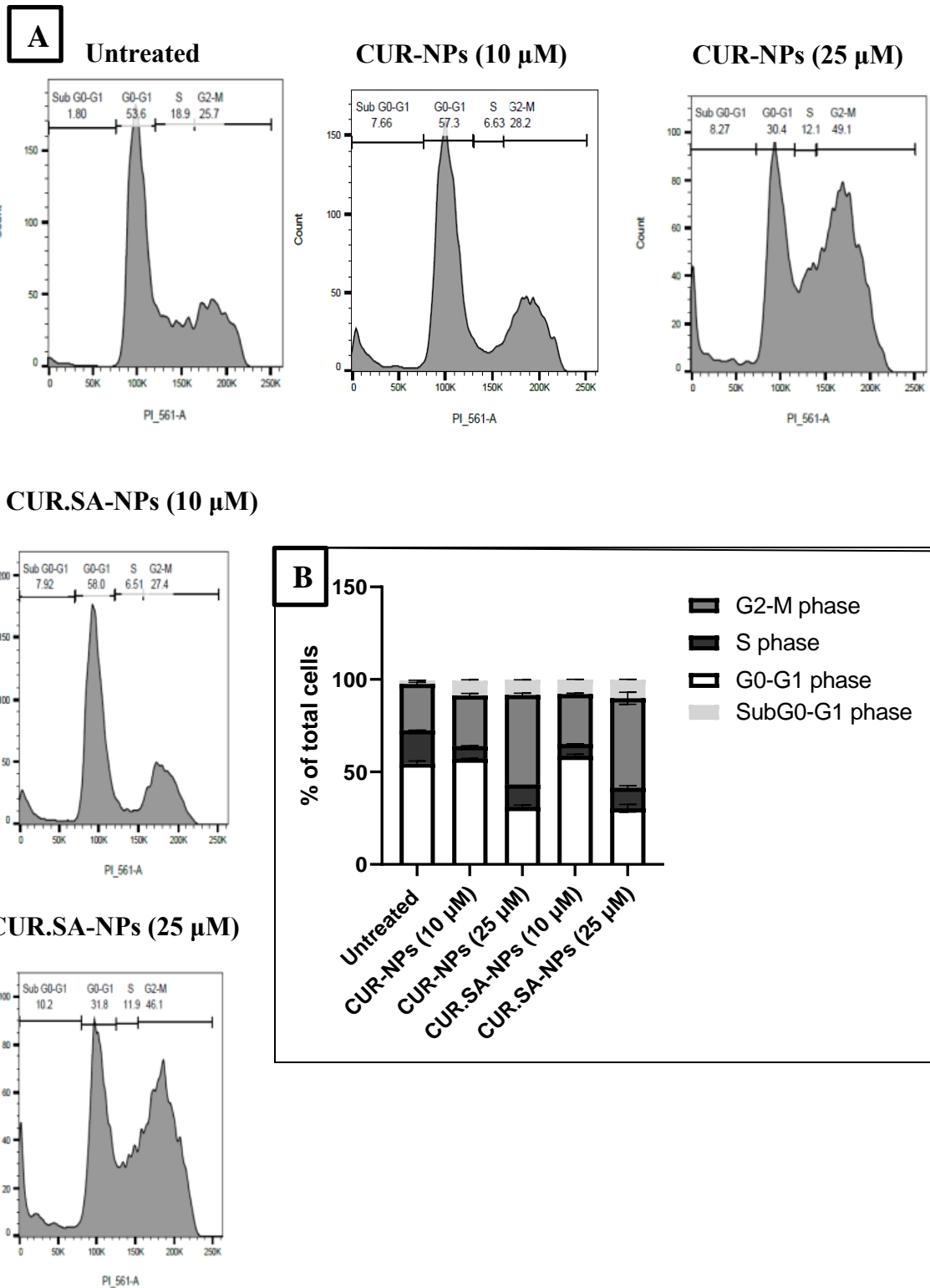


Figure 51. Cell cycle analysis of SW480 cells after treatment with CUR-NPs (10 and 25 μ M), CUR.SA-NPs (10 and 25 μ M), and untreated cells for 24 hours. Characteristic histogram data of Annexin V-FITC/PI flow cytometer evaluation (A) and cell cycle distribution percentages (B) are represented. Results are expressed as percentage of total cells mean \pm SD (n=3).

In the case of HCT116 cell line, Figure 52 has evidently demonstrated that both 10 μM and 25 μM of CUR-NPs and CUR.SA-NPs have significantly altered the distribution of HCT116 cells in the cell cycle phases. The obtained results revealed that the HCT116 cells were arrested in the G2/M phase. Increased number of cells in G2/M phase was observed after treating cells with 10 μM and 25 μM CUR-NPs by $49.90 \pm 0.42\%$ and $52.90 \pm 1.69\%$, respectively, compared to untreated cells ($25.45\% \pm 0.63$). This change was followed by drops in G0/G1 phase ($37.60 \pm 0.56\%$ at 10 μM , and $31.80 \pm 0.42\%$ at 25 μM) and declines in S phase ($5.23 \pm 0.17\%$ at 10 μM , and $11.40 \pm 0.55\%$ at 25 μM) compared to untreated cells. A similar profile in G2/M phase was observed also after treatment with 10 μM and 25 μM CUR.SA-NPs ($48.75 \pm 0.63\%$ and $53.40 \pm 0.28\%$, respectively). This change was followed by decreases in G0/G1 phase ($36.85 \pm 0.35\%$ at 10 μM , and $33.15 \pm 0.21\%$ at 25 μM) and decreases in S phase ($6.78 \pm 0.89\%$ at 10 μM , and $9.39 \pm 0.38\%$ at 25 μM) compared to untreated cells.

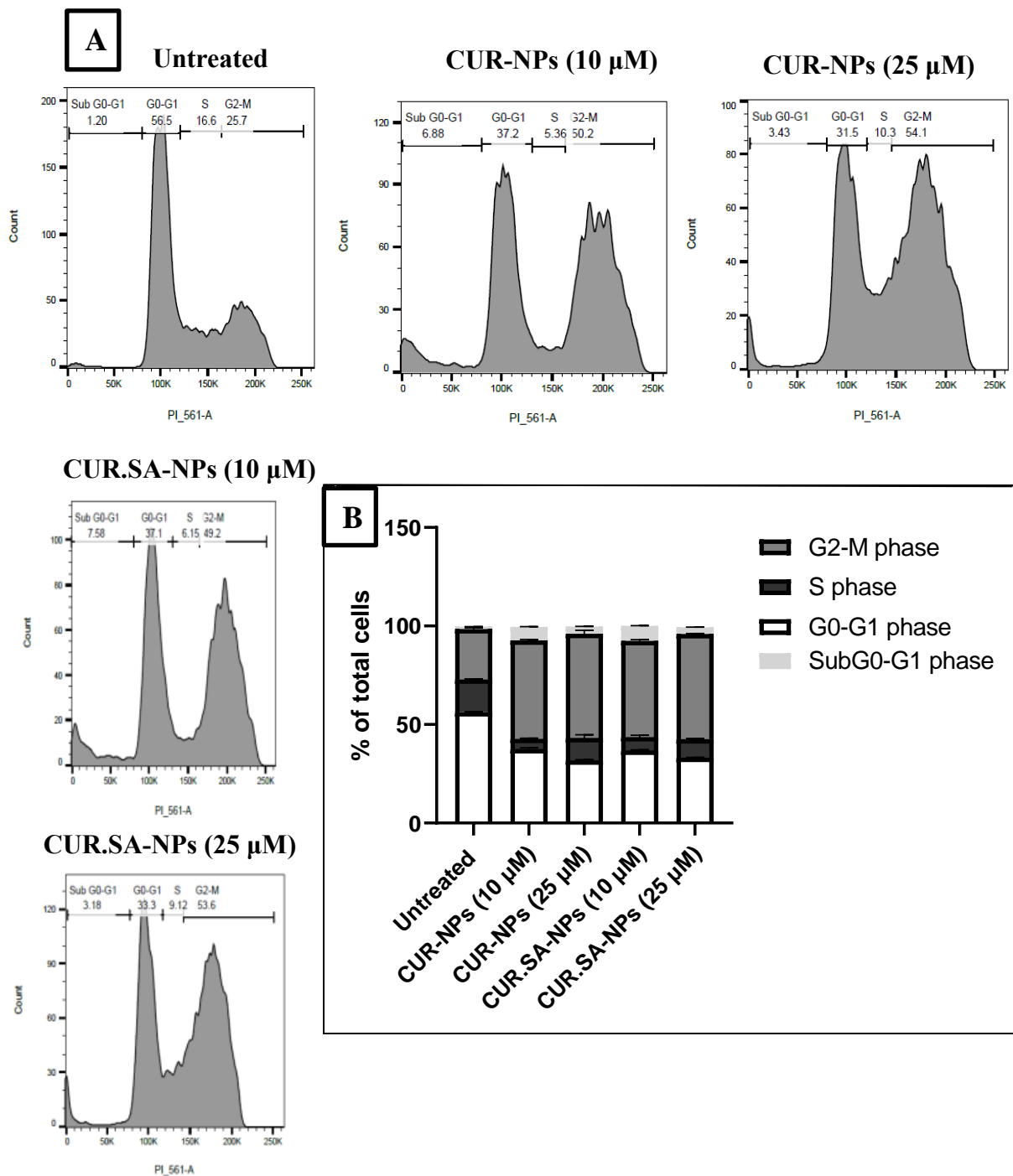


Figure 52. Cell Cycle analysis of HCT116 cells after treatment with CUR-NPs (10 and 25 μ M), CUR.SA-NPs (10 and 25 μ M), and untreated cells for 24 hours. Characteristic histogram data of Annexin V-FITC/PI flow cytometer evaluation(A) and cell cycle distribution percentages (B) are represented. Results are expressed as percentage of total cells mean \pm SD (n=3).

3.4.5 Cell apoptosis

The apoptotic cell death was evaluated upon treating SW480 (Figure 53.A) and HCT116 (Figure 54.A) cell lines with CUR-NPs (10 and 25 μ M), CUR.SA-NPs (10 and 25 μ M), and untreated cells as control using Annexin V flow-cytometric assay. Both cell lines were treated for 24 hours, and cells at early apoptosis and late apoptosis phases were calculated.

In case of SW480 cell line (Figure 53.B), population portion of total apoptotic cells was (i) $5.03 \pm 1.06\%$ for untreated cells, (ii) $25.98 \pm 0.08\%$ for CUR-NPs (10 μ M) group; (iii) $67.35 \pm 3.18\%$ for CUR-NPs (25 μ M) group; (iv) $15.35 \pm 0.93\%$ for CUR.SA-NPs (10 μ M) group, and (v) $66.85 \pm 0.63\%$ CUR.SA-NPs (25 μ M).

In the case of HCT116 cell line (Figure 54.B), the population portion of total apoptotic cells was (i) $8.94 \pm 0.22\%$ for untreated cells, (ii) $42.15 \pm 5.32\%$ for CUR-NPs (10 μ M) group; (iii) $95.20 \pm 0.98\%$ for CUR-NPs (25 μ M) group; (iv) $49.35 \pm 0.85\%$ for CUR.SA-NPs (10 μ M) group, and (v) $92.48 \pm 0.25\%$ for CUR.SA-NPs (25 μ M). In both cell lines, the total apoptotic rate of CUR-NPs (10 μ M and 25 μ M) and CUR.SA-NPs (10 μ M and 25 μ M) groups was significantly different from that of untreated group ($p < 0.05$). Thus, both CUR-NPs (25 μ M) and CUR.SA-NPs (25 μ M) have stimulated apoptosis of the both cell lines in a dose-dependent manner ($p < 0.05$), and the ability of CUR-NPs (25 μ M) to induce the apoptosis of SW480 cells was comparable to that of CUR.SA-NPs (25 μ M).

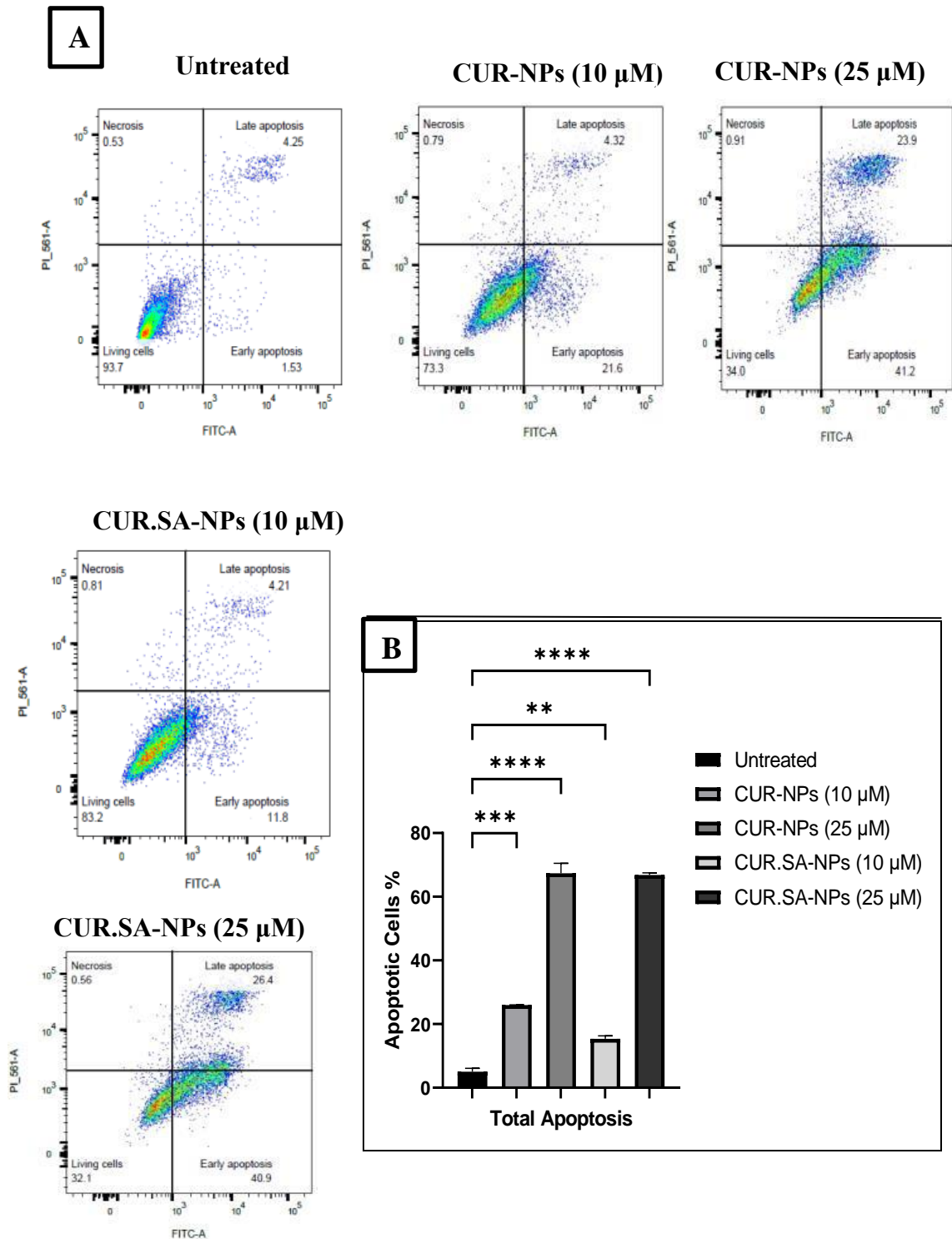


Figure 53. Apoptotic cell death of SW480 cells after treatment with CUR-NPs (10 and 25 μM), CUR.SA-NPs (10 and 25 μM), and untreated cells for 24 hours. (A) Characteristic histogram data of Annexin V-FITC/PI flow cytometer evaluation, and (B) Total apoptotic cell percentages are represented as mean ±SD (n=3). Statistical significance was calculated using 1-way ANOVA and Dunnett's test (ns: not significant; (*p < 0.05, **p < 0.01; ***p < 0.001, ****p < 0.0001 indicates statistical significance).

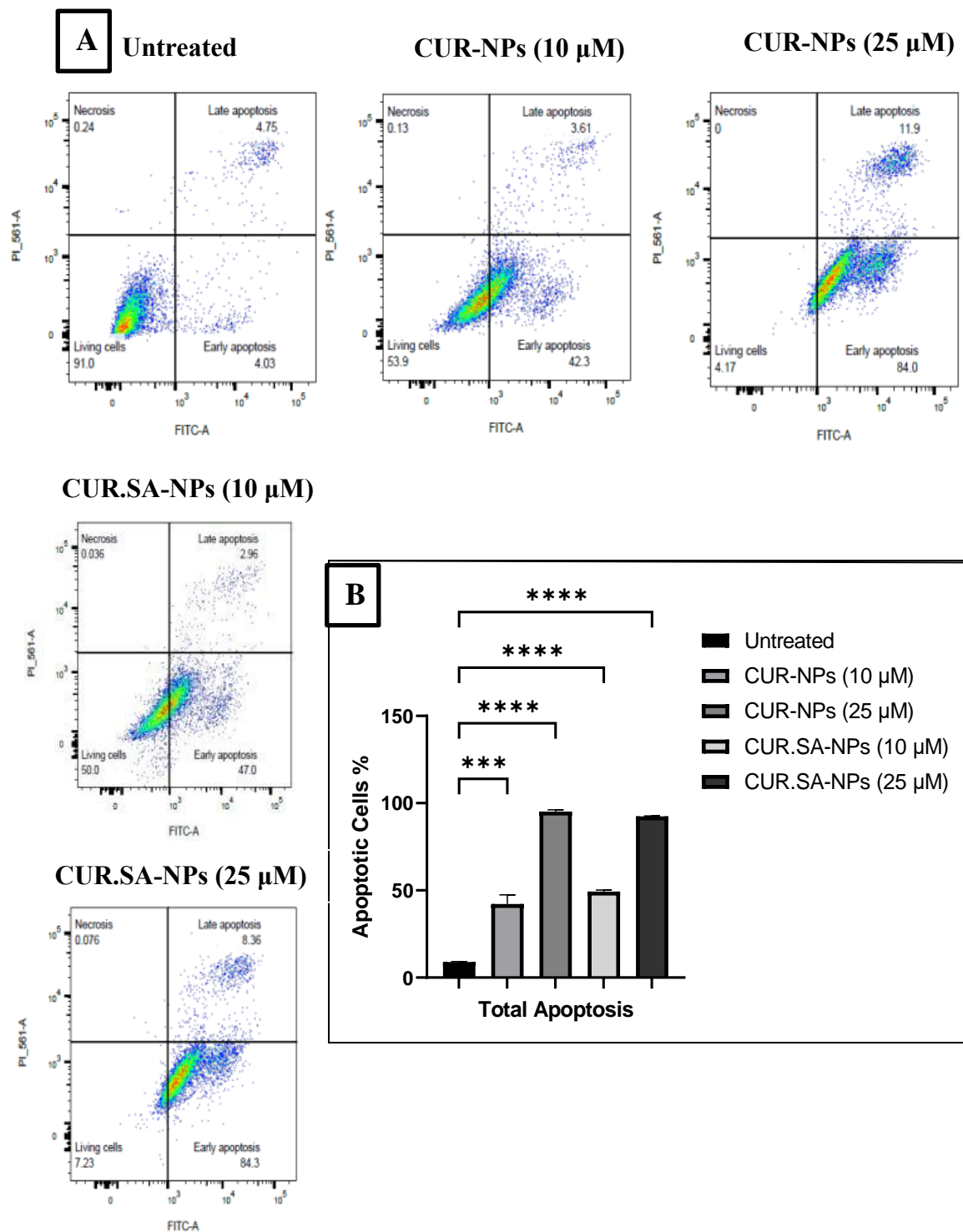


Figure 54. Apoptotic cell death of HCT116 cells after treatment with CUR-NPs (10 and 25 μ M), CUR.SA-NPs (10 and 25 μ M), and untreated cells for 24 hours. (A) Characteristic histogram data of Annexin V-FITC/PI flow cytometer evaluation, and (B) Total apoptotic cell percentages are represented as mean \pm SD (n=3). Statistical significance was calculated using 1-way ANOVA and Dunnett's test (ns: not significant; (*p < 0.05, **p < 0.01; ***p < 0.001, ****p < 0.0001 indicates statistical significance).

3.4.6 Western Blotting

To assess CUR-NPs and CUR.SA-NPs effect on the total PARP and cleaved caspase 8, which are proapoptotic markers in SW480 and HCT116 cells, Western blotting was used (Figure 55). In SW480 cell line, upon treatment with 25 μM of CUR-NPs and CUR.SA-NPs for 24 hours, a significant dose-dependent increase ($P < 0.05$) in PARP and cleaved caspase 8 expression was observed compared to untreated cells (Figure 56). In the case of HCT116 cell line, a similar profile was also observed upon treatment with 25 μM of CUR-NPs and CUR.SA-NPs for 24 hours compared to untreated cells (Figure 56). Thus, overexpression of these apoptotic markers has confirmed the induction of apoptosis in both cell lines upon treatment with CUR-NPs and CUR.SA-NPs.

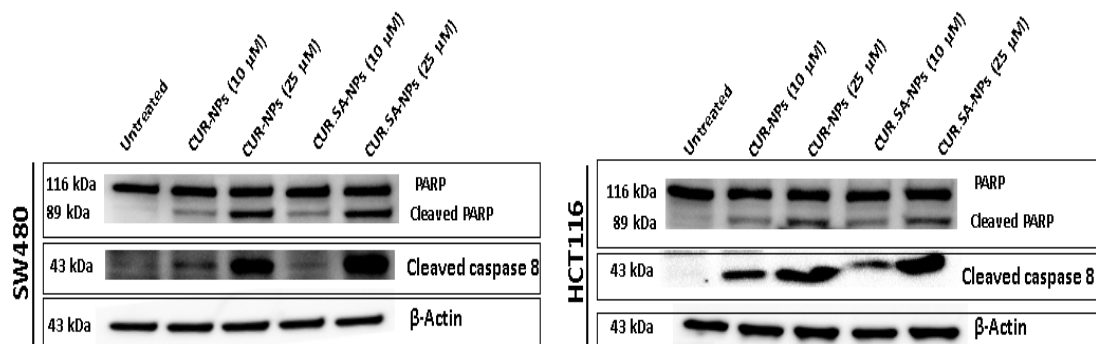


Figure 55. Western blot bands of Total PARP and Cleaved Caspase 8 in SW480 and HCT116 cell lines. Increased expression of both Total PARP and Cleaved Caspase 8 was noticed after treatment using CUR-NPs (10 and 25 μM), CUR.SA-NPs (10 and 25 μM), and untreated cells for 24 hours.

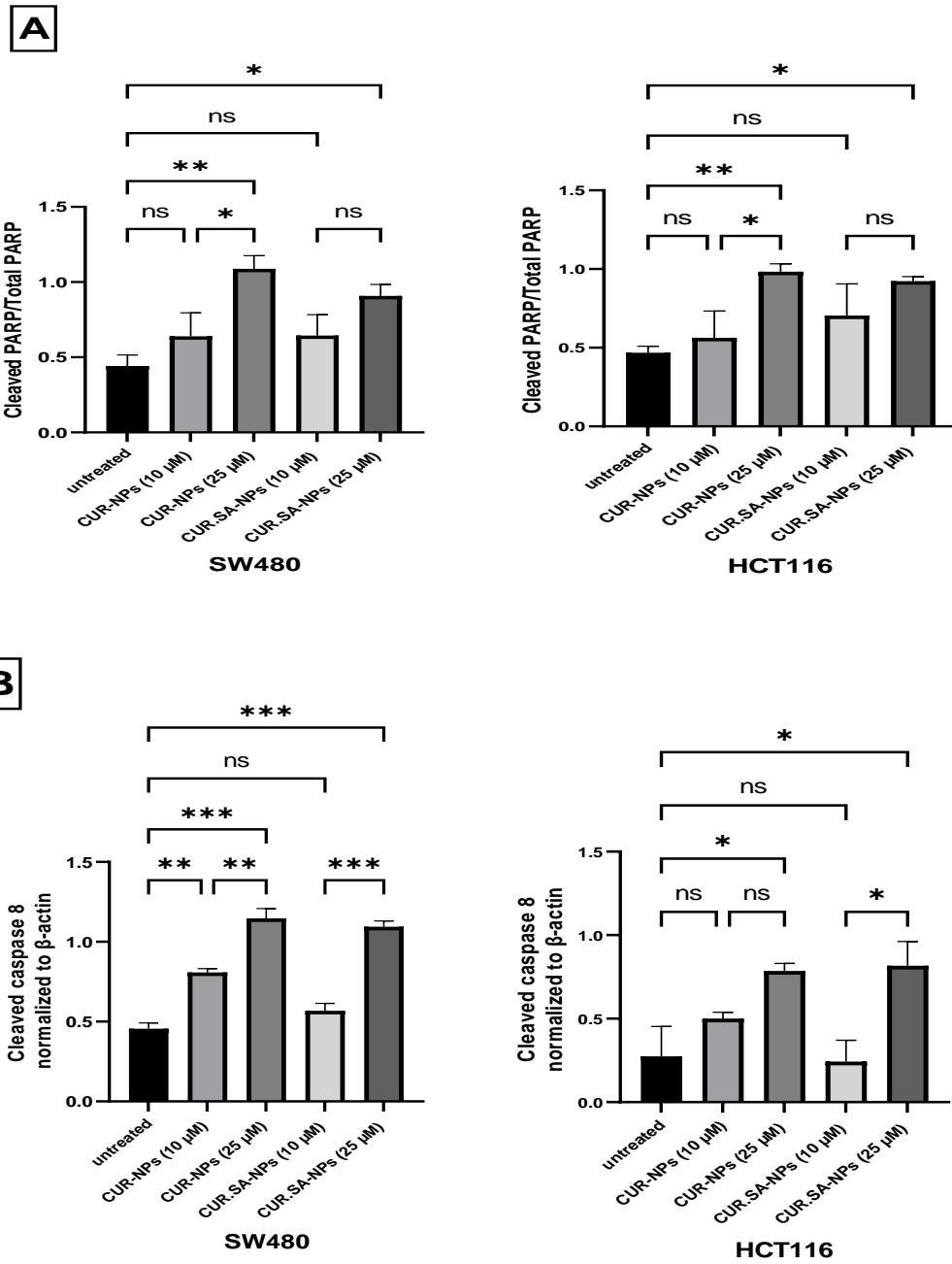


Figure 56. Quantification results as average density to β -actin of total PARP (A) and cleaved caspase 8 (B). All statistical results are represented as the mean \pm SD (n=3). Statistical significance was calculated using 1-way ANOVA and Bonferroni test (ns: not significant; (* $p < 0.05$, ** $p < 0.01$; *** $p < 0.001$, **** $p < 0.0001$ indicates statistical significance).

CHAPTER 4: DISCUSSION

From the results and based on the literature, there is clear evidence to the anti-CRC activity of CUR. However as eluded to earlier, its full therapeutic potential is limited mainly by its low solubility and rapid metabolism (8). It is possible to encapsulate poorly soluble drugs in nanocarriers such as polymeric nanoparticles, whereby the physicochemical property of the former is masked in favor of improved solubility, biocompatibility and therapeutic activity. This has been shown in the present study and elsewhere (191). In the present study, CUR-NPs and CUR.SA-NPs were successfully formulated using a modified ionic gelation procedure (184). The success of the method was judged based on homogeneity of the formulation in low PDI values.

Physicochemical characterization using FT-IR, ^1H and ^{13}C NMR analysis was used to obtain a qualitative and quantitative assessment of the different functional groups present. The formation of CM conjugate is supported by data in the literature (181,192,193), and for CUR.SA conjugate, (94). After encapsulation in the mannosylated CS carrier system, the presence of both CUR and CUR.SA within the nanoparticle was corroborated by FT-IR data. Similar studies involving the conjugation of CUR.SA in CS nanoparticles provide support for the evidence of encapsulation of the conjugates within the nanoparticles (89, 183). However, the functionality of the formulation rest heavily on the cargo. It is therefore imperative to ascertain the physicochemical properties of the conjugates to assure that the two key constraints (solubility and stability) associated with CUR have been addressed.

The application of CUR in therapy is significantly limited because of its poor aqueous solubility (191). It is thus crucial that some form of intervention is imposed in order to realize the full therapeutic potential of CUR. In the present work, CUR succinylation was conducted to improve its aqueous solubility. The resultant conjugate

CUR.SA demonstrated improved solubility in aqueous media, compared to CUR, ($p < 0.05$). In ethanolic media, CUR showed better solubility compared to CUR.SA, ($p < 0.05$). Thermal stability assessment indicates that the degradation of both CUR and CUR.SA was insignificant in dark and room light ($p > 0.05$) after 6 hours of exposure. On the other hand, both CUR and CUR.SA exhibited a significant degradation profile after exposure to sunlight ($p < 0.05$). The other key parameter studied was the solubility, whereby we conclude that CUR succinylation indeed improved the solubility of CUR in comparison with free CUR, with conserved stability. The improved solubility is attributable to the succinic acid moieties, which are hydrophilic. In summary, overcoming these physicochemical constraints are likely to impact positively the therapeutic outcomes, and thus the cell uptake and anti CRC effect will be discussed accordingly in subsequent sections (222).

In this work, ionic gelation method was used in formulating the different nanoparticles using STPP as a cross-linker. Because of its excellent crosslinking functionality and nontoxicity, STPP has been widely used to formulate CS nanoparticles (194,195). Ionic gelation is based on the ionic crosslinking between CS amino groups, that are positively charged, and negatively charged polyanions from STPP (195). Although medium MW CS was used in the present study, the obtained particle size of CUR-NPs and CUR.SA-NPs were 268 nm and 342 nm, respectively, which is slightly higher than a reported study using CUR- loaded mannosylated CS nanoparticles with size ranges between 172 nm (192) to 215 nm (181), when low MW CS was used. Furthermore, medium MW CS was, previously, used to encapsulate CUR, but large microparticulate formulation was obtained (196). The higher particle size of CUR and CUR.SA compared to empty CM-NPs is due to the entrapment of CUR and CUR.SA within the CM carrier, which is an indirect indication of encapsulation. The

particle size plays a major role in the deployment of the cargo to the site of action, whereby previous studies have indicated that sizes between 10 nm to 200 nm are more enabled to reach the tumor sites (197). In other words, smaller nanoparticles (up to 300 nm) were more likely to enter the cells through endocytosis or diffusion, and larger nanoparticles would be imported into cancer cells through phagocytosis (198,199). The reduced zeta potential in CUR-NPs and CUR.SA-NPs could be attributed to the occupation of free NH₂ groups present in CS with mannose and CUR/CUR.SA conjugate. A similar observation was made when CS was conjugated with mannose as reported previously by where a reduction in zeta potential was also observed (183,192).

Among the formulations studied in the present work, Formulation B yielded the most optimal size and zeta potential, whilst the other formulations were either microparticulate or presented with an almost neutral zeta potential. The size and shape of the optimized formulation was further confirmed by the SEM and AFM analyses. The SEM revealed a spherical morphology of the particles that were discrete, an indication that sufficient surface charge was manifested between the particles. The AFM presented a somewhat rough surface with the shape and size in agreement with the SEM and DLS analysis, respectively. Such sphericity of CS nanoparticles has been also reported in the literature (181,200,201). However, the discreteness was not always associated with the sphericity.

It is important to ascertain the distribution of the active drug within the nanoparticles. The EDX analysis revealed the presence of sodium and phosphorus on the surface of the nanoparticles. It was not possible to ascertain the localization of CUR because elemental C, H and O are common to the other components used in the nanoparticle formulation. However, it is likely that CUR is present within the matrix of the nanoparticle based on a similar observations in the literature (89,202).

The loading capacities of both CUR and CUR-SA within the CM carrier were affected by the STPP and CS ratios. Low amounts of CM and STPP resulted in low %EE because of the low matrix density, which favors poor retention of the cargo (192). Results from the current study did not show a significant difference in %EE between the formulations prepared with different CM:STPP ratios, which were all above 90%, except Formulation D, that yielded %EE of 34.94% and 38.4% for CUR and CUR.SA, respectively. The obtained data is supported by previous studies where the obtained %EE ranged between 70 and 98% (192,203,204).

Drug release studies from the nanoparticles gives us some sense of how much of the cargo is retained within prior to cellular uptake. The release of both CUR and CUR.SA showed a burst release of up to around 30% at pH 6.8 within 6 hours from both CUR-NPs and CUR.SA-NPs followed by a levelling off until 72 hours. This is indicative of significant degree of retention of the cargo within the carrier and relevant in the current endeavor because a high drug retention will ensure high drug deployment after uptake by cells. In the case of acidic pH condition, an increase in CUR release was observed in CUR-NPs up to 2 hours, however the profile for CUR.SA was slightly different, with a peak at 1 hour followed by a fall at 2 hours. The maximum amount released in both cases was about 30%. CS hydrates in acidic media, which promotes drug release, and is the reason for the observed 30% release, even though the solubility of CUR in acidic media is low. In contrast, CS is insoluble at neutral to alkaline pH but the solubility of CUR is higher at elevated pH. It is known that the cancer media has an acidic pH compared to healthy cells (205), therefore, an accelerated release of CUR or CUR.SA is expected in the tumor sites, which could demonstrate a potential cancer therapy. Moreover, the slow-release profile is useful for long-term treatment, which is characteristic of cancer therapy (207). This is likely to improve patient compliance and

quality of life. In addition, extended-release profile of drugs represents a recent and attractive medicinal approach for cancer treatment as it could have a potential effect on cancer treatment with reduced number of received doses and unwanted side effects (206). Furthermore, since none of the formulations released 100% of the cargo over 72 hours, it suggests a significant degree of the drug retention within the CM carrier. Similar observations of slow CUR release have been reported in previous studies (207,208). In summary the slow release of CUR-NPs and CUR.SA-NPs could be a potential alternative for cancer therapy, and CM is considered an effective controlled drug delivery carrier.

CUR is crystalline, which is one of the reasons for its insolubility in aqueous media. It is often necessary to assess the crystalline characteristics of active pharmaceutical ingredient (API) after formulation since polymeric transformations are likely. In the present study, XRD was used to determine the degree of crystallinity of free CUR and CUR.SA, which reaffirmed the crystallinity of CUR. However, after conjugation to SA, the sharp peaks ascribable to CUR disappeared, which indicates that CUR.SA is less crystalline than CUR. Indeed, solubility studies confirms this observation, whereby the CUR.SA presented a better solubility than CUR in aqueous media. Further characterization of CUR-NPs and CUR.SA-NPs revealed amorphous profiles for both formulations, suggesting that polymorphic transformation to amorphous states occurs during the formulation. The reduced crystallinity reflects an improved dissolution rate due to an increase in the lattice free energy (209); hence, it is anticipated that the bioavailability of the low-crystallinity molecules would be higher than that of higher-crystallinity molecules. Thus, the results evidenced that CUR and CUR.SA would possess an enhanced bioavailability after their encapsulation inside CM carrier. The obtained data is supported by previous studies where a reduction in

crystallinity phase was also reported after CUR encapsulation inside CS polymeric carrier (210–212).

Understanding the thermal profile of formulations can make deeper insights into the behavior of polymeric carriers as a function of temperature (213). In this work, CUR succinylation and CS mannosylation revealed a stable profile of the conjugates compared to free compounds. Compared to empty CM-NPs, CUR-NPs and CUR.SA-NPs possessed a more stable thermal profile whereby the carrier system can be said to provide thermal stability to CUR and CUR.SA within the CM nanoparticle. Such thermal stability provision by CS has also been observed previously (214,215).

In vitro stability of nanoparticles in the culturing media is a key factor for the efficient delivery of the carried drug. The nanoparticles should be stable long enough to be able to release the carried cargo in the targeted site through strong protection of the drug cargo. After their incubation under standard cell growth conditions, the prepared formulations have maintained their spherical shape in the serum supplemented RPMI and DMEM medias for up to 48 hours. A similar profile was previously observed for CS-NPs that were stable and retained their spherical morphology after incubation in cellular media for 72 hours (216). Thus, stable nanoparticles will ensure the potential release of the cargo in the targeted cellular region. The nanoparticle aggregation is sometimes unavoidable under standard culturing conditions. As a useful solution, it was proposed by Ozturk et al. that removing the nanoparticles after a sufficient incubation period and adequate cellular uptake is considered a feasible and low-cost method for testing their *in vitro* effectiveness and to avoid their aggregation (217).

Storage is a key stability-indicating parameter and changes in physical properties during storage can be used to ascertain the stability of the formulation as a function of time. During storing the nanoformulation, variations in the size distribution,

zeta potential, and PDI could take place and the nanoparticles become aggregated. In this study, the size, zeta potential, and PDI were not obviously changed after storage at 4°C for 28 days and at 37°C for 3 weeks, which confirms that the prepared nanoparticles are very stable. Similarly in a previous work, the mean diameter and zeta potential of the saponin-coated CUR nanoparticles revealed a slight change only when they were stored at 4°C in aqueous suspensions (218). Furthermore, Davis et al. have developed a novel Pluronic-F127 stabilized D- α -Tocopherol polyethene glycol1000 succinate nanoparticles containing CUR and possessed a stable particle size for 9 weeks when stored at 25°C in liquid and lyophilized forms (219). Similarly, formulated CUR containing CS-g-Pluronic nanoparticles showed no statistically significant variations in particle size and PDI after 24 weeks of storage at 4°C (220).

Poor bioavailability of CUR following oral administration is the major constraint limiting the effectiveness of CUR as an effective anticancer agent. Nanoformulation and or chemical modification of CUR appears to be making some headway in circumventing this constraint. In addition, targeted nanoencapsulation of CUR is also expected to enhance its bioavailability as well as improved cytotoxic effect against CRC cells (129). It is important to ascertain the toxicity effect imposed by the carrier system as well. In the present study, two cell lines were studied (HCT116 and SW480), whereby, a minor reduction in the cell viability (less than 10%) of cells treated with CM-NPs and DMSO was observed, which confirms that CM-NPs and DMSO exhibit no toxicity to the cells. However, a decrease in cell viability was observed by CUR and CUR.SA loaded nanoparticles. This is in agreement with a previous work by Ma et al. that showed there was no cytotoxic effect associated CS-NPs uptake by the CRC cells (221). Data from the present study demonstrated that both CUR-NPs and CUR.SA-NPs had significantly reduced viability of HCT116 and SW480 cells when

treated with concentration range 1–25 μM . Moreover, CUR- NPs decreased the cell viability of both cell lines as potently as CUR.SA-NPs in a time- and dose-dependent way. The significant differences between the two treatment groups on 24 hours and 48 hours of CUR and CUR.SA entrapment inside CM-NPs were noticed. These observations indicated that entrapment of CUR or CUR.SA within the CM carrier did not alter the therapeutic activity of either. Furthermore, the prepared nanoparticles could induce a prolonged contact between the nanoparticles and the CRC cells, which was beyond confirmed through the low IC_{50} values for toxicity on SW480 and HCT116. In a recent study, Ma et al. has proved that CUR-loaded CS-NPs exhibited higher cytotoxic activity against CRC cells (HT29) compared to free CUR (221). Moreover, Orasitthiyanukarn et al. developed CS-alginate nanoparticles containing CUR diethyl disuccinate that showed an enhanced anticancer effect compared to free CUR (222).

Flow cytometry was performed to investigate the effects of CUR-NPs and CUR.SA-NPs on SW480 and HCT116 cell proliferation using PI staining of the nuclei to assess their cell cycle. Generally, the amount of the absorbed PI is proportional to the quantity of DNA present. Therefore, the fluorescence data would be correlated with the DNA quantity (223). In this work, both CUR-NPs and CUR.SA-NPs were found to induce cell accumulation in the G2/M phase, confirming that CUR and CUR.SA hinder cellular proliferation in SW480 and HCT116 cells. Usually, the induction of G2/M phase arrest is coupled with increased apoptosis, and is considered a marker of cytotoxic effect against cancer cells (224). In a recent study, similar outcomes were obtained where cetuximab-conjugated modified citrus pectin-chitosan nanoparticles entrapping CUR (Cet-MCPCNPs) stimulated cellular death in Caco-2 cells through inducing cell cycle arrest in the G2/M phase (225). In another study, a 75 μM dose of formulated mucoadhesive nanoparticles carrying CUR had induced cellular apoptosis

in colorectal cancer cells (HT-29), through induction of cell cycle arrest at G2/M phase after cellular treatment for 24 hours (226). Furthermore, CUR plays a role in stimulating degradation of membrane and DNA and in shrinking the cellular nucleus (227). Therefore, the observed morphological changes of SW480 and HCT116 cell lines after treatment by CUR-NPs and CUR.SA-NPs could be explained due to the encapsulated CUR and CUR.SA.

Induction of cellular apoptosis in different cancer cell lines was previously reported for CUR to take place through mitochondrial and receptor-mediated apoptotic pathways, where upregulation or downregulation of various apoptotic markers plays a key role (228). In the present work, induction of cellular apoptosis was observed in SW480 and HCT116 cell lines after treatment by CUR-NPs and CUR.SA-NPs. Further, apoptotic induction was confirmed using protein quantification by Western blotting where upregulation of total PARP and cleaved caspase 8 markers was confirmed. PARP refers to poly (ADP-ribose) polymerase, which is a nuclear enzyme that is cleaved into different fragments during apoptosis and it has become a beneficial feature to confirm apoptosis (229). Caspase 8 is a cysteine protease that initiates apoptotic signaling once it is activated (230). Thus, upregulation of total PARP and cleaved caspase 8 markers confirms cellular apoptotic induction. In this work, induction of cellular apoptosis was confirmed in SW480 and HCT116 cell lines after treatment by CUR-NPs and CUR.SA-NPs through upregulation of both total PARP and cleaved caspase 8 markers. In a previous study, a 20 μ M combination of CUR and 5-FU treatment has induced HCT116 apoptosis through potentiating the expression PARP and Cleaved caspase 8 (231). Identical biological activity was observed in the present work between CUR-NPs and CUR.SA-NPs and no statistical significance was recorded. Succinylation of CUR was found to improve CUR solubility, and thus, its bioavailability and cellular uptake by

CRC cell lines. This could be explained by the nature of in vitro tests that occurs in a controlled environment, where interaction between different organs does not take place. Thus, further investigation of CUR-NPs and CUR.SA-NPs as potential anti-CRC agents is required to translate their application towards in vivo studies.

CHAPTER 5: CONCLUSIONS AND FUTURE DIRECTIONS

Worldwide, colon cancer remains to be one of the major causes of mortality. Drugs originating from natural sources including curcumin have significantly contributed to drug discovery for cancer therapy. While curcumin exhibit potent anticancer activities, its low solubility, bioavailability and instability, hinders its therapeutic applications. In this work, CUR-NPs and CUR.SA-NPs were successfully formulated using ionic gelation method as proposed anti-cancer formulations. Formation of nanoparticles was confirmed using different characterization tools including XRD, DLS, and SEM. Further, In vitro drug release demonstrated a sustained release profile of CUR and CUR.SA from CM carrier over a period of 3 days. Moreover, CUR-NPs and CUR.SA-NPs illustrated an excellent cytotoxicity and intracellular uptake by CRC cell lines (SW480 and HCT116) compared to free CUR and CUR.SA conjugate. Certainly, cellular studies including cell apoptosis and cell cycle assays confirmed the anticancer efficiency of both CUR-NPs and CUR.SA-NPs against colorectal cancer cells (SW480 and HCT116). Thus, the promising results indicates CUR-NPs and CUR.SA-NPs as excellent agents for colon cancer therapy.

Further studies are planned to test the efficacy of CUR-NPs and CUR.SA-NPs against other colorectal cancer cells to gather more information about their effectiveness against a range of colorectal cancer cell lines with distinct gene expression. Furthermore, the toxicity of CUR-NPs and CUR.SA-NPs towards normal human cell line should be also tested to ensure that both formulations are non-toxic to normal cells. Besides, in vivo assessment of CUR-NPs and CUR.SA-NPs is required to better understand the anticancer behavior of the formulation. This should include pharmacokinetic comparison between the CUR.SA and CUR.

Study limitations

In this study, some obstacles have been encountered. For instance, some skills for instrumentation use such as HPLC and DLS were required. Furthermore, lack of some equipment tools, that were among the study plan, to be used for NPs characterization were either under maintenance or not available. Timeline was one of the barriers to accomplishment of this work due to delay of receipt of some chemicals. Adequate training for some study techniques was required, which was either through attending relevant workshops or through personal training sessions.

Some of the study limitations also includes that stability of nanocarriers is weakness that affects their potential applications for cancer therapy because nanoparticles are prone to aggregation and agglomeration, which could affect their cellular uptake and treatment outcomes. Also, there is a lack of regulations related to public awareness of nanotechnology application for cancer therapy and Only a few organizations have created regulations for regulating the use of nanotechnology for cancer therapy, and although a lot of work has been done in the literature using polymeric nanoparticles for cancer therapy, up to data, polymeric nanoparticles are not approved yet by the FDA as a new approach for cancer therapy. Although their application for cancer therapy is being commercialized, the affordability of the nanocarriers is a worry due to scale up preparation of the nanoparticles.

References

1. World Health Organization, International Agency for Research in Cancer. 2021; Available from: https://gco.iarc.fr/today/online-analysis-pie?v=2020&mode=cancer&mode_population=continents&population=900&populations=900&key=total&sex=0&cancer=39&type=0&statistic=5&prevalence=0&population_group=0&ages_group%5B%5D=0&ages_group%5B%5D=17&nb_items=7&group
2. Jahanafrooz Z, Mosafer J, Akbari M, Hashemzaei M, Mokhtarzadeh A, Baradaran B. Colon cancer therapy by focusing on colon cancer stem cells and their tumor microenvironment. *J Cell Physiol.* 2020;235(5):4153–66.
3. Aiello P, Sharghi M, Mansourkhani SM, Ardekan AP, Jouybari L, Daraei N, et al. Medicinal plants in the prevention and treatment of colon cancer. *Oxid Med Cell Longev.* 2019;2019:53.
4. Kim JH. Chemotherapy for colorectal cancer in the elderly. *World J Gastroenterol.* 2015;21(17):5158–66.
5. Ding L, Ma S, Lou H, Sun L, Ji M. Synthesis and biological evaluation of curcumin derivatives with water-soluble groups as potential antitumor agents: An in vitro investigation using tumor cell lines. *Molecules.* 2015;20(12):21501–14.
6. Baskaran R, Madheswaran T, Sundaramoorthy P, Kim HM, Yoo BK. Entrapment of curcumin into monoolein-based liquid crystalline nanoparticle dispersion for enhancement of stability and anticancer activity. *Int J Nanomedicine.* 2014;9(1):3119–30.
7. Saranya TS, Rajan VK, Biswas R, Jayakumar R, Sathianarayanan S. Synthesis, characterisation and biomedical applications of curcumin conjugated chitosan

- microspheres. *Int J Biol Macromol*. 2018;110:227–33.
8. Mbese Z, Khwaza V, Aderibigbe BA. Curcumin and Its Derivatives as Potential Therapeutic Agents in Prostate, Colon and Breast Cancers. *Molecules*. 2019;24(23).
 9. Yen P, Fadhilzil M, Mohd F, Rullah K, Wai K. Insights on the synthesis of asymmetric curcumin derivatives and their biological activities. *Eur J Med Chem*. 2019;183:111704.
 10. Zheng B, McClements DJ. Formulation of More Efficient Curcumin Delivery Systems Using Colloid Science: Enhanced Solubility, and Bioavailability. *Molecules*. 2020;1–25.
 11. Wong KE, Ngai SC, Chan KG, Lee LH, Goh BH, Chuah LH. Curcumin nanoformulations for colorectal cancer: A review. *Front Pharmacol*. 2019;10.
 12. Mahadevan V. Anatomy of the caecum, appendix and colon. *Surg (United Kingdom)* [Internet]. 2020;38(1):1–6. Available from: <https://doi.org/10.1016/j.mpsur.2019.10.017>
 13. Arévalo-Pérez R, Maderuelo C, Lanao JM. Recent advances in colon drug delivery systems. *J Control Release*. 2020;327:703–24.
 14. Moran BJ, Jackson AA. Function of the human colon. *Br J Surg*. 1992;79(11):1132–7.
 15. Van den Mooter G. Colon drug delivery. *Expert Opin Drug Deliv*. 2006;3(1):111–25.
 16. Irving MH, Catchpole B. Anatomy and physiology of the colon, rectum, and anus. *Br Med J*. 1992;304(6834):1106–8.
 17. Hagihara PF, Griffen WO. Physiology of the colon and rectum. *Surg Clin North Am*. 1972;52(4):797–805.

18. Amidon S, Brown JE, Dave VS. Colon-Targeted Oral Drug Delivery Systems: Design Trends and Approaches. *AAPS PharmSciTech*. 2015;16(4):731–41.
19. Bray F et al. Global cancer statistics 2018: GLOBOCAN estimates of incidence and mortality worldwide for 36 cancers in 185 countries. *CA Cancer J Clin*. 2018;68:394–424.
20. World Health Organization. Cancer. 2021; Available from: <https://www.who.int/news-room/fact-sheets/detail/cancer>
21. THANI KBT AL. Cancer survival rate in Qatar one of the highest, data show. *The Peninsula*. 2021.
22. Weitz J., Koch M., Debus J., Höhler T., Galle R. BM. Colorectal cancer. *Lancet*. 2005;394:1467–80.
23. Labianca R, Beretta GD, Kildani B, Milesi L, Merlin F, Mosconi S, et al. Colon cancer. *Crit Rev Oncol Hematol*. 2010;74(2):106–33.
24. Freeman HJ. Early stage colon cancer. *World J Gastroenterol*. 2013;19(46):8468–73.
25. NATIONAL CANCER INSTITUTE. Colon Cancer Treatment (PDQ®)– Patient Version. 2021; Available from: https://www.cancer.gov/types/colorectal/patient/colon-treatment-pdq#_112
26. Simon K. Colorectal cancer development and advances in screening. *Clin Interv Aging*. 2016;11:967–76.
27. Hewitson P, Glasziou P, Irwig L, Towler B, Watson E. Screening for colorectal cancer using the faecal occult blood test, Hemoccult. *Cochrane Database Syst Rev*. 2007;(1).
28. Arévalo-pérez R, Maderuelo C, Lanao JM. Recent advances in colon drug delivery systems. *J Control Release*. 2020;327:703–24.

29. Hayashi JY, Tamanoi F. Exploiting Enzyme Alterations in Cancer for Drug Activation, Drug Delivery, and Nanotherapy. 1st ed. Vol. 42, Enzymes. Elsevier Inc.; 2017. 153–172 p.
30. Truelove SC. Evolution of olsalazine. *Scand J Gastroenterol.* 1988;23(S148):3–6.
31. Esseku F, Adeyeye MC. Bacteria and pH-sensitive polysaccharide-polymer films for colon targeted delivery. *Crit Rev Ther Drug Carrier Syst.* 2011;28(5):395–445.
32. Baumgart DC, Sandborn WJ. Crohn's disease. *Lancet.* 2012;380(9853):1590–605.
33. Bansal V, Malviya R, Malaviya T, Sharma PK. Novel prospective in colon specific drug delivery system. *Polim Med.* 2014;44(2):109–18.
34. Dos Santos J, da Silva GS, Velho MC, Beck RCR. Eudragit®: A versatile family of polymers for hot melt extrusion and 3D printing processes in pharmaceuticals. *Pharmaceutics.* 2021;13(9):1–36.
35. Sinha VR, Kumria R. Microbially triggered drug delivery to the colon. *Eur J Pharm Sci.* 2003;18(1):3–18.
36. Wilson C, Wang Lee W, Mukherji G. Time-Dependent Systems for Colonic Delivery. 2002;(July):243–8.
37. Lee SH, Bajracharya R, Min JY, Han JW, Park BJ, Han HK. Strategic approaches for colon targeted drug delivery: An overview of recent advancements. *Pharmaceutics.* 2020;12(1).
38. Edsbäcker S, Andersson T. Pharmacokinetics of budesonide (Entocort™ EC) capsules for Crohn's disease. *Clin Pharmacokinet.* 2004;43(12):803–21.
39. Philip AK, Philip B. Colon targeted drug delivery systems: A review on

- primary and novel approaches. *Oman Med J.* 2010;25(2):70–8.
40. Sarangi MK, Padhi S. Colon Targeted Drug Delivery System-an Approach for Treating Colonic Ailments. *J Crit Rev.* 2015;2(4):12–8.
 41. Rubinstein A. Microbially controlled drug delivery to the colon. *Biopharm Drug Dispos.* 1990;11(6):465–75.
 42. Yang L, Chu JS, Fix JA. Colon-specific drug delivery: New approaches and in vitro/in vivo evaluation. *Int J Pharm.* 2002;235(1–2):1–15.
 43. Hageman D, Caillet V, Kostohryz J, Madick S. Laparoscopic-assisted colon surgery. *AORN J.* 2008;88(3):415–6.
 44. Häfner MF, Debus J. Radiotherapy for colorectal cancer: Current standards and future perspectives. *Visc Med.* 2016;32(3):172–7.
 45. Folkesson J, Birgisson H, Pahlman L, Cedermark B, Glimelius B, Gunnarsson U. Swedish rectal cancer trial: Long lasting benefits from radiotherapy on survival and local recurrence rate. *J Clin Oncol.* 2005;23(24):5644–50.
 46. Peeters KCMJ, van de Velde CJH, Leer JWH, Martijn H, Junggeburst JMC, Kranenbarg EK, et al. Late side effects of short-course preoperative radiotherapy combined with total mesorectal excision for rectal cancer: Increased bowel dysfunction in irradiated patients - A Dutch Colorectal Cancer Group Study. *J Clin Oncol.* 2005;23(25):6199–206.
 47. Pollack J, Holm T, Cedermark B, Altman D, Holmström B, Glimelius B, et al. Late adverse effects of short-course preoperative radiotherapy in rectal cancer. *Br J Surg.* 2006;93(12):1519–25.
 48. Johdi NA, Sukor NF. Colorectal Cancer Immunotherapy: Options and Strategies. *Front Immunol.* 2020;11:1–18.
 49. Luo C, Cen S, Ding G, Wu W. Mucinous colorectal adenocarcinoma: Clinical

- pathology and treatment options. *Cancer Commun.* 2019;39(1):1–13.
50. Kennedy LB, Salama AKS. A review of cancer immunotherapy toxicity. *CA Cancer J Clin.* 2020;70(2):86–104.
 51. Wu T, Munro AJ, Guanjian L, Liu GJ. Chinese medical herbs for chemotherapy side effects in colorectal cancer patients. *Cochrane Database Syst Rev.* 2005;(1).
 52. Piawah S, Venook AP. Targeted therapy for colorectal cancer metastases: A review of current methods of molecularly targeted therapy and the use of tumor biomarkers in the treatment of metastatic colorectal cancer. *Cancer.* 2019;125(23):4139–47.
 53. Hu T, Li Z, Gao CY, Cho CH. Mechanisms of drug resistance in colon cancer and its therapeutic strategies. *World J Gastroenterol.* 2016;22(30):6876–89.
 54. Prostate A, Cancers B. Curcumin and Its Derivatives as Potential Therapeutic Agents in Prostate, Colon and Breast Cancers. 2019;
 55. Rajesh E, Sankari L, Malathi L, Krupaa JR. Naturally occurring products in cancer therapy. *J Pharm Bioallied Sci.* 2015;7(April):S181–3.
 56. Greenlee H. Natural Products for Cancer Prevention. *Semin Oncol Nurs.* 2012;28(1):29–44.
 57. Kocaadam B, Şanlıer N. Curcumin, an active component of turmeric (*Curcuma longa*), and its effects on health. *Crit Rev Food Sci Nutr.* 2017;57(13):2889–95.
 58. Lestari MLAD, Indrayanto G. Curcumin. Vol. 39, *Profiles of Drug Substances, Excipients and Related Methodology.* 2014. 113–204 p.
 59. Menon VP, Sudheer AR. Antioxidant and anti-inflammatory properties of curcumin. *Adv Exp Med Biol.* 2007;595:105–25.
 60. Willenbacher E, Khan SZ, Mujica SCA, Trapani D, Hussain S, Wolf D, et al.

- Curcumin: New insights into an ancient ingredient against cancer. *Int J Mol Sci.* 2019;20(8):1–13.
61. Rodrigues FC, Anil Kumar N V., Thakur G. Developments in the anticancer activity of structurally modified curcumin: An up-to-date review. *Eur J Med Chem.* 2019;177:76–104.
 62. Wang Y, Lu Z, Lv F, Bie X. Study on microencapsulation of curcumin pigments by spray drying. *Eur Food Res Technol.* 2009;229(3):391–6.
 63. Priyadarsini KI. Photophysics, photochemistry and photobiology of curcumin: Studies from organic solutions, bio-mimetics and living cells. *J Photochem Photobiol C Photochem Rev.* 2009;10(2):81–95.
 64. Tomeh MA, Hadianamrei R, Zhao X. A Review of Curcumin and Its Derivatives as Anticancer Agents. *Int J Mol Sci.* 2019;20(1033).
 65. Wang M, Jiang S, Zhou L, Yu F, Ding H, Li P, et al. Potential Mechanisms of Action of Curcumin for Cancer Prevention: Focus on Cellular Signaling Pathways and miRNAs. *Int J Biol Sci.* 2019;15(6):1200–14.
 66. Thiery JP. Epithelial-mesenchymal transitions in development and pathologies. *Curr Opin Cell Biol.* 2003;15(6):740–6.
 67. Jiang D, Rasul A, Batool R, Sarfraz I, Hussain G, Mateen Tahir M, et al. Potential Anticancer Properties and Mechanisms of Action of Formononetin. *Biomed Res Int.* 2019;2019:645–51.
 68. Wilken R, Veena MS, Wang MB, Srivatsan ES. Curcumin: A review of anti-cancer properties and therapeutic activity in head and neck squamous cell carcinoma. *Mol Cancer.* 2011;10:1–19.
 69. Park J. Anti-carcinogenic properties of curcumin on colorectal cancer. *World J Gastrointest Oncol.* 2010;2(4):169.

70. Xu X, Zhu Y. Curcumin inhibits human non-small cell lung cancer xenografts by targeting STAT3 pathway. *Am J Transl Res.* 2017;9(8):3633–41.
71. Wang H, Zhang K, Liu J, Yang J, Tian Y, Yang C, et al. Curcumin Regulates Cancer Progression: Focus on ncRNAs and Molecular Signaling Pathways. *Front Oncol.* 2021;11(April):1–10.
72. Yu X, Zhong J, Yan L, Li J, Wang H, Wen Y, et al. Curcumin exerts antitumor effects in retinoblastoma cells by regulating the JNK and p38 MAPK pathways. *Int J Mol Med.* 2016;38(3):861–8.
73. Luo J, Manning BD, Cantley LC. Targeting the PI3K-Akt pathway in human cancer: Rationale and promise. *Cancer Cell.* 2003;4(4):257–62.
74. Yu JSL, Cui W. Proliferation, survival and metabolism: The role of PI3K/AKT/ mTOR signalling in pluripotency and cell fate determination. *Dev.* 2016;143(17):3050–60.
75. Akkoç Y, Berrak Ö, Arisan ED, Obakan P, Çoker-Gürkan A, Palavan-Ünsal N. Inhibition of PI3K signaling triggered apoptotic potential of curcumin which is hindered by Bcl-2 through activation of autophagy in MCF-7 cells. *Biomed Pharmacother.* 2015;71:161–71.
76. Shakibaei M, Buhrmann C, Kraehe P, Shayan P, Lueders C, Goel A. Curcumin chemosensitizes 5-fluorouracil resistant MMR-deficient human colon cancer cells in high density cultures. *PLoS One.* 2014;9(1):1–12.
77. Sesarman AA, Tefas L, Sylvester B, Licarete E, Rauca V, Luput L, et al. Anti-angiogenic and anti-inflammatory effects of long-circulating liposomes co-encapsulating curcumin and doxorubicin on C26 murine colon cancer cells. *Pharmacol Reports.* 2017;
78. Xiao B, Si X, Han MK, Viennois E, Zhang M, Merlin D. Co-delivery of

- camptothecin and curcumin by cationic polymeric nanoparticles for synergistic colon cancer combination chemotherapy. *J Mater Chem B*. 2015;3(39):7724–33.
79. Lev-Ari S, Strier L, Kazanov D, Madar-Shapiro L, Dvory-Sobol H, Pinchuk I, et al. Celecoxib and curcumin synergistically inhibit the growth of colorectal cancer cells. *Clin Cancer Res*. 2005;11(18):6738–44.
80. Li L, Ahmed B, Mehta K, Li L, Ahmed B, Mehta K. Liposomal curcumin with and without oxaliplatin: effects on cell growth, apoptosis, and angiogenesis in colorectal cancer. *Mol Cancer Ther*. 2007;1276–82.
81. Chaurasia S, Chaubey P, Patel RR, Kumar N, Mishra B. Curcumin-polymeric nanoparticles against colon-26 tumor-bearing mice: Cytotoxicity, pharmacokinetic and anticancer efficacy studies. *Drug Dev Ind Pharm*. 2016;42(5):694–700.
82. Anitha A, Deepa N, Chennazhi KP, Lakshmanan VK, Jayakumar R. Combinatorial anticancer effects of curcumin and 5-fluorouracil loaded thiolated chitosan nanoparticles towards colon cancer treatment. *Biochim Biophys Acta - Gen Subj*. 2014;1840(9):2730–43.
83. Yang X, Li Z, Wang N, Li L, Song L, He T, et al. Curcumin-Encapsulated Polymeric Micelles Suppress the Development of Colon Cancer In Vitro and In Vivo. *Sci Rep*. 2015;1–15.
84. Sharma RA, Euden SA, Platton SL, Cooke DN, Shafayat A, Hewitt HR, et al. Phase I clinical trial of oral curcumin: Biomarkers of systemic activity and compliance. *Clin Cancer Res*. 2004;10(20):6847–54.
85. Greil R, Ressler SG, Weiss L, Schönlieb C, Magnes T, Radl B, et al. A phase 1 dose-escalation study on the safety, tolerability and activity of liposomal

- curcumin - (LipocurcTM) in patients with locally advanced or metastatic cancer. *Cancer Chemother Pharmacol.* 2018;0(0):0.
86. Storka A, Vcelar B, Klickovic U, Gouya G, Weisshaar S, Aschauer S, et al. Safety , tolerability and pharmacokinetics of liposomal curcumin (LipocurcTM) in healthy humans. 2014;2014:1–12.
87. Study Investigating the Ability of Plant Exosomes to Deliver Curcumin to Normal and Colon Cancer Tissue [Internet]. NCT01294072. Available from: <https://clinicaltrials.gov/ct2/show/NCT01294072>
88. Liu W, Zhai Y, Heng X, Che FY, Chen W, Sun D, et al. Oral bioavailability of curcumin: problems and advancements. *J Drug Target.* 2016;24(8):694–702.
89. Nair RS, Morris A, Billa N, Leong CO. An Evaluation of Curcumin-Encapsulated Chitosan Nanoparticles for Transdermal Delivery. *AAPS PharmSciTech.* 2019;20(2):1–13.
90. Ireson CR, Jones DJL, Boocock DJ, Farmer PB, Gescher AJ, Orr S, et al. Metabolism of the cancer chemopreventive agent curcumin in human and rat intestine. *Cancer Epidemiol Biomarkers Prev.* 2002;11(1):105–11.
91. Ireson C, Orr S, Jones DJL, Verschoyle R, Lim CK, Luo JL, et al. Characterization of metabolites of the chemopreventive agent curcumin in human and rat hepatocytes and in the rat in vivo, and evaluation of their ability to inhibit phorbol ester-induced prostaglandin E₂ production. *Cancer Res.* 2001;61(3):1058–64.
92. Hoehle SI, Pfeiffer E, Sólyom AM, Metzler M. Metabolism of curcuminoids in tissue slices and subcellular fractions from rat liver. *J Agric Food Chem.* 2006;54(3):756–64.
93. Safavy A, Raisch KP, Mantena S, Sanford LL, Sham SW, Krishna NR, et al.

- Design and development of water-soluble curcumin conjugates as potential anticancer agents. *J Med Chem.* 2007;50(24):6284–8.
94. Wichitnithad W, Nimmannit U, Wacharasindhu S, Rojsitthisak P. Synthesis, characterization and biological evaluation of succinate prodrugs of curcuminoids for colon cancer treatment. *Molecules.* 2011;16(2):1888–900.
 95. Fang X, Fang L, Gou S, Cheng L. Design and synthesis of dimethylaminomethyl-substituted curcumin derivatives/analogues: Potent antitumor and antioxidant activity, improved stability and aqueous solubility compared with curcumin. *Bioorganic Med Chem Lett.* 2013;23(5):1297–301.
 96. De Jong WH, Borm PJA. Drug delivery and nanoparticles: Applications and hazards. *Int J Nanomedicine.* 2008;3(2):133–49.
 97. Patra JK, Das G, Fraceto LF, Campos EVR, Rodriguez-Torres MDP, Acosta-Torres LS, et al. Nano based drug delivery systems: Recent developments and future prospects. *J Nanobiotechnology.* 2018;16(1):1–33.
 98. Zhang RX, Ahmed T, Li LY, Li J, Abbasi AZ, Wu XY. Design of nanocarriers for nanoscale drug delivery to enhance cancer treatment using hybrid polymer and lipid building blocks. *Nanoscale.* 2017;9(4):1334–55.
 99. Kumari A, Yadav SK, Yadav SC. Biodegradable polymeric nanoparticles based drug delivery systems. *Colloids Surfaces B Biointerfaces.* 2010;75(1):1–18.
 100. Pérez-Herrero E, Fernández-Medarde A. Advanced targeted therapies in cancer: Drug nanocarriers, the future of chemotherapy. *Eur J Pharm Biopharm.* 2015;93(March):52–79.
 101. Van Der Vlies AJ, Morisaki M, Neng HI, Hansen EM, Hasegawa U. Framboidal Nanoparticles Containing a Curcumin-Phenylboronic Acid

- Complex with Antiangiogenic and Anticancer Activities. *Bioconjug Chem.* 2019;30(3):861–70.
102. Leyva-Gómez G, Piñón-Segundo E, Mendoza-Muñoz N, Zambrano-Zaragoza ML, Mendoza-Elvira S, Quintanar-Guerrero D. Approaches in polymeric nanoparticles for vaginal drug delivery: A review of the state of the art. *Int J Mol Sci.* 2018;19(6):1–19.
 103. Wilczewska AZ, Niemirowicz K, Markiewicz KH, Car H. Nanoparticles as drug delivery systems. *Pharmacol Reports.* 2012;64(5):1020–37.
 104. Aliabadi HM, Lavasanifar A. Polymeric micelles for drug delivery. *Expert Opin Drug Deliv.* 2006;3(1):139–62.
 105. Zhou Q, Zhang L, Yang TH, Wu H. Stimuli-responsive polymeric micelles for drug delivery and cancer therapy. *Int J Nanomedicine.* 2018;13:2921–42.
 106. Cho H, Lai TC, Tomoda K, Kwon GS. Polymeric Micelles for Multi-Drug Delivery in Cancer. *AAPS PharmSciTech.* 2014;16(1):10–20.
 107. Lin M, Dai Y, Xia F, Zhang X. Advances in non-covalent crosslinked polymer micelles for biomedical applications. *Mater Sci Eng C.* 2021;119.
 108. Shah S, Dhawan V, Holm R, Nagarsenker MS, Perrie Y. Liposomes: Advancements and innovation in the manufacturing process. *Adv Drug Deliv Rev.* 2020;154–155:102–22.
 109. Li Z, Tan S, Li S, Shen Q, Wang K. Cancer drug delivery in the nano era: An overview and perspectives (Review). *Oncol Rep.* 2017;38(2):611–24.
 110. Rivankar S. An overview of doxorubicin formulations in cancer therapy. *J Cancer Res Ther.* 2014;10(4):853–8.
 111. Suhail M, Rosenholm JM, Minhas MU, Badshah SF, Naeem A, Khan KU, et al. Nanogels as drug-delivery systems: A comprehensive overview. *Ther Deliv.*

- 2019;10(11):697–717.
112. Li Z, Huang J, Wu J. PH-Sensitive nanogels for drug delivery in cancer therapy. *Biomater Sci.* 2021;9(3):574–89.
 113. Pinelli F, Ortola ÓF, Makvandi P, Perale G, Rossi F. In vivo drug delivery applications of nanogels: A review. *Nanomedicine.* 2020;15(27):2707–27.
 114. Singh P, Pandit S, Mokkaipati VRSS, Garg A, Ravikumar V, Mijakovic I. Gold Nanoparticles in Diagnostics and Therapeutics for Human Cancer. *Int J Mol Sci.* 2018;19(1979).
 115. Sztandera K, Gorzkiewicz M, Klajnert-Maculewicz B. Gold Nanoparticles in Cancer Treatment. *Mol Pharm.* 2019;16(1):1–23.
 116. Yang C, Uertz J, Chithrani DB. Colloidal gold-mediated delivery of bleomycin for improved outcome in chemotherapy. *Nanomaterials.* 2016;6(3):1–15.
 117. Patrulea V, Ostafe V, Borchard G, Jordan O. Chitosan as a starting material for wound healing applications. *Eur J Pharm Biopharm.* 2015;97:417–26.
 118. Sinha VR, Kumria R. Polysaccharides in colon-specific drug delivery. *Int J Pharm.* 2001;224(1–2):19–38.
 119. Vinodh R, Sasikumar Y, Kim HJ, Atchudan R, Yi M. Chitin and chitosan based biopolymer derived electrode materials for supercapacitor applications: A critical review. *J Ind Eng Chem.* 2021;104:155–71.
 120. Gulbake A, Jain SK. Chitosan: A potential polymer for colon-specific drug delivery system. *Expert Opin Drug Deliv.* 2012;9(6):713–29.
 121. Muxika A, Etxabide A, Uranga J, Guerrero P, de la Caba K. Chitosan as a bioactive polymer: Processing, properties and applications. *Int J Biol Macromol.* 2017;105:1358–68.
 122. Rizeq BR, Younes NN, Rasool K, Nasrallah GK. Synthesis, bioapplications,

- and toxicity evaluation of chitosan-based nanoparticles. *Int J Mol Sci.* 2019;20(22).
123. Kaur G, Rana V, Jain S, Tiwary AK. Colon delivery of budesonide: Evaluation of chitosan-chondroitin sulfate interpolymer complex. *AAPS PharmSciTech.* 2010;11(1):36–45.
 124. Huang BB, Li GF, Luo JH, Duan L, Nobuaki K, Akira Y. Permeabilities of rebamipide via rat intestinal membranes and its colon specific delivery using chitosan capsule as a carrier. *World J Gastroenterol.* 2008;14(31):4928–37.
 125. Akhlaghi SP, Saremi S, Ostad SN, Dinarvand R, Atyabi F. Discriminated effects of thiolated chitosan-coated pMMA paclitaxel-loaded nanoparticles on different normal and cancer cell lines. *Nanomedicine Nanotechnology, Biol Med.* 2010;6(5):689–97.
 126. Aibani N, Rai R, Patel P, Cuddihy G, Wasan EK. Chitosan Nanoparticles at the Biological Interface: Implications for Drug Delivery. *Pharmaceutics.* 2021;13(10):1686.
 127. G. Nava-Arzaluz M, Pinon-Segundo E, Ganem-Rondero A, Lechuga-Ballesteros D. Single Emulsion-Solvent Evaporation Technique and Modifications for the Preparation of Pharmaceutical Polymeric Nanoparticles. *Recent Pat Drug Deliv Formul.* 2012;6(3):209–23.
 128. Iqbal M, Zafar N, Fessi H, Elaissari A. Double emulsion solvent evaporation techniques used for drug encapsulation. *Int J Pharm.* 2015;496(2):173–90.
 129. Zieli A., Carreiró F., Oliveira A. et al. Polymeric Nanoparticles: Production, Characterization, Toxicology and Ecotoxicology. *Molecules.* 2020;25(3731).
 130. Ding S, Serra CA, Vandamme TF, Yu W, Anton N. Double emulsions prepared by two–step emulsification: History, state-of-the-art and perspective. *J*

- Control Release. 2019;295:31–49.
131. Nagpal K, Singh SK, Mishra DN. Chitosan nanoparticles: A promising system in novel drug delivery. *Chem Pharm Bull.* 2010;58(11):1423–30.
 132. Lim K, Hamid ZAA. Polymer nanoparticle carriers in drug delivery systems: Research trend. *Applications of Nanocomposite Materials in Drug Delivery.* Elsevier Inc.; 2018. 217–237 p.
 133. Dubey S, Mody N, Sharma R, Agrawal U, Vyas SP. Nanobiomaterials: Novel nanoplatforms for protein and peptide delivery. *Nanobiomaterials in Drug Delivery: Applications of Nanobiomaterials.* Elsevier Inc.; 2016. 111–146 p.
 134. Galindo-Rodríguez SA, Puel F, Briançon S, Allémann E, Doelker E, Fessi H. Comparative scale-up of three methods for producing ibuprofen-loaded nanoparticles. *Eur J Pharm Sci.* 2005;25(4–5):357–67.
 135. Galindo-Rodríguez S, Allémann E, Fessi H, Doelker E. Physicochemical parameters associated with nanoparticle formation in the salting-out, emulsification-diffusion, and nanoprecipitation methods. *Pharm Res.* 2004;21(8):1428–39.
 136. Bhattacharjee S et al. Polymeric Nanoparticles: Production, Characterization, Toxicology and Ecotoxicology. *Molecules.* 2020;25(3731):195–240.
 137. Pineda-Reyes AM, Hernández Delgado M, De La Luz Zambrano-Zaragoza M, Leyva-Gómez G, Mendoza-Muñoz N, Quintanar-Guerrero D. Implementation of the emulsification-diffusion method by solvent displacement for polystyrene nanoparticles prepared from recycled material. *RSC Adv.* 2021;11(4):2226–34.
 138. Piñón-Segundo E, Llera-Rojas VG, Leyva-Gómez G, Urbán-Morlán Z, Mendoza-Muñoz N, Quintanar-Guerrero D. The emulsification-diffusion method to obtain polymeric nanoparticles: Two decades of research. *Nanoscale*

- Fabrication, Optimization, Scale-up and Biological Aspects of Pharmaceutical Nanotechnology. 2017. 51–83 p.
139. Chidambaram M, Krishnasamy K. Modifications to the conventional nanoprecipitation technique: An approach to fabricate narrow sized polymeric Nanoparticles. *Adv Pharm Bull.* 2014;4(2):205–8.
 140. Martínez Rivas CJ, Tarhini M, Badri W, Miladi K, Greige-Gerges H, Nazari QA, et al. Nanoprecipitation process: From encapsulation to drug delivery. *Int J Pharm.* 2017;532(1):66–81.
 141. Peltonen L, Valo H, Kolakovic R, Laaksonen T, Hirvonen J. Electrospraying, spray drying and related techniques for production and formulation of drug nanoparticles. *Expert Opin Drug Deliv.* 2010;7(6):705–19.
 142. Salama AH. Spray drying as an advantageous strategy for enhancing pharmaceuticals bioavailability. *Drug Deliv Transl Res.* 2020;10(1).
 143. Marante T, Viegas C, Duarte I, Macedo AS, Fonte P. An overview on spray-drying of protein-loaded polymeric nanoparticles for dry powder inhalation. *Pharmaceutics.* 2020;12(11):1–23.
 144. Chakravarty P, Famili A, Nagapudi K, Al-Sayah MA. Using supercritical fluid technology as a green alternative during the preparation of drug delivery systems. Vol. 11, *Pharmaceutics.* 2019. 1–34 p.
 145. Girotra P, Singh SK, Nagpal K. Supercritical fluid technology: A promising approach in pharmaceutical research. *Pharm Dev Technol.* 2013;18(1):22–38.
 146. Mavila S, Eivgi O, Berkovich I, Lemcoff NG. Intramolecular Cross-Linking Methodologies for the Synthesis of Polymer Nanoparticles. *Chem Rev.* 2016;116(3):878–961.
 147. Lima AC, Sher P, Mano JF. Production methodologies of polymeric and

- hydrogel particles for drug delivery applications. *Expert Opin Drug Deliv.* 2012;9(2):231–48.
148. Mohamed MA, Jaafar J, Ismail AF, Othman MHD, Rahman MA. Fourier Transform Infrared (FTIR) Spectroscopy. *Membr Charact.* 2017;3–29.
 149. Bates JB. Fourier Transform Infrared Spectroscopy Published by : American Association for the Advancement of Science. *Science* (80-). 1976;191(4222):31–7.
 150. Berthomieu C, Hienerwadel R. Fourier transform infrared (FTIR) spectroscopy. *Photosynth Res.* 2009;101(2–3):157–70.
 151. Bacsik Z, Mink J, Keresztury G. FTIR spectroscopy of the atmosphere. I. Principles and methods. *Appl Spectrosc Rev.* 2004;39(3):295–363.
 152. Deleanu C, Jocelyn Paré JR. Chapter 6 Nuclear magnetic resonance spectroscopy (NMR): Principles and applications. *Tech Instrum Anal Chem.* 1997;18(C):179–237.
 153. Lens PNL, Hemminga MA. Nuclear magnetic resonance in environmental engineering: Principles and applications. *Biodegradation.* 1998;9(6):393–409.
 154. Behroozmand AA, Keating K, Auken E. A Review of the Principles and Applications of the NMR Technique for Near-Surface Characterization. *Surv Geophys.* 2015;36(1):27–85.
 155. Mlynárik V. Introduction to nuclear magnetic resonance. *Anal Biochem.* 2017;529:4–9.
 156. Gary M. McClelland, Ragnar Erlandsson and SC. ATOMIC FORCE MICROSCOPY: GENERAL PRINCIPLES AND A NEW IMPLEMENTATION. Springer. 1987;1307–14.
 157. Cappella B, Dietler G. Force-distance curves by atomic force microscopy. *Surf*

- Sci Rep. 1999;34(1–3):1–3.
158. Johnson D, Hilal N, Bowen WR. Basic principles of atomic force microscopy. *Atomic Force Microscopy in Process Engineering*. Elsevier Ltd; 2009. 1–30 p.
 159. Sandhu R, Singh N, Dhankhar J, Kama G, Sharma R. Dynamic light scattering (DLS) technique, principle, theoretical considerations and applications. *Nanotechnological Biochem Tech Assess Qual Saf Milk Milk Prod*. 2018;(February 2019):135–7.
 160. Bunaciu AA, Udriștioiu E gabriela, Aboul-Enein HY. X-Ray Diffraction: Instrumentation and Applications. *Crit Rev Anal Chem*. 2015;45(4):289–99.
 161. Walenta G, Füllmann T. Advances in quantitative XRD analysis for clinker, cements, and cementitious additions. *Powder Diffr*. 2004;19(1):40–4.
 162. Chauhan A. Powder XRD Technique and its Applications in Science and Technology. *J Anal Bioanal Tech*. 2014;5(6).
 163. De Blasio C. *Fundamentals of Biofuels Engineering and Technology*. Springer. 2019. 46–56 p.
 164. Loganathan S, Valapa RB, Mishra RK, Pugazhenti G, Thomas S. *Thermogravimetric Analysis for Characterization of Nanomaterials*. Vol. 3, *Thermal and Rheological Measurement Techniques for Nanomaterials Characterization*. Elsevier Inc.; 2017. 67–108 p.
 165. Ng HM, Saidi NM, Omar FS, Ramesh K, Ramesh S, Bashir S. *Thermogravimetric Analysis of Polymers*. *Encycl Polym Sci Technol*. 2018;(13):1–29.
 166. Wu H, Zhang W, Mu W. Recent studies on the biological production of D-mannose. *Appl Microbiol Biotechnol*. 2019;103(21–22):8753–61.
 167. Domenici L, Monti M, Bracchi C, Giorgini M, Colagiovanni V, Muzii L, et al.

- D-mannose: a promising support for acute urinary tract infections in women. A pilot study. *Eur Rev Med Pharmacol Sci*. 2016;20(13):2920–5.
168. Wei Z, Huang L, Cui L, Zhu X. Mannose: Good player and assister in pharmacotherapy. *Biomed Pharmacother*. 2020;129(May).
169. Gonzalez PS, O’Prey J, Cardaci S, Barthet VJA, Sakamaki J ichi, Beaumatin F, et al. Mannose impairs tumour growth and enhances chemotherapy. *Nature*. 2018;563(7733):719–23.
170. Dalle Vedove E, Costabile G, Merkel OM. Mannose and Mannose-6-Phosphate Receptor–Targeted Drug Delivery Systems and Their Application in Cancer Therapy. *Adv Healthc Mater*. 2018;7(14):1–37.
171. Wang Y, Xie S, He B. Mannose shows antitumour properties against lung cancer via inhibiting proliferation, promoting cisplatin-mediated apoptosis and reducing metastasis. *Mol Med Rep*. 2020;22(4):2957–65.
172. Comuzzo P, Battistutta F. Acidification and pH Control in Red Wines [Internet]. *Red Wine Technology*. Elsevier Inc.; 2018. 17–34 p. Available from: <http://dx.doi.org/10.1016/B978-0-12-814399-5.00002-5>
173. Li L, Zhang X, Pi C, Yang H, Zheng X, Zhao L, et al. Review of curcumin physicochemical targeting delivery system. *Int J Nanomedicine*. 2020;15:9799–821.
174. B, ANDERSON T V. Initial Rate Studies of Hydrolysis and Acyl Migration in Methylprednisolone 21-Hemisuccinate and 17-Hemisuccinate. *J Pharm Sci*. 1981;70:181–6.
175. Johansen M, Larsen C. Stability and kinetics of hydrolysis of metronidazole monosuccinate in aqueous solution and in plasma. *Int J Pharm*. 1984;21(2):201–9.

176. La-Scalea MA, Menezes CMS, Matsutami GC, Polli MC, Serrano SHP, Ferreira EI. Molecular modeling of the voltammetric oxidation at a glassy carbon electrode of the antimalarial drug primaquine and its prodrugs succinylprimaquine and maleylprimaquine. *Electrochim Acta*. 2006;51(24):5103–11.
177. Muangnoi C, Bhuket PRN, Jithavech P, Wichitnithad W, Srikun O, Nerungsi C, et al. Scale-up synthesis and in vivo anti-tumor activity of curcumin diethyl disuccinate, an ester prodrug of curcumin, in HepG2-xenograft mice. *Pharmaceutics*. 2019;11(8):1–14.
178. Ye Z, Zhang Q, Wang S, Bharate P, Varela-Aramburu S, Lu M, et al. Tumour-Targeted Drug Delivery with Mannose-Functionalized Nanoparticles Self-Assembled from Amphiphilic β -Cyclodextrins. *Chem - A Eur J*. 2016;22(43):15216–21.
179. Xiong M, Lei Q, You X, Gao T, Song X, Xia Y, et al. Mannosylated liposomes improve therapeutic effects of paclitaxel in colon cancer models. *J Microencapsul*. 2017;34(6):513–21.
180. Kim TH, Jin H, Kim HW, Cho MH, Cho CS. Mannosylated chitosan nanoparticle-based cytokine gene therapy suppressed cancer growth in BALB/c mice bearing CT-26 carcinoma cells. *Mol Cancer Ther*. 2006;5(7):1723–32.
181. Chaubey P, Mishra B, Mudavath SL, Patel RR, Chaurasia S, Sundar S, et al. Mannose-conjugated curcumin-chitosan nanoparticles: Efficacy and toxicity assessments against *Leishmania donovani*. *Int J Biol Macromol*. 2018;111:109–20.
182. 宗莉, 罗娟, 焦岩, 杜明珠, 姚文军. Simple preparation method for mannosylated chitosan. CHINA; CN102477107A, 2010.

183. Ejaz S, Ihsan A, Noor T, Shabbir S, Imran M. Mannose functionalized chitosan nanosystems for enhanced antimicrobial activity against multidrug resistant pathogens. *Polym Test*. 2020;91.
184. Jahromi MAM, Al-Musawi S, Pirestani M, Ramandi MF, Ahmadi K, Rajayi H, et al. Curcumin-loaded chitosan tripolyphosphate nanoparticles as a safe, natural and effective antibiotic inhibits the infection of staphylococcus aureus and pseudomonas aeruginosa in vivo. *Iran J Biotechnol*. 2014;12(3).
185. Modasiya MK, Patel VM. Studies on solubility of curcumin. *Int J Pharm LIFE Sci*. 2012;3(3):1490–7.
186. Chen Y, Wu D, Zhong W, Kuang S, Luo Q, Song L, et al. Evaluation of the PEG density in the PEGylated chitosan nanoparticles as a drug carrier for curcumin and mitoxantrone. *Nanomaterials*. 2018;8(7).
187. Kamoun EA. N-succinyl chitosan-dialdehyde starch hybrid hydrogels for biomedical applications. *J Adv Res*. 2016;7(1):69–77.
188. Esfandiarpour-Boroujeni S, Bagheri-Khoulenjani S, Mirzadeh H, Amanpour S. Fabrication and study of curcumin loaded nanoparticles based on folate-chitosan for breast cancer therapy application. *Carbohydr Polym*. 2017;168:14–21.
189. Valencia MS, Silva Júnior MF da, Xavier-Júnior FH, Veras B de O, Albuquerque PBS de, Borba EF de O, et al. Characterization of curcumin-loaded lecithin-chitosan bioactive nanoparticles. *Carbohydr Polym Technol Appl*. 2021;2:100119.
190. Cai L, Qin X, Xu Z, Song Y, Jiang H, Wu Y, et al. Comparison of Cytotoxicity Evaluation of Anticancer Drugs between Real-Time Cell Analysis and CCK-8 Method. *ACS Omega*. 2019;4(7):12036–42.

191. Chen Y, Lu Y, Lee RJ, Xiang G. Nano encapsulated curcumin: And its potential for biomedical applications. *Int J Nanomedicine*. 2020;15:3099–120.
192. Chaubey P, Patel RR, Mishra B. Development and optimization of curcumin-loaded mannosylated chitosan nanoparticles using response surface methodology in the treatment of visceral leishmaniasis. *Expert Opin Drug Deliv*. 2014;11(8):1163–81.
193. G. Asthana, A. Asthana, D.Kholi SV. Mannosylated Chitosan Nanoparticles for Delivery of Antisense Oligonucleotides for Macrophage Targeting. *Biomed Res Int*. 2021;2021.
194. Fikai D, Albu MG, Sonmez M, Fikai A, Andronescu E. Advances in the field of soft tissue engineering: From pure regenerative to integrative solutions. *Nanobiomaterials in Soft Tissue Engineering: Applications of Nanobiomaterials*. Elsevier Inc.; 2016. 355–386 p.
195. Tarhini M, Badri W, Greige-Gerges H, Fessi H, Elaissari A. Nanoparticles/nanoplatform to carry and deliver the drug molecules to the target site. *Drug Deliv Devices Ther Syst*. 2021;249–66.
196. Pooresmaeil M, Namazi H. Facile preparation of pH-sensitive chitosan microspheres for delivery of curcumin; characterization, drug release kinetics and evaluation of anticancer activity. *Int J Biol Macromol*. 2020;162:501–11.
197. You X, Kang Y, Hollett G, Chen X, Zhao W, Gu Z, et al. Polymeric nanoparticles for colon cancer therapy: overview and perspectives. *J Mater Chem B*. 2016;4(48):7779–92.
198. Herdiana Y, Wathoni N, Shamsuddin S, Joni IM, Muchtaridi M. Chitosan-based nanoparticles of targeted drug delivery system in breast cancer treatment. *Polymers (Basel)*. 2021;13(11).

199. Sultan MH, Moni SS, Madkhali OA, Bakkari MA, Alshahrani S, Alqahtani SS, et al. Characterization of cisplatin-loaded chitosan nanoparticles and rituximab-linked surfaces as target-specific injectable nano-formulations for combating cancer. *Sci Rep.* 2022;12(1):1–16.
200. Samrot A V., Burman U, Philip SA, Shobana N, Chandrasekaran K. Synthesis of curcumin loaded polymeric nanoparticles from crab shell derived chitosan for drug delivery. *Informatics Med Unlocked.* 2018;10:159–82.
201. Xiao J, Nian S, Huang Q. Assembly of kafirin/carboxymethyl chitosan nanoparticles to enhance the cellular uptake of curcumin. *Food Hydrocoll.* 2015;51:166–75.
202. Villegas-Peralta Y, López-Cervantes J, Madera Santana TJ, Sánchez-Duarte RG, Sánchez-Machado DI, Martínez-Macías M del R, et al. Impact of the molecular weight on the size of chitosan nanoparticles: characterization and its solid-state application. *Polym Bull.* 2021;78(2):813–32.
203. Kamaraj S, Palanisamy UM, Kadhar Mohamed MSB, Gangasalam A, Maria GA, Kandasamy R. Curcumin drug delivery by vanillin-chitosan coated with calcium ferrite hybrid nanoparticles as carrier. *Eur J Pharm Sci.* 2018;116(April 2017):48–60.
204. Ahmadi F, Ghasemi-Kasman M, Ghasemi S, Tabari MG, Pourbagher R, Kazemi S, et al. Induction of apoptosis in HeLa cancer cells by an ultrasonic-mediated synthesis of curcumin-loaded chitosan-alginate-STPP nanoparticles. *Int J Nanomedicine.* 2017;12:8545–56.
205. Gillies RJ, Raghunand N, Karczmar GS, Bhujwalla ZM. MRI of the tumor microenvironment. *J Magn Reson Imaging.* 2002;16(4):430–50.
206. Kim JO, Ramasamy T, Tran TH, Choi JY, Cho HJ, Kim JH, et al. Layer-by-

- layer coated lipid-polymer hybrid nanoparticles designed for use in anticancer drug delivery. *Carbohydr Polym.* 2014;102(1):653–61.
207. Kumari M, Sharma N, Manchanda R, Gupta N, Syed A, Bahkali AH, et al. PGMD/curcumin nanoparticles for the treatment of breast cancer. *Sci Rep.* 2021;11(1):1–17.
208. Vijayakurup V, Thulasidasan AT, Shankar MG, Retnakumari AP, Nandan CD, Somaraj J, et al. Chitosan encapsulation enhances the bioavailability and tissue retention of curcumin and improves its efficacy in preventing b[a]p-induced lung carcinogenesis. *Cancer Prev Res.* 2019;12(4):225–36.
209. Babu NJ, Nangia A. Solubility advantage of amorphous drugs and pharmaceutical cocrystals. *Cryst Growth Des.* 2011;11(7):2662–79.
210. Dhanasekaran S, Rameshthangam P, Venkatesan S, Singh SK, Vijayan SR. In Vitro and In Silico Studies of Chitin and Chitosan Based Nanocarriers for Curcumin and Insulin Delivery. *J Polym Environ.* 2018;26(10):4095–113.
211. Han J, Chen F, Gao C, Zhang Y, Tang X. Environmental stability and curcumin release properties of Pickering emulsion stabilized by chitosan/gum arabic nanoparticles. *Int J Biol Macromol.* 2020;157:202–11.
212. Ubeyitogullari A, Ciftci ON. A novel and green nanoparticle formation approach to forming low-crystallinity curcumin nanoparticles to improve curcumin's bioaccessibility. *Sci Rep.* 2019;9(1):1–11.
213. Vyazovkin S. “Nothing Can Hide Itself from Thy Heat”: Understanding Polymers via Unconventional Applications of Thermal Analysis. *Macromol Rapid Commun.* 2019;40(1):1–15.
214. Arab C, El Kurdi R, Patra D. Chitosan coated zinc curcumin oxide nanoparticles for the determination of ascorbic acid. *J Mol Liq.*

2021;328:115504.

215. Sun X, Yu D, Ying Z, Pan C, Wang N, Huang F, et al. Fabrication of ion-crosslinking aminochitosan nanoparticles for encapsulation and slow release of curcumin. *Pharmaceutics*. 2019;11(11).
216. Masarudin MJ, Cutts SM, Evison BJ, Phillips DR, Pigram PJ. Factors determining the stability, size distribution, and cellular accumulation of small, monodisperse chitosan nanoparticles as candidate vectors for anticancer drug delivery: Application to the passive encapsulation of [14C]-doxorubicin. *Nanotechnol Sci Appl*. 2015;8:67–80.
217. Ozturk K, Arslan FB, Tavukcuoglu E, Esendagli G, Calis S. Aggregation of chitosan nanoparticles in cell culture: Reasons and resolutions. *Int J Pharm*. 2020;578(December 2019):119119.
218. Peng S, Li Z, Zou L, Liu W, Liu C, McClements DJ. Improving curcumin solubility and bioavailability by encapsulation in saponin-coated curcumin nanoparticles prepared using a simple pH-driven loading method. *Food Funct*. 2018;9(3):1829–39.
219. Davis BM, Pahlitzsch M, Guo L, Balendra S, Shah P, Ravindran N, et al. Topical Curcumin Nanocarriers are Neuroprotective in Eye Disease. *Sci Rep*. 2018;8(1):1–14.
220. Dang LH, Nguyen TH, Tran HLB, Doan VN, Tran NQ. Injectable Nanocurcumin-Formulated Chitosan-g-Pluronic Hydrogel Exhibiting a Great Potential for Burn Treatment. *J Healthc Eng*. 2018;2018.
221. Ma Y, Thurecht KJ, Coombes AGA. Development of enteric-coated, biphasic chitosan/HPMC microcapsules for colon-targeted delivery of anticancer drug-loaded nanoparticles. *Int J Pharm*. 2021;607:1–9.

222. Sorasitthiyankarn FN, Muangnoi C, Rojsitthisak P, Rojsitthisak P. Chitosan-alginate nanoparticles as effective oral carriers to improve the stability, bioavailability, and cytotoxicity of curcumin diethyl disuccinate. *Carbohydr Polym.* 2021;256.
223. Sengel-turk CT, Gumustas M, Uslu B, Ozkan SA. Nanosized Drug Carriers for Oral Delivery of Anticancer Compounds and the Importance of the Chromatographic Techniques [Internet]. *Nano- and Microscale Drug Delivery Systems*. Elsevier Inc.; 2017. 165–195 p. Available from: <http://dx.doi.org/10.1016/B978-0-323-52727-9/00010-8>
224. Wang H, Zhang T, Sun W, Wang Z, Zuo D, Zhou Z, et al. Erianin induces G2 / M-phase arrest , apoptosis , and autophagy via the ROS / JNK signaling pathway in human osteosarcoma cells in vitro and in vivo. 2016;
225. Sabra R, Billa N, Roberts CJ. Cetuximab-conjugated chitosan-pectinate (modified) composite nanoparticles for targeting colon cancer. *Int J Pharm* [Internet]. 2019;572:118775. Available from: <https://doi.org/10.1016/j.ijpharm.2019.118775>
226. Chuah LH, Roberts CJ, Billa N, Abdullah S, Rosli R. Cellular uptake and anticancer effects of mucoadhesive curcumin-containing chitosan nanoparticles. *Colloids Surfaces B Biointerfaces* [Internet]. 2014;116:228–36. Available from: <http://dx.doi.org/10.1016/j.colsurfb.2014.01.007>
227. Mortezaee K, Salehi E, Mirtavoos-mahyari H, Motevaseli E, Najafi M, Farhood B, et al. Mechanisms of apoptosis modulation by curcumin: Implications for cancer therapy. *J Cell Physiol.* 2019;234(8):12537–50.
228. Ismail NI, Othman I, Abas F, Lajis NH, Naidu R. Mechanism of apoptosis induced by curcumin in colorectal cancer. Vol. 20, *International Journal of*

Molecular Sciences. 2019.

229. Gobeil S, Boucher CC, Nadeau D, Poirier GG. Characterization of the necrotic cleavage of poly (ADP-ribose) polymerase (PARP-1): implication of lysosomal proteases. 2001;588–94.
230. Pozzesi N, Fierabracci A, Liberati AM, Martelli MP, Ayroldi E, Riccardi C, et al. Role of caspase-8 in thymus function. *Cell Death Differ* [Internet]. 2013;21(2):226–33. Available from: <http://dx.doi.org/10.1038/cdd.2013.166>
231. Shakibaei M, Mobasheri A, Lueders C, Busch F, Shayan P, Goel A. Curcumin Enhances the Effect of Chemotherapy against Colorectal Cancer Cells by Inhibition of NF- k B and Src Protein Kinase Signaling Pathways. 2013;8(2):1–13.